ISSN: 2152-7385 Volume 11, Number 8, August 2020

Scientific Research Publishing

Applied Mathematics

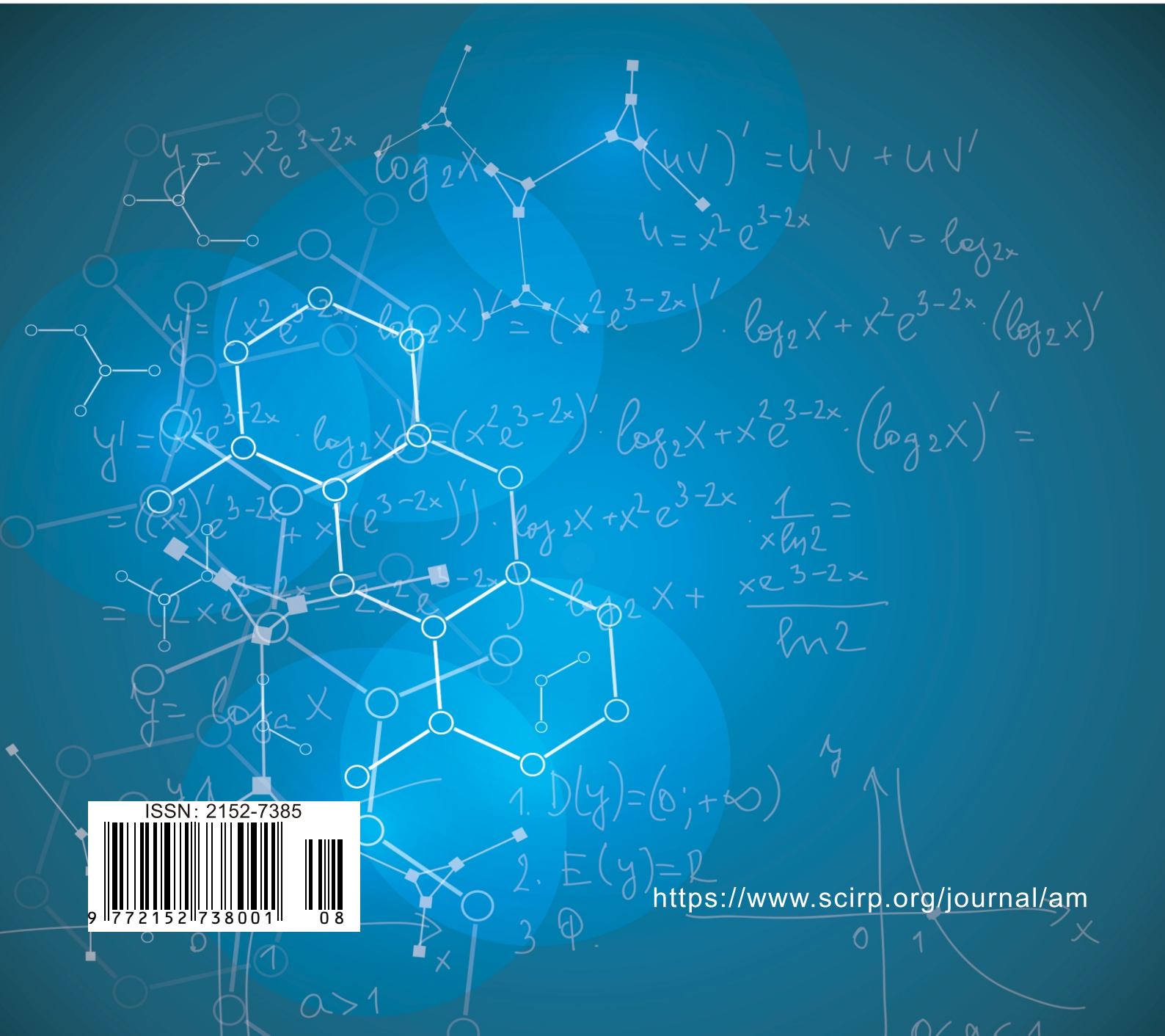

ISSN: 2152-7385

https://www.scirp.org/journal/am

Journal Editorial Board

ISSN Print: 2152-7385 ISSN Online: 2152-7393

https://www.scirp.org/journal/am

Editorial Board

Scientific Research Publishing

Applied Mathematics, 2020, 11, 739-844
https://www.scirp.org/journal/am
ISSN Online: 2152-7393
ISSN Print: 2152-7385

Table of Contents

Volume 11 Number 8 August 2020

Applied Mathematics (AM)
Journal Information

SUBSCRIPTIONS

The *Applied Mathematics* (Online at Scientific Research Publishing, https://www.scirp.org/) is published monthly by Scientific Research Publishing, Inc., USA.

Subscription rates:
Print: $89 per copy.
To subscribe, please contact Journals Subscriptions Department, E-mail: sub@scirp.org

SERVICES

Advertisements
Advertisement Sales Department, E-mail: service@scirp.org

Reprints (minimum quantity 100 copies)
Reprints Co-ordinator, Scientific Research Publishing, Inc., USA.
E-mail: sub@scirp.org

COPYRIGHT

PRODUCTION INFORMATION

For manuscripts that have been accepted for publication, please contact:
E-mail: am@scirp.org

Scientific Research Publishing

Applied Mathematics, 2020, 11, 739-752
https://www.scirp.org/journal/am
ISSN Online: 2152-7393
ISSN Print: 2152-7385

On Separation of Charges and Formation of Linear Structures in the Nuclei of Dislocations in Metals

V. L. Busov

Donbass State Engineering Academy, Kramatorsk, Ukraine
Email: vlbusov49@gmail.com

How to cite this paper: Busov, V.L. (2020) On Separation of Charges and Formation of Linear Structures in the Nuclei of Dislocations in Metals. *Applied Mathematics*, **11**, 739-752.
https://doi.org/10.4236/am.2020.118049

Received: July 9, 2020
Accepted: August 15, 2020
Published: August 18, 2020

Abstract

In metals, the non-adiabatic mechanism of charge separation into the electron, cation, and vacancy chains is considered. It includes: 1) the photoelectric effect caused by bremsstrahlung caused by the scattering of conduction electrons by impurity ions lying at the ends of these chains and oscillating with the frequency of the local phonon mode; 2) knocking out from the metal cations of the matrix, sufficiently slow (in comparison with the conduction electrons) photoelectrons that pull these cations from the nodes, thereby not violating the electroneutrality condition in the model of a free electron gas as with the static state of the chains and at their motion (slipping, recrawling) in the absence of a thermal field; 3) induced radiation along the line of chains; 4) the formation of linear structures in the spatial lattice of octahedral interstitial sites. The conditions for the formation of quasistable bound states in the dislocation core are considered. A hypothesis is advanced that the latent energy in the dislocation cores contains a component that is of an electromagnetic nature.

Keywords

Nonadiabatic Process, Bremsstrahlung, Photoelectric Effect, Photoelectrons, Induced Radiation, Quasistable Bound States

1. Introduction

It is known that in metals near edge dislocations there is a difference in bulk density above and below the slip plane [1] [2] [3]. For the ground state of a free electron gas in metals [4], the Fermi energy $\varepsilon_F \sim n_e^{2/3}$, where n_e is the bulk concentration of conduction electrons, is the same at all points of the crystal.

Near the dislocation in the compacted sections above the slip plane, there is a lack of electrons, and in the rarefaction region there is an excess, which leads to a violation of electroneutrality and the appearance of an electric dipole with a dipole moment distributed along the dislocation line and directed along the normal to the slip plane. On the other hand, the solution of the problem of scattering of conduction electrons near the line of edge [5] and screw [6] dislocations is well known, where it was assumed that, firstly, the scattering of conduction electrons by cations is elastic due to its large mass in comparison with the mass of the electron and, accordingly, the negligible recoil momentum and displacement of the cation at the lattice node during scattering, the energy of an electron in a collision can be assumed to be unchanged; secondly, the solution was obtained at large distances from the dislocation line $\rho \approx 2a_0 \div 25a_0$ (a_0 is the lattice parameter) with the help of asymptotic wave functions and Friedel basis functions [7].

Here it is shown that, first of all, regardless of the type of dislocation around its line, an oscillating distribution of the excess electric charge of the conduction electrons arises $q_{scr}, q_{edg} \sim r^{-5/2}$ (r is the distance from the dislocation line to the collision point) in difference from scattering by a charged impurity ion: $q_{imp} \sim r^{-3}$; secondly, for an edge dislocation, $q_{edg} \sim \sin\beta \cdot \sin\left(2k_F + \frac{\pi}{4}\right)$, where k_F is the modulus of the Fermi wave vector, β is the angle between the Burgers vector and the radius vector $\boldsymbol{r}$, which corresponds to the deformation field of the defect r^{-1}; for a screw dislocation $q_{scr} \sim r^{-5/2}\cos\left(2k_F + \Phi\right)$, where Φ is the phase shift, which reflects the axial symmetry of the defect. However, the distribution $q_{scr}, q_{edg}(r)$ [5] [6] caused by the deformation field of the defect r^{-1} in the region of a good crystal does not allow us to reliably determine $q_{scr}, q_{edg}(r)$ inside the cylindrical region around the defect line with the radius $r \approx 0.1 \div 0.2$ nm, as well as the shape, height and width of the potential barrier in these nuclei. In addition, as noted by Friedel [7], the conduction electrons are fast particles and, when passing near the dislocation, they do not settle on the cations of the dislocation core, but only change the direction of their motion, creating a dynamic picture of charge redistribution. As an attempt to remedy the situation, work [8] is known, where in the tight-binding approximation, the solution of the Schrödinger time equation was found by numerical methods for a two-dimensional distorted lattice of cross section perpendicular to the dislocation line considered in the Peierls-Nabarro model. Here, the distribution of the local density of states $N_0(\varepsilon)$ of electrons on the energy scale ε is obtained, which contains two pronounced high peaks, one of which is located in the region $\varepsilon < 0$ and the other at $\varepsilon > 0$, while the point $\varepsilon = 0$ divides the intermediate segment between the peaks, for example, for the s-s bond and the various spatial dependences of the transfer integrals $T(R)$, $\boldsymbol{R} = \boldsymbol{\rho} - \boldsymbol{\rho}'$ in the nearest-neighbor approximation: for the power $T \sim R^{-5}$ in the relation 1 (in $\varepsilon > 0$) to 1.5 (in $\varepsilon < 0$); at an exponential $T \sim \exp(-\alpha R) - 0.5/1.5$. In the same time there is no interpretation of this form of $N_0(\varepsilon)$. The results of the numerical

calculation show the decisive role of the dislocation core for the electronic structure of the defect in comparison with the effect of the long-range part of the deformation potential [5] [6].

It is also known ([9], p. 99) that, in crystals of the NaCl type, edge dislocations in the $\{111\}$ plane with a Burgers vector $\frac{a_0}{2}\langle 110\rangle$ and a linear (running) charge density $Q_{\mathrm{NaCl}} = \pm e/2a_0$ are charged. In semiconductor crystals, particularly in n-type germanium and silicon, a chain of unpaired valence electrons along the dislocation line forms a negative charge density Q_{sc}, $Q_m < Q_{sc} < Q_{\mathrm{NaCl}}$ ([9], p. 101). In metals, according to [10] [11], this density is $Q_m \approx -(0.01 \div 0.1)e/a_0$ in contrast to [5] [6], where the total charge of excess density q_{scr}, q_{edg} in volume around the dislocation line at $V_d \to \infty$ tends to zero.

The purpose of this paper is to identify the mechanism for separating the charges of electrons and metal cations, which allows the generation of dislocation nuclei, and the formation of linear structures, as well as the determination of the conditions for the appearance of quasistable bound states in the dislocation core.

2. Theoretical Model

First we note that the electric charge, as well as energy, momentum, etc. is the integral of motion ([12], p. 505) is preserved in space and in time. Generation of dislocations occurs mainly in a perfect crystal, where the total charge $\sum_i q_i$ in its individual volumes and in the entire volume is initially zero. Therefore, after generating the defect $\sum_i q_i = 0$. In addition, as a result of the movement (slipping, recrawling), a single defect leaves no trace in the crystal except for extrusions and intrusions on its free surface. If we consider the separation of charges as a short-lived state for a characteristic period of time T within the trial volume V, then the condition $\sum_i q_i = 0$ must be softened, averaging it according to

$$\left\langle \sum_i q_i \right\rangle_{V,T} = 0. \tag{1}$$

On the other hand, the separation of charges in metals mainly occurs under the influence of an external electromagnetic field, penetration of which into the material is possible only within the skin layer. The question arises: "How does the charge separation occur when generating dislocation nuclei outside the skin layer?" Here it should be noted that practically all dislocation models, known in the literature, reflect adiabatic processes, *i.e.* at the beginning metal cations are shifted, and then electrons are "adjusted" for these displacements. In this paper, we abandon this approach and state hypothesis 1: *The processes of generation and motion of the cationic chain, as well as of the entire core of the dislocation as a whole, are nonadiabatic.* Here, we will use an intermittent field of electromagnetic nature as the generating field of defect nuclei. At the first stage, we shall single out the main scheme of the charge separation mechanism during generation, where as an intermittent field we take the bremsstrahlung of the

conduction electrons, which form the halo of the charge q_{scr}, q_{edg}, when a charged impurity ion moves along a certain periodic law. Here, for simplicity, we use the harmonic oscillations $\cos\Omega t$ (Ω is the frequency of the natural oscillations of the impurity ion as a local phonon mode ([13], p. 358). This radiation can cause a photoelectric effect for electrons of internal L, K-shells, thus forming a sufficiently slow (in comparison with the conduction electrons) photoelectrons, as well as induced radiation along the dislocation line and long-wavelength secondary photons that go to the region of a good crystal where they are elastically scattered on the metal cations. In other words, we arrive at the problem of scattering of bremsstrahlung photons on bound electrons L, K-shells, and in the absence of secondary photons to resonant scattering ([14], p. 384).

To determine the initial generation conditions, let us use the experiment [15] to determine the electromagnetic emission (EME) in the process of intermittent deformation in an AlMg6Mn aluminum alloy (Al-6.03 wt% Mg-0.5% Mn), where the samples were stretched at a constant rate of increase of the applied stress σ. This alloy is a solid solution of Mg and Mn in an aluminum matrix, and in the first stage the influence of Mn is neglected. The light impurity atom Mg ($M_{\mathrm{Mg}} < M_{\mathrm{Al}}$) gives both valence electrons to the subsystem of the collectivizated conduction electrons of the whole alloy and forms an single impurity ion Mg^{2+} [16], which creates a local oscillation mode with a frequency [13]

$$\omega_L = \omega_{\max}\sqrt{1-\epsilon^2} \tag{2}$$

at $M_{\mathrm{Mg}} = M_{\mathrm{Al}}(1-\epsilon)$ and $\epsilon > 0$ without taking into account the change in the force constant. We note that the axis along which the impurity ion oscillates has a stereographic projection equally distributed in a full solid angle and has a spherical polarization as $t \to \infty$. Under the actual conditions of the alloy, the homogeneous distribution of the cations Mg^{2+} takes place on average, for which the average distance R_{Mg} between them is much larger than the distance r_{lm} of the amplitude of the oscillations decrease to zero: $R_{\mathrm{Mg}} \gg r_{lm}$. If a weak impact (shock) is applied to the free surface of the alloy sample, the displacement of the ion Mg^{2+} is different from the displacements of the surrounding cations Al^{3+} at $t = 0$ due to the difference in ionic radii $r_{ion}\left(\mathrm{Al}^{3+}\right) = 0.057$ nm and $r_{ion}\left(\mathrm{Mg}^{2+}\right) = 0.074$ nm without taking into account the influence of the coordinate number ([17], p.75), which leads to the replacement of the spherical polarization of the oscillations by linear polarization. In addition, the main feature of [15] for $\sigma = \dot{\sigma}_0 \cdot t, \dot{\sigma}_0 = const$ is the linear increase in the EME pulse amplitude $\varphi_{\mathrm{EME}}(t)$ in time t, and the time intervals between neighboring pulses, especially in its central part are practically equidistant. We recall that the energy stored in the crystal as a result of pumping at time t is numerically determined by the area under the σ-ε curve, which allows us to replace the time coordinate of the energy coordinate: $\varphi_{\mathrm{EME}}(\varepsilon)$.

2.1. Bremsstrahlung

Let us consider the law of conservation of energy and momentum ([14], p. 387)

in the scattering of conduction electron by an impurity ion

$$p_{1\mu} - p_{2\mu} = k_\mu - q_\mu \ (\mu = 0,1,2,3), \tag{3}$$

where $p_{1\mu}, p_{2\mu}, k_\mu$ and q_μ are the 4-momentum of the incident electron, the scattered electron, the bremsstrahlung photon and the recoil of the ion nucleus, respectively. For the time components of these pulses, expression (3) is written in the form

$$\varepsilon_1 - \varepsilon_2 = \varepsilon_\gamma + \varepsilon_{nr}, \tag{4}$$

$\varepsilon_1, \varepsilon_2, \varepsilon_\gamma$ and ε_{nr} are the kinetic energy of the initial and final states of the electron, the photon energy of bremsstrahlung and the recoil of the nucleus of the impurity ion, respectively. For the spatial components of 4-momenta

$$\boldsymbol{p}_1 - \boldsymbol{p}_2 = \boldsymbol{k} - \boldsymbol{q}. \tag{5}$$

In the limiting case of low energies of primary electrons from $\varepsilon_F = 3-10$ eV in metals up to tens of keV in the problem of the continuous spectrum of x-rays, the photon momentum $|\boldsymbol{k}|$ small compared with the momentum of the electron in view of the practically zero rest mass of the photon, and there fore

$$\boldsymbol{q}^2 = (\boldsymbol{p}_1 - \boldsymbol{p}_2)^2. \tag{6}$$

In the nonrelativistic case, with the initial velocity of the electron $|\boldsymbol{v}_e| \ll c$, c is the speed of light, the differential bremsstrahlung cross section is equal to the product of the Rutherford elastic scattering cross section $\mathrm{d}\sigma_s$ by the photon emission probability $\mathrm{d}w_\gamma$

$$\mathrm{d}\sigma_\gamma = \mathrm{d}\sigma_s \cdot \mathrm{d}w_\gamma, \tag{7}$$

where

$$\mathrm{d}w_\gamma = \frac{\alpha}{(2\pi)^2}\left[\frac{\boldsymbol{k}}{\varepsilon_\gamma}(\boldsymbol{v}_{e1} - \boldsymbol{v}_{e2})\right]^2 \frac{\mathrm{d}\varepsilon_\gamma}{\varepsilon_\gamma}\mathrm{d}o, \tag{8}$$

and α is the fine structure constant, $\alpha \approx 1/137$; $\boldsymbol{v}_{e1}$ and $\boldsymbol{v}_{e2}$ are the velocity vectors of the primary and scattered electron; $\mathrm{d}o$ is the solid angle element. Here, the radiation intensity I reaches a maximum in the direction perpendicular to the plane of motion of the electron $(\boldsymbol{p}_1, \boldsymbol{p}_2)$ *i.e.* when $\boldsymbol{k}$ lies in this plane. In accordance with the classical theory of radiation, $\mathrm{d}w_\gamma$ is the ratio of the intensity of the dipole radiation I_d at low frequencies to the photon energy ε_γ equal to the average number of photons n_γ per unit time. We note that the representation of the bremsstrahlung cross section in the form (7), (8) is possible in all those cases in which low-frequency photons are emitted. In this connection, the theoretical spectrum of bremsstrahlung in a metal, for example, in aluminum ([14], p. 398), is of interest in the form of the dependence I_d on ε_γ / T_e (T_e is the kinetic energy of the primary electron), taking into account the electron shielding of the inner shells of the impurity ion, which allows one to eliminate the divergence as $\varepsilon_\gamma \to 0$ in the process of determining the total cross section σ_γ with the help of (7), (8). Here, in the interval $\varepsilon_\gamma = (0.2 \div 0.8)T_e$, the value

of I_d (in relative units) varies from 7 to 4, *i.e.* in engineering calculations is replaced by an average of 5.5, and for light elements of type Al screening is of little significance. It becomes clear from the expressions (3)-(8) that by changing the components of the 4-momentum of the impurity nucleus q_μ in time by an external action, leading to jumps $[q_0]$ and $[\boldsymbol{q}]$, wherein it is possible to achieve level jumps $[I_d]$, where the jump $[\boldsymbol{q}]$ creates a discontinuous displacement of the ion nucleus $[l]$ along an arbitrary axis *l*. To do this, we place single impurity ion in an ideal crystal at a distance *R* from its free surface, with $R \gg a_0$. We divide the entire space of the crystal into two half-spaces by a plane parallel to its free surface. Here we note that according to the theory of periodic chains of bonds between atoms and estimates of the surface energy of the free surface of the crystal ([18], p. 14), the crystallographic orientation of the crystal must correspond to the most densely packed crystallographic plane. In our case of metals with a face-centered lattice this is a family of slip planes $\{111\}$ in Al. Here, the light ion Mg^{2+} is in an octahedral interstitial site with six nearest neighbors—cations Al^{3+} ([3], p. 122). The total recoil momentum $\sum_j \boldsymbol{q}_j$ that imparts to the impurity nucleus the conduction electrons scattered on it from the lower half-space $\sum_j \boldsymbol{q}_j(\mathrm{LHS})$ is equal in magnitude and opposite in sign to the analogous momentum transferred from electrons from the upper half-space $\sum_j \boldsymbol{q}_j(\mathrm{UHS})$ without taking into account the influence of thermal oscillations and in the absence of external forces. As already noted, there exists a local mode of oscillations of the ion Mg^{2+} with a frequency ω_L by gap from the upper spectral phonon band. Here, the dipole moment of the charge system "impurity ion-distribution of scattered electrons" is equal to zero due to the symmetry of the lattice, while the stereographic projection of the ion oscillation axis is uniformly distributed in a full solid angle in time $t \gg T_L = 2\pi/\omega_L$. If a weak impact (shock) is made on the free surface of the crystal along the normal to it, then the recoil momentum $\boldsymbol{q}_{nr}$ given to the nucleus of the single impurity is equal to the difference $\sum_j \boldsymbol{q}_j(\mathrm{LHS})$ (the coincidence of the directions of the external force action and the recoil of the ion nucleus from scattering electrons) and $\sum_j \boldsymbol{q}_j(\mathrm{UHS})$ (the above directions are opposite)

$$\boldsymbol{q}_{nr} \equiv [\boldsymbol{q}] = \sum_j \boldsymbol{q}_j(\mathrm{LHS}) - \sum_j \boldsymbol{q}_j(\mathrm{UHS}) \tag{9}$$

and arises in the form of a jump $[\boldsymbol{q}]$. Here it should be noted that under the influence of the impact both the impurity ion and its nearest and subsequent cations Al^{3+} are displaced, where for the easy Mg^{2+} this displacement is obviously larger. As a result, such a impact (shock) lowers the point symmetry of the lattice to the axial symmetry near the impurity ion, but all the characteristics of a free electron gas under translational invariance must correspond to periodic boundary conditions within a three-dimensional cube with the side $L \gg a_0$, and the time interval $\tau_e \approx L/v_F$ (v_F is Fermi velocity) within the framework of this model is proportional to the relaxation time of the free-electron subsystem and plays the role of the time for its "adjustment" to the lattice change for a free path length of order *L* and collisions with one impurity ion. On the other hand, the

time interval for the amplitude shift of the impurity ion $\Delta t_{\mathrm{Mg}} \approx a_0 / v_s$ (v_s is the sound velocity) for a perfect aluminum single crystal at $L \approx 10^{-2}$ m and $v_F \gg v_s$, and for the intervals τ_e and Δt_{Mg}, the condition $\Delta t_{\mathrm{Mg}} \ll \tau_e$ is satisfied. In this case, the charged ion is displaced with respect to the spherically symmetric distribution of the excess density q_{edg}, q_{scr} of the charge of the conduction electrons, and a dipole moment of the system arises at the time $t = \Delta t_{\mathrm{Mg}}$

$$P_s = \left(k_m - k_{imp}\right) \cdot e \cdot \Delta z_{\text{Mg-Al}}, \tag{10}$$

where k_m and k_{imp} are valences of matrix and impurity atoms, respectively; $\Delta z_{\text{Mg-Al}}$ is the displacement amplitude of the Mg ion with respect to the nearest neighbors, $\Delta z_{\text{Mg-Al}} \approx \left(0.01 \div 0.1\right) \cdot a_0$. Hence, the bremsstrahlung intensity I_d in the dipole approximation ([19], p. 206) for an single impurity is

$$I_d = \frac{e^2 \left(k_m - k_{imp}\right)^2}{3c^3} \cdot \omega_L^4 \cdot \left(\Delta z_{\text{Mg-Al}}\right)^2. \tag{11}$$

In a real aluminum polycrystalline with a grain dispersion of 10 ÷ 100 μm, the values of τ_e and Δt_{Mg} are of the same order $\Delta t_{\mathrm{Mg}} \cong \tau_e$, but $\Delta t_{\mathrm{Mg}} > \tau_e$. Here, in the expression (11), the frequency ω_L should be replaced by the plasma frequency ω_p with implicit replacement of the mass M_{ion} by m_e, where the intensity I_d increases by 5 - 6 orders of magnitude and the excitation of cation energy levels and knock out photoelectrons becomes possible.

2.2. Photoelectric Effect

Let us consider the scheme of the energy levels of the Mg atom ([12], p. 558), analogous to the scheme of the Al atom. Here we can distinguish two concepts: the binding energy ε_i and the ionization energy I_i. For an single atom ε_i coincides in absolute value with the length of a energy segment from zero to a level corresponding to a given *s*, *p*, *d*, ... electron in the region $\varepsilon < 0$, and the quantity $I_i > \varepsilon_i$ in the region $\varepsilon > 0$ corresponds to the electron state as $r \to \infty$, r is the distance from the nucleus. In the crystal, the definition of ε_i remains unchanged, and the determination of I_i as a function of r essentially depends on the degree of screening by the conduction electrons. In dielectrics and semiconductors, the Coulomb interaction of the knocked out electron and the resulting cation can be neglected even at $10a_0 < r < 100a_0$. In metals, this interval is $5a_0 < r < 10a_0$. Consider the absorption of the bremsstrahlung photon γ_{br} by the electron of the internal L, K-shells of the cation Al^{3+} in the case when the photon energy ε_γ exceeds ε_i and the knocked out electron passes to the continuous spectrum region for $\varepsilon > 0$, *i.e.* there is a photoelectric effect. In this case, the photoelectron in the nucleus of the dislocation must reach a region roughly $a_0 < r < 2a_0$.

The most accurate description of the photoelectric effect is given by quantum electrodynamics ([14], p. 360), where in the nonrelativistic case an angular dependence of the differential photoelectric cross section for unpolarized incident photons γ_{br}

$$d\sigma_{phef} \sim \sin^2 \vartheta, \tag{12}$$

where ϑ is the angle between the polarization vectors of the photon $\boldsymbol{e}_\gamma$ and the photoelectron momentum $\boldsymbol{p}_{phe}$. For polarized incident photons γ_{br} is replaced by

$$\sin^2 \vartheta \to \cos^2 \vartheta = \sin^2 \vartheta \cdot \cos^2 \varphi, \tag{13}$$

where φ is the angle between the planes $\left(\boldsymbol{p}_{phe}, \boldsymbol{k}_\gamma\right)$ and $\left(\boldsymbol{k}_\gamma, \boldsymbol{e}_\gamma\right)$ ($\boldsymbol{k}_\gamma$ is the wave vector of the incident photon γ_{br}. Analysis (12), (13) shows that the majority of photoelectrons emerge in the direction of polarization vector $\boldsymbol{e}_\gamma$ of the incident photon γ_{br} (condition*). The total cross section of the photoelectric effect on the K-shell in the Born approximation ([14], p. 362) has the form

$$\sigma_K = A_K \cdot \varepsilon_\gamma^{-7/2}, \tag{14}$$

where $A_K = A_0 \cdot I_{i1}^{5/2}(\mathrm{Al})$; $A_0 = 64\alpha/3m_e$; $I_{i1}(\mathrm{Al})$ is the ionization energy of the Al atom on the K-shell. In the photoelectric effect on the L-shell, the total cross section breaks up into a cross section when it is absorbed by two 2s-electrons

$$\sigma_{L_I} = A_1 \cdot \varepsilon_\gamma^{-4} + A_2 \cdot \varepsilon_\gamma^{-5}, \tag{15}$$

and the cross section for absorption by six 2p-electrons

$$\sigma_{L_{II}} + \sigma_{L_{III}} = A_3 \cdot \varepsilon_\gamma^{-5} + A_4 \cdot \varepsilon_\gamma^{-5}, \tag{16}$$

where $A_1\left(I_{i2}^{m_1}\right), A_2\left(I_{i2}^{m_2}\right), A_3\left(I_{i2}^{m_3}\right), A_4\left(I_{i2}^{m_4}\right)$ have the same structure as A_K, but different numerical coefficients and exponents m_j for $I_{i2}(\mathrm{Al})$-the ionization energy of the Al atom on the L-shell, and $I_{i2}(\mathrm{Al}) < I_{i1}(\mathrm{Al})$. Here it should be noted that when $\varepsilon_\gamma - \varepsilon_i \to 0$, when the kinetic energy of photoelectrons is small in comparison with $\varepsilon_\gamma, \varepsilon_i$, resonance scattering takes place ([14], p. 384), where a narrow band is cut out from the continuous bremsstrahlung spectrum, which when knocking out photoelectrons from the internal L, K-shells of the cation Al^{3+} corresponds to the line absorption spectrum. This is indicated by a comparison of the power dependences of the bremsstrahlung cross sections σ_{br} and σ_K, σ_{L_n} on ε_γ in (8) and (14)-(16).

2.3. Induced Radiation

According to the definition, the frequency, phase, polarization and direction of propagation of the electromagnetic wave incident on the metal cation coincide with the same characteristics as the absorbed cation, and after its excitation of the emitted wave. Hence, the energy of the induced radiation wave will be transferred from one cation Al^{3+} to the neighboring cation without losses, until the wave reaches an impurity ion Mg^{2+}, in which another scheme of energy levels, which leads to elastic scattering back. If the normals of the effective scattering cross sections of two impurity ions lie within the same line, then a standing wave of stimulated or induced radiation arises. We assume that parallel to the free surface of aluminum is a slip plane, where at the nodes of the square grid of oc-

tahedral interstices there are impurity ions and standing waves of induced radiation appear in each section of grid cells under the influence of a weak shock and bremsstrahlung.

2.4. Separation of Charges and Bound States in the Dislocation Core

Let us consider the crystallography of one of the slip planes (111) of a face-centered lattice, which intersects the lines of the main diagonals of the cells of this lattice along the $\langle 111 \rangle$ directions normal to this plane within one cell. If the bremsstrahlung photon γ_{br} is transverse: its wave vector $\boldsymbol{k}_{phe} \perp \boldsymbol{n}_{(111)}$ ($\boldsymbol{n}_{(111)}$ is the unit vector of the normal to the (111) plane) lies in this plane, and its the polarization vector $\boldsymbol{e}_{br}$ is directed along $[111] \| \boldsymbol{n}_{(111)}$, then the photon γ_{br} can produce a photoelectric effect on the inner shells of the first cation Al^{3+}, which intersects $\boldsymbol{e}_{br}$ on the main diagonal of the cell. The photoelectron e_{phe} ejected by the photon γ_{br} moves according to the condition (*) in the direction $\boldsymbol{e}_{br}$ and depending on the level of the kinetic energy T_{phe} obtained from the photon, it can settle on the first counter and on the subsequent interstitial sites. The possible states of photoelectrons are due to the joint influence of the Coulomb attraction of the cation from which they were knocked out, and the spherically symmetric potential of attraction of the octahedral interstice as a force center. To describe these states and the possible structure arising under the influence of bremsstrahlung, we use the definition of stable bound and quasistable bound states ([19], p. 671), where, for the particle system, in our case, the systems of metal cations and photoelectrons, first, their relative the motion is finite for a long time in comparison with the periods typical for the given system; second, for the formation of bound states, it is necessary to have attractive forces, which for cations and photoelectrons is natural. If the range of distances on which these particles are attracted is separated by an energy potential barrier from the region in which they repel, then the particles can form stable states. Such states lie in the energy region $\varepsilon < 0$, for $\varepsilon > 0$ they do not exist. However, in the region $U_0 < \varepsilon < U_b$ (U_0 is the depth of the potential well, U_b is the height of the potential barrier), for some values of ε there can exist quasi-stable bound states, the lifetime of $\tau_{qwsb} \sim w_{tt}^{-1}$ which is determined by the probability of the tunnelling transition w_{tt} through potential barrier. In this connection, we can disclose the physical essence of the local density of electron states $N_0(\varepsilon)$ [8], where a quasi-periodic sequence of shallow minima occurs between a high lower peak at $\varepsilon < 0$ and a high upper peak at $\varepsilon > 0$ for a power-law dependence of the transport integral. With the help of this sequence and the whole of $N_0(\varepsilon)$, we can qualitatively estimate the shape of the potential relief on the energy scale in the dislocation core if we symmetrically reflect the upper half-plane of the graph $N_0(\varepsilon)$ on its lower half-plane with respect to the energy axis or, more simply, turn the sheet with the graph by 180˚. Such modeling of the potential relief shows that the lower peak corresponds to a narrow potential well of a rectangular shape with a depth of U_{01}, and the upper one cor-

responds to the same well with a depth of U_{02}, and $U_{02} > U_{01}$. Inside the intermediate interval between the peaks, firstly, there is a weak growth of the regular component of the potential relief towards upper peak, and secondly, at the beginning and at the end of this energy interval, the Fourier components of the above sequence, oscillating against the background of the regular component, are substantially higher than analogous components within the interval. The linear structure along the $\langle 111 \rangle$ and $\boldsymbol{e}_{br}$ directions, which does not contradict the potential relief of the dislocation core obtained from the numerical calculation [8], is shown in **Figure 1**. Here at position *A* there is a site vacancy, at position *B* in octahedral interstice—cation Al^{3+}, which passed from node *A*, to position near the node *C*—photoelectron, at position *D*—the nearest cation Al^{3+}, displaced under the total influence of vacancy *A*, cation *B* and photoelectron *C*. Note that the distance between the positions *A* and *B* is $b_0 = \sqrt{2} \cdot a_0 / 2$, between *B* and *C* does not exceed $\le b_0$, and the distance *CD* is determined by the interval $r_{ion}\left(Al^{3+}\right) < R < b_0$; all of the matrix metal cations following position *D* shift from the position *C* to the depth of the material in accordance with the law r^{-1}.

Under the influence of the bremsstrahlung causing the photoelectric effect, the subsequent formation of two systems of bound charges in the space lattice of the octahedral interstices is taking place., where the first system consists of a chain of photoelectrons near the nodes *C* with a linear charge density $Q_{phe} = -k_{phe} \cdot e/a_0$ (k_{phe} is the number of knocked out photoelectrons, $k_{phe} = 1, 2, 3$) and chains of metal matrix cations in interstices *B* c linear density after the departure of photoelectrons from the inner shells of these cations $Q_{we} = +k_{phe} \cdot e/a_0$. The second system in the model of a free electron gas (jelly model) contains an inhomogeneity in the form of a "ridge" of bulk density δn with a linear density $Q_{\delta n} = +3e/a_0$ in the interstices *B*, and along the nodes *A* with $Q_{vch} = -3e/a_0$ *i.e.* "valley" in the homogeneous distribution of a positive charge smeared in space, whose density is equal in magnitude and opposite in sign to the mean charge density of conduction electrons, so that the system of a free electron gas is always electrically neutral. Hence the total linear charge density of the cationic chain $Q_{cch} = Q_{we} + Q_{\delta n}$.

To determine the mutual arrangement of the above chains in the face-centered lattice Al, we use the crystallography of the {111} slip plane and the system of the main diagonals {111} ([20], c. 24). We assume that translational invariance is preserved along the dislocation line between the impurity ions bordering it. Hence, along the dislocation line, a periodic sequence of the above linear structures arises, both along the normal to the chosen plane (111), and in the plane itself along the normal to the dislocation line.

The analysis shows that consideration of the Coulomb effect of cationic and vacancy chains with distributed linear charges on the photoelectron chain in the defect nucleus should be carried out together with the influence of the distributed excess charge q_{scr}, q_{edg} of conduction electrons. The model representation

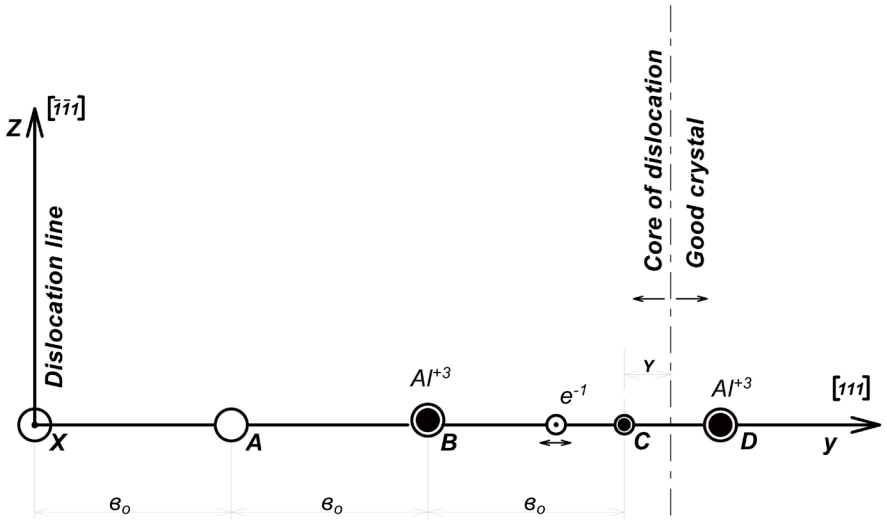

Figure 1. Linear structure in dislocation core in metals with face-centered lattice. *A*, *B*, *C*, *D*-positions of particles in octahedral interstitial sites. The axis *Z* is along the direction $\left[\bar{1}\bar{1}1\right]$ of the line of dislocation; axis *Y* along the direction $\left[111\right]$ on of the normal to the dislocation line and the plane (111).

of the potential relief V_d in the core of the defect does not allow to obtain from the distribution $N_0(\varepsilon)$ a dependence $V_d(\rho,\varphi,z)$ on the cylindrical coordinates with the help of [8].

A description of the dynamics of the above structure in the dislocation core and in a good crystal is possible using the theory of the LHOPS method ([2] [13], p.208) and [21] [22], in which cations and photoelectrons at positions *B* and near *C*, with taking into account their orbital, spin and total moments in the corresponding interstices and nodes. We carry out a detailed description of this dynamics in a separate work.

3. Discussion of the Results

The mechanism of charge separation and the formation of linear structures in the generation of the dislocation nucleus are more realistic than the known adiabatic elastoplastic models of the continual theory of individual dislocations, atomic models of dislocation nuclei as it includes the natural processes of bremsstrahlung, photoelectric effect, and Coulomb interaction. In the framework of this model, we do not cut and do not move the material on both sides of the cut in the appropriate way, we do not remove or relax it after these operations, but we produce a natural weak shock on the free surface. Here we can consider standing electromagnetic waves not only between impurity ions, but between impurity ions and the free surface, intergranular, interphase boundaries, and also boundaries of deformation origin. In addition, the bremsstrahlung of photoelectron chains leads us to the plasma frequency of oscillations, the theory of solid-state plasma ([19], p. 539).

The analysis in **Figure 1** also shows that the boundary between the dislocation

core and the good crystal passes in the interval CD and is separated from the dislocation line on which the centers of impurity ions lie at a distance $r_{core} = 2b_0 + Y$, where $Y \le CD - r_{ion}\left(\mathrm{Al}^{3+}\right)$ has yet to be found. It is also of interest to supplement the well-known statement for disordered media on the statistical homogeneity on the average [23] with statistical isotropy in the mean. In this case, the intermittent field must be periodic in time and create linear structures in two opposite directions.

We compare the experimental dependence of the EME pulse amplitude $\varphi_{\mathrm{EME}}(\varepsilon)$ [8] with the current-voltage characteristic in the Frank-Hertz experiment ([12], p. 542), where the accelerated cathode electrons undergo inelastic scattering by Hg atoms when the anode potential of the tube coincides with the critical potential Hg, and elastic scattering in the absence of this coincidence, *i.e.* the energy of the atoms varies discretely. In our case, with plastic deformation $\dot{\sigma} = \mathrm{const}$, the amplitude $\varphi_{\mathrm{EME}}(\varepsilon)$, and together with it the energy accumulated in the crystal, also varies discretely. The natural question arises: "How do the above described linear structures distributed between two impurity ions contribute to the accumulation of energy in the crystal?" The answer follows from the above: only thanks to the energy level scheme of the cation of the matrix peculiar to him alone. Let us hypothesize 2: *The latent energy of a crystal accumulated in dislocation cores contains a component that is of an electromagnetic nature.*

This raises a natural question: What is the relationship between bremsstrahlung intensity I_d and the recoil momentum of the impurity ion $\boldsymbol{q}_{ii}$ and cation matrix $\boldsymbol{q}_{mi}$ on impact? Here we will use work [24] and consider in the generalized space of rectangular pulses the effect of a rectangular pulse of the displacements $L_{\sqcap} u$ on the system "impurity ion—distribution of conduction electrons" at a certain point $\boldsymbol{r}$ in the traveling wave regime, where $L_{\sqcap} = U_{-}(x) - U_{-}(x+\tau)$ is a linear operator of rectangular pulses; U_{-} is jump operator. At the first stage $L_{\sqcap} u$, at the time t, a dipole moment $d_0 = e[u]\delta(t)$ occurs, where $[u]$ is a jump in the displacement of the impurity ion relative to the surrounding cations of the matrix, then the halo of conduction electrons around the impurity ion is redistributed over relaxation time $\tau_{re} \approx (0.01 \div 0.03) b_0 / v_F \approx 10^{-14} \div 10^{-15}\,\mathrm{s}$, $v_F = 10^6\,\mathrm{m/s}$ ($b_0 = 0.7 a_0$) before inverting $d_0 = e[u]\delta(t+\tau_{re})$ to zero. Such relaxation at $\tau_{re} \ll T_{rep}$ is a source of bremsstrahlung of an intermittent field, where the bremsstrahlung intensity is $I_\gamma \sim \square \exp(-t/\tau_{re}) \sim \omega_{re}^4$, where $\square = \triangle - \frac{1}{c^2}\frac{\partial^2}{\partial t^2}$; $\omega_{re} = \tau_{re}^{-1}$ is the relaxation frequency of the conduction electron subsystem. At the second stage $L_{\sqcap} u$, with $t+\tau$, the radiation algorithm is repeated, but this field changes sign. Here $\Delta z_{\mathrm{Mg\text{-}Al}} = u_{\mathrm{Mg}} - u_{\mathrm{Al}} \sim |\boldsymbol{q}_{ii} - \boldsymbol{q}_{mi}|$. Hence $I_\gamma \sim \left(E_0^{if}\right)^2 \approx I_d \sim |\boldsymbol{q}_{ii} - \boldsymbol{q}_{mi}|^2$. In addition the vectors $\boldsymbol{q}_{ii}$ and $\boldsymbol{q}_{mi}$ are collinear and have the same direction, and the acceleration vectors of conduction electrons $\boldsymbol{a}_e$ and $\boldsymbol{q}_{ii} - \boldsymbol{q}_{mi}$ are also collinear, but directed towards each other, while it is well known from classical electrody-

namics that $I_d \sim |\boldsymbol{a}_e|^3$, where $|\boldsymbol{a}_e| \approx v_F/\tau_{re}$.

The process of charge separation and the formation of linear structures in the nuclei of linear defects can be described using a system of dynamic equations for the external currents of these charges according to [24] [25]. Here, for the collision of solids in the generalized space of rectangular impulses of shock loads, a discrete model of defect nuclei in crystalline materials is presented, where an undeformed perfect crystal is taken as Hilbert space of wave functions of the Schrödinger equation, and the core of a dislocation is the rigged Hilbert space of step functions as a combination of these functions of different sign, separated by a time interval. It was shown in [24] that a system of pairs of cations and photoelectrons knocked out of these cations appears in the core of a linear defect, and an intermittent field E_0^{if} in the form of a periodic sequence $E_0^{if}\delta(t)$ and $-E_0^{if}\delta(t+\tau)$ with the pulse repetition frequency ω_{rep} in the standing wave regime can interact through the chains of photoelectrons with the electron subsystem of the solid-state plasma. The features of the motion of charged particles and the interaction of chains of photoelectrons with the material's own plasma are taken out in a separate work.

Conflicts of Interest

The author declares no conflicts of interest regarding the publication of this paper.

References

[1] Cottrell, A.H. (1953) Dislocations and Plastic Flow in Crystals. 2nd Edition, Oxford University Press, Oxford.

[2] Van Buren, H.G. (1962) Defekty v kristallakh (Defects in Crystals). Izd. Inostr. Lit., Moscow.

[3] Kelly, A. and Groves, G.W. (1970) Crystallography and Crystal Defects. Longman, London.

[4] Reims, S. (1972) Theory of Many-Electron Systems. North-Holland Publishing Company, Amsterdam.

[5] Brown, R.A. (1966) Electron Distribution about an Edge Dislocation in a Metal. *Physical Review*, **141**, 568. https://doi.org/10.1103/PhysRev.141.568

[6] Oqurtani, T.O. and Huggins, R.A. (1967) Theory of Electric Field Gradient Due to Conduction Electron Charge Density Redistribution around Screw Dislocation in Metals. *Physica Status Solidi* (*b*), **24**, 301-311. https://doi.org/10.1002/pssb.19670240130

[7] Friedel, J. (1952) XIV. The Distribution of Electrons Round Impurities in Monovalent Metals. *The London, Edinburgh, and Dublin Philosophical Magazine and Journal of Science*, **43**, 153-189. https://doi.org/10.1080/14786440208561086

[8] Anokhin, A.O., Halperin, M.L., Gornostyrov, U.N., Katznelson, M.I. and Trefilov, A.V. (1994) On the Possibility of Localization of Electrons on Dislocations, Disclinations and at Grain Boundaries. *Journal of Experimental and Theoretical Physics Letters*, **59**, 344.

[9] Shuvalov, L.A., Urusovskaya, A.A., Zheludev, I.S., Zalessky, A.V., Semiletov, S.A.,

Grechushnikov, B.N., Chistyakov, I.G. and Pikin, S.A. (1981) Modern Crystallography 4: Physical Properties of Crystals (V.4). Nauka, Moscow.

[10] Landauer, R. (1951) Conductivity of Cold-Worked Metals. *Physical Review*, **82**, 520. https://doi.org/10.1103/PhysRev.82.520

[11] Orlov, A.N. (1983) Introduction to the Theory of Defects in Crystals. High School Press, Moscow.

[12] Kuzmichov, B.E. (1989) Laws and Formulas of Physics. Directory. Naukova Dumka, Kyiv.

[13] Stoneham, A.M. (1975) Theory of Defects in Solids. Electronic Structure of Defects in Insulators and Semiconductors. Claredon Press, Oxford.

[14] Akhiezer, A.I. and Berestetsky, V.B. (1969) Quantum Electrodynamics. Nauka, Moscow.

[15] Shibkov, A.A., Titov, S.A., Zheltov, M.A., Hasanov, M.F., Zolotov, A.E., Proskuryakov, K.A. and Zhigachev, A.O. (2016) Electromagnetic Emission during the Development of Macroscopically Unstable Plastic Deformation of a Metal. *Physics of the Solid State*, **58**, 1-8. https://doi.org/10.1134/S1063783416010297

[16] James, H.M. and Lark-Horovitz, K. (1951) Localized Electronic States in Bombarded Semiconductors. *Zeitschrift für Physikalische Chemie*, **198**, 107-126.

[17] Vainshtein, B.K., Fridkin, V.M. and Indenbom, V.L. (1979) Modern Crystallography Vol. 2: Structure of Crystals. Nauka, Moscow.

[18] Chernov, A.A., Givargizov, E.I., Bagdasarov, K.S., Kuznetsov, V.A., Demyanets, L.N. and Lobachev, A.N. (1980) Modern Crystallography (in 4 Volumes) V.3. The Formation of Crystals. Science, Moscow.

[19] Prokhorov, A.M. (1984) Physical Encyclopedic Dictionary. The Soviet Encyclopedia, Moscow.

[20] Honeycombe, R.W.K. (1968) The Plastic Deformation of Metals. Edward Arnold Ltd., Cambridge.

[21] Longuet-Higgins, H.C., Öpik, V., Pryce, M.H.L. and Suck, R.A. (1958) Studies of the Jahn-Teller Effect. II the Dynamical Problem. *Proceedings of the Royal Society A*, **244**, 1-16.

[22] Sloncewski, J.C. (1963) Theory of the Dynamical Jahn-Teller Effect. *Physical Review*, **131**, 1596. https://doi.org/10.1103/PhysRev.131.1596

[23] Lifshitz, I.M., Gredeskul, S.A. and Pastur, L.A. (1982) Introduction to the Theory of Disordered Media. Nauka, Moscow.

[24] Busov, V.L. (2019) Dynamic Evolution Equations for the Cores of Linear Defects of Crystalline Materials in Colliding Solids. *Physical Mesomechanics*, **22**, 91-96.

[25] Lifshits, E.M. and Pitaevsky, L.P. (1979) Theoretical Physics. V10. Physical Kinetics. Nauka, Moscow.

Scientific Research Publishing

Applied Mathematics, 2020, 11, 753-770
https://www.scirp.org/journal/am
ISSN Online: 2152-7393
ISSN Print: 2152-7385

Modeling on Metabolic Rate and Thermoregulation in Three Layered Human Skin during Carpentering, Swimming and Marathon

Dev Chandra Shrestha*, Saraswati Acharya, Dil Bahadur Gurung

Department of Mathematics, School of Science, Kathmandu University, Dhulikhel, Nepal
Email: *shresthadev28@yahoo.com

How to cite this paper: Shrestha, D.C., Acharya, S. and Gurung, D.B. (2020) Modeling on Metabolic Rate and Thermoregulation in Three Layered Human Skin during Carpentering, Swimming and Marathon. *Applied Mathematics*, **11**, 753-770.
https://doi.org/10.4236/am.2020.118050

Received: June 13, 2020
Accepted: August 18, 2020
Published: August 21, 2020

Abstract

Metabolisms play a vital role in thermoregulation in the human body. The metabolic rate varies with the activity levels and has different behaviors in nature depending on the physical activities of the person. During the activity, metabolic rate increases rapidly at the beginning and then increases slowly to become almost constant after a certain time. So, its behavior is as logistics in nature. The high metabolic rate during activity causes the increase of body core temperature up to 39˚C [1] [2]. The logistic model of metabolic rate is used to re-model Pennes' bioheat equation for the study of temperature distribution in three layered human dermal parts during carpentering, swimming and marathon. The finite element method is used to obtain the solution of the model equation. The results demonstrate that there is a significant change in tissue temperature due to sweating and ambient temperature variations.

Keywords

Pennes' Bio-Heat Equation, Metabolic Rate, Finite Element Method, Physical Activities, Thermoregulation

1. Introduction

1.1. Thermoregulation

Thermoregulation is the process of transporting thermal energy through the biochemical process in the human body. It maintains its required internal temperature. It keeps the body temperature in the equilibrium position. This process is applicable for diagnostic and therapeutic applications and involves either mass

or heat transfer. In the human body, the heat transfer is affected by blood vessel geometry, local blood flow rates, the thermal capacity of blood and produces metabolic energy. The Body regulates its temperature through internal metabolic processes and internally maintains a narrow range of internal temperature. Heat is usually generated by the metabolic process but under the condition of excessive cold, the body generates heat by shivering. Heat is lost and gained through the process of convection, radiation, blood perfusion and conduction, while evaporation contributes only heat loss from the body to the environment. Total heat loss from body surface depends on the temperature difference between skin and environment.

Hypothalamus is the main part of the brain that controls thermo-regulation. When it senses the internal temperature becoming too low or too high, it sends signals to different organs such as muscles, glands, and nervous. The body mechanism responds and helps to maintain the temperature to normal position. Different people have different thermal behaviors even in the same environment.

The biochemical processes have been divided into three broad categories: hypothermia, hyperthermia and cryobiology. Hypothermia is the phenomena in which the body core temperature falls to 35˚C or below it. This phenomenon can potentially lead to cardiac arrest, brain damage, or even death. In Hyperthermia, body core temperature rises to 42˚C or above it. Due to this phenomenon, it can suffer brain damage or even death, where cryobiology is the blood subfreezing temperature period. The average healthy person has a normal body core temperature between 36.1˚C to 37.8˚C [3]. But temperature rising up to 39.5˚C during the high intensity exercises doing on long period [1] [2]. However, if the body temperature is extreme, it can affect the body's ability to work. Thermo-regulation phenomena are affected by either environment or biological factors such as metabolic rate, dehydration, gender, etc. The internal temperature of the body rises due to fever, physical exercise and digestion of the food. Besides the internal temperature decreases due to use of alcohol, drug and some functioning of thyroid glands, etc. [4].

1.2. Circulatory System

The circulatory system also plays a vital role to maintain body temperature. The vasodilation and vasoconstriction are the two main processes which maintain heat and balanced the temperature of the body. If the body has a high temperature, the body controls the temperature and keeps in normal by occurring the mechanism of vasodilation and sweating. The blood flow rate to the skin increases by expanding the wider blood vessels under skin and heat energy dissipated by the radiation process. On the other hand, sweat glands lying under the skin surface release sweat in the form of water and vapour from the skin surface and maintain the body temperature is normal. If the body has a low temperature, it maintains the body temperature by the mechanism of vasoconstriction and thermo-genesis. The blood flow rate to the skin reduces by contracting the peripheral blood vessels lying under the skin surface and conserving heat

energy near the warm inner body and keeps the body temperature normal. Besides body muscles, organs, glands and hormones also produce heat by their mechanism.

Figure 1 represents the thermoregulation system in the human body. It shows that if the body has a low temperature, it maintains by the process of vasoconstriction and thermogenesis and if body temperature is high, it controls by the process of vasodilation and sweating to keeps the body temperature is normal.

1.3. Metabolism

The metabolic rate of a person increases due to increases in the kinetic energy and helps on increasing the temperature of the body. Some of the hormones and thyroid gland releases hormones to increase metabolism. This increased metabolism creates energy in the form of heat and maintains body temperature as normal. Basal metabolism is the minimum amount of energy release in the body to sustain life in the rest position. Body uses this energy for the circulation of blood, respiration and functioning of cells and different organs. The active person has a more metabolic rate than a less active person [5]. In general, the metabolic rate is proportional to the body weight and depends upon the type of exercises, body surface area, health, mental state, sex, thermal conductivity, age and atmospheric conditions, etc. Due to the hormones, the metabolic rate is highly increased in fever [6]. The metabolic heat produced by the exercising muscles is transported by the circulating blood to the surface of the body and released to the environment either by radiation and convection or by evaporation of sweet appears in a hot environment. According to the conservation law of energy in a healthy body, the amount of heat gain is equal to the amount of heat loss, and is given by [7]

$$M = W \pm R \pm C + E + H$$

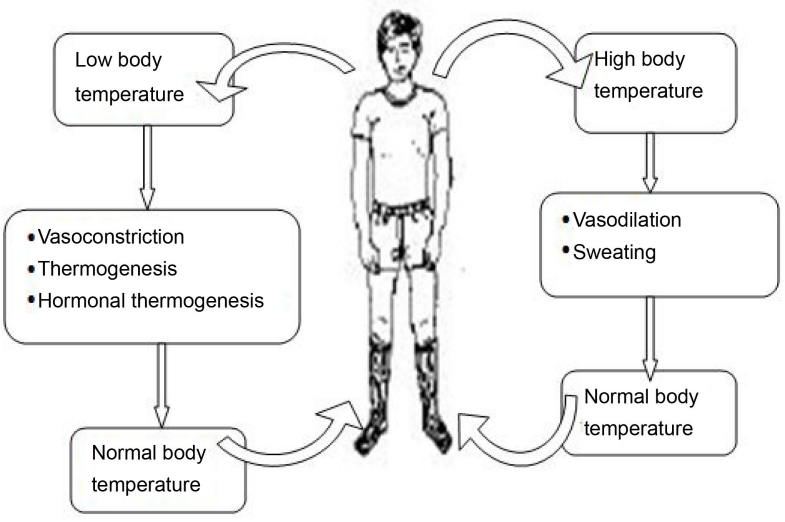

Figure 1. Schematic diagram of thermoregulation system in human body.

when the body is at rest, there is normal blood flow and metabolic activity however, during exercise there is abnormal blood flow and metabolic activity. When a person engaged in different types of physical activities, the body requires additional fuel which increases the metabolic rate and the rate of heat production [8]. The body must use its mechanism to remove the additional heat produced to keep the internal temperature at a healthy level. The body always produces heat, so the metabolic heat (M) is always positive, varying with the activity level. When environment temperature is lower than the body temperature, a thermal gradient is created which favors heat loss from the body core to the environment. That heat energy is transformed into the skin by convective blood flow and emitted by radiation, convection and sweat evaporation. The driving force of radiation and convective heat loss depends on the maintains of a large temperature gradient between the environment and body. When the environment temperature exceeds than body temperature, the gradient for heat exchange is reversed and the body gains the heat.

Different people have different thermal behavior even in the same environment. However, as environment temperature rises, sweat rate also increases. In a resting lightly clad man, the sweet begins at 29˚C environment while in the resting nude man sweating begins at the environment temperature at 31˚C [9]. Sweat evaporation becomes the primary means of heat dissipation when convective and radiative heat exchange is minimal. In a hot moist environment, a healthy man approximately 1.94 ml sweat losses from the body [10]. Being lost of heat through evaporation even an entirely high metabolic rate can also be limited by the body mechanism. If the combined heat loss from the body is less than the metabolic heat rate production of the body, the excess heat must be store in the body, but storage heat energy (H) is always small because the body has a limited thermal storage capacity. This storage heat energy helps on bring the body temperature rise and when the metabolic heat is less than combine heat loss, the body temperature falls.

During the mild exercises, the muscles are the main source of metabolic heat, and during intense exercise, it may occur up to 90% [11]. In heavy exercises, the respiration process plays the role of increasing metabolism. In low-intensity exercises as sitting, typing, cooking, etc there is very little difference in the vascular system so the metabolic rate is similar to the basal metabolic rate. While in high-intensity exercises, as marathon, wrestling, etc most of the organs come in movement with high kinetic energy so, there is a loss of energy. In moderate-intensity exercise as carpentering, driving, etc. helps on decreasing body weight by increasing cardiovascular exercise.

From the experimental data, the average basal metabolic rate (BMR) of (30 - 60) years old healthy man, of body weight 74 kg has 1737 kcal/day [12]. This shows that the BMR of the healthy human body has 1114 w/m^3, but it may vary from person to person. On the contrary to the basal metabolic energy, the body produces additional metabolic energy during the activity period. From the next experimental data, the energy consumption during different activities carpen-

tering, swimming and marathon (athletics) by a man of 65 kg weight consumed 16.7 kJ/min, (21 - 31.5) kJ/min, and 31.5 kJ/min energy respectively [13]. This data provides that the estimation value of the metabolic rate of carpentry person is 4198.08 w/m^3 and the metabolic rate of the swimming person is 6598.79 w/m^3. The scale of metabolic rate during various activities is shown in **Table 1**.

1.4. Blood Perfusion

Blood perfusion is the physiological term that refers to the process of delivery of arteries blood to a capillaries bed in the biological tissue. The arterioles and venous blood temperature may be different from the local tissue temperature. The rate of heat transfer between blood and local tissue is proportional to the product of a volumetric perfusion rate and the difference between the arterial blood temperature and the local tissue temperature [14]. This temperature may vary as a function of many transient and physiological and physical parameters. Pennes' mathematical model describes the effect of blood perfusion and metabolism on the energy balance within the tissue. These effects were incorporated into the standard thermal diffusion equation and modeled the bio-heat equation

$$\rho c\frac{\partial T}{\partial t}=\nabla\cdot\left(K\nabla T\right)+\rho_b c_b w_b\left(T_A-T\right)+S\left(t\right) \tag{1}$$

Several computer simulated methods are developed for the estimation of temperature distribution in the human body. Saxena *et al.* [15] used a variational finite element approach with linear shape function to find one dimensional unsteady temperature distribution in epidermis, dermis and subcutaneous tissues (*SST*) region assuming a rate of blood flow and rate of metabolic heat generation as a variable in the dermis part. Chao *et al.* [16] assumed two simple models and studied the temperature distribution curve in skin and subcutaneous tissue for certain paramaters values are constant. Agrawal [13] and Kenefick *et al.* [2] experimentally studied the amount of energy expenditure and blood flow rate during swimming and marathon. They estimated the maximum core temperature occurring 39.5˚C in the human body during the exercise period. Acharya *et al.* [17] divided the dermal part into six skin layers and studied the metabolic effect in thermoregulation on human males and females. The authors suggested that skin temperature in males has more than females. Khanday and Saxena [18] assumed five layered skin in the human body and used one dimensional steady state model to the estimation of cold effect on the human dermal part. Saxena and Gupta [15] and Saxena and Arya [19] contributed the papers on the effect of

Table 1. Metabolic rate of different exercises.

Type of exercises	Metabolic rate (w/m^3)
Carpentering	4198.08
Swimming	6598.79
Marathon (running)	7918.00

blood flow and heat flow in human skin and subcutaneous tissue by using variational finite element method. Kumari and Adlakha [20] developed a numerical model to study the temperature distribution in human peripheral regions incorporated the blood mass flow rate, thermal conductivity and metabolic heat generation rate were constants during and after the exercise.

Gurung *et al.* [21] investigated the temperature distribution in three layers of a human dermal part in one dimensional unsteady state with quadratic shape function assuming that the outer skin is exposed to the atmosphere. Agrawal *et al.* [22] developed a model for the temperature distribution in a human limb by assuming an irregular tapered shaped limb with a variable radius and eccentricity. Khanday [23] explained the appearance of thermal stress on the human brain tissue in hypothermic conditions. Khanday and Sexana [18] studied the thermoregulation and fluid regulation in the human head and dermal region at cold environmental conditions by using variational finite element method. K.C. *et al.* [24] investigated the thermal effect of eyelid based on the properties of ambient temperature, evaporation rate, blood temperature and lens thermal conductivity in the human eye.

Previously, developed models have not studied on the temperature distribution in the human dermal part during the exercise. So this mathematical model has presented to estimate the metabolic energy produces differently in various exercises. The main objective of this study is to investigate the temperature profiles of epidermis, dermis and subcutaneous tissues during exercise. Since the body is an irregular geometry, the finite element method is appropriate to handle such an inhomogeneous discretized problem to get realistic values of temperature of different layers.

2. Model for Metabolic Energy

During physical exercise, metabolic rate increases due to an increase in the rate of blood flow. The continuous increases in blood flow are controlled by the mechanism of the body by rapidly producing metabolic energy at the beginning of the exercise and become constant after a certain time so it is plausible to consider the metabolic rate, increasing logistically in the form similar to the logistic curve. We consider the metabolic rate $S(t)$ equation based on exercise as

$$S(t) = S_0 + \frac{\boldsymbol{E} - S_0}{1 + \mathrm{e}^{-\beta(t - t_{si})}}$$

Figure 2 represents the unsteady behavior of metabolic rates of the normal human body during the various activities in 30 minutes period. The graph shows the threshold metabolic value during the marathon is 7918 w/m^3, during swimming is 6598.79 w/m^3 and during carpentering is 4198.08 w/m^3 at $\beta = 0.01/\mathrm{s}$, and $t_{si} = 500$ s with $BMR = 1114$ w/m^3.

3. Re-Model of Bioheat Equation

Pennes' [14] and Perl [25] established the simplified bio-heat transfer model

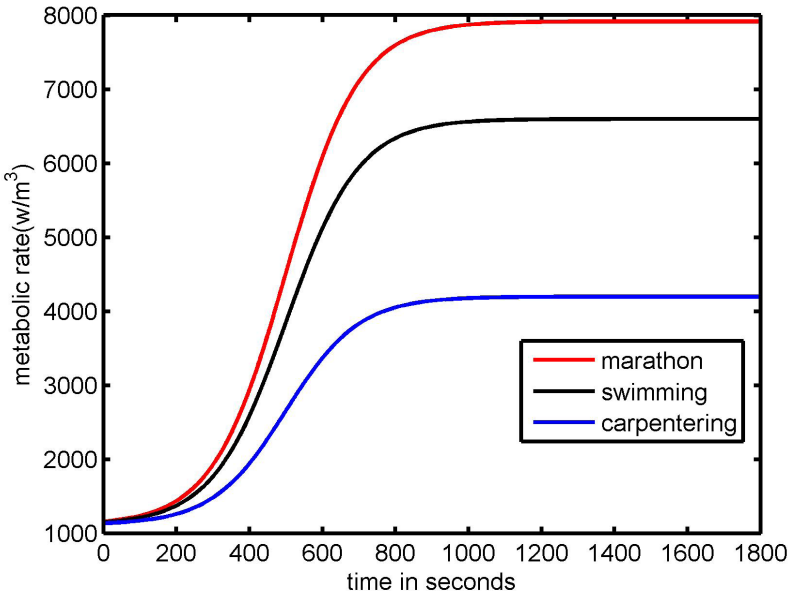

Figure 2. Metabolic rate behavior during different exercises.

equation to describe the effect of conduction, perfusion and metabolism. During the exercise period, additional heat energy arises and dissipated from the body to the environment by its mechanism. The resulting bio-heat equation with metabolic energy is re-formulated by

$$\rho c\frac{\partial T}{\partial t}=\nabla\cdot\left(K\nabla T\right)+\rho_b c_b w_b\left(T_A-T\right)+\left(S_0+\frac{E-S_0}{1+\mathrm{e}^{-\beta\left(t-t_{si}\right)}}\right) \tag{2}$$

4. Discretization of Domain

Skin is the main organ that keeps helping the temperature balance in the human body. If any illness occurs in the body, the first symptom is changing body temperature [8]. In mathematical treatments of temperature distribution in the human dermal part, the skin layers can be regarded as a physical and physiological barrier with complex structures. The three natural layers of skin are epidermis, dermis and subcutaneous tissues (*SST*). The schematic diagram of the temperature distribution model in dermal parts of the human body is shown as in **Figure 3**.

Let l_1, l_2-l_1, and l_3-l_2 be the thickness of the layers of epidermis, dermis and subcutaneous tissue respectively. Let T_0, T_1, T_2 and T_3 be the respective nodal temperatures at a distance at $x=0$, $x=l_1$, $x=l_2$ and $x=l_3$ measured from the outer surface of the skin. $T^{(1)}$, $T^{(2)}$ and $T^{(3)}$ be the temperature function of epidermis, dermis and subcutaneous tissues respectively.

5. Solution of the Model

The governing equation that characterized the heat regulation in in-vivo tissue of human body during exercises is given by the partial differential Equation (1), which we can write for 1D as;

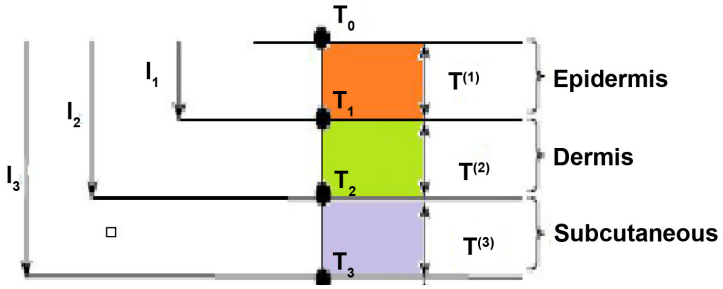

Figure 3. Schematic diagram of three layered skin.

$$\rho c\frac{\partial T}{\partial t}=\frac{\partial}{\partial x}\left(k\frac{\partial T}{\partial x}\right)+M\left(T_A-T\right)+\left(S_0+\frac{E-S_0}{1+\mathrm{e}^{-\beta\left(t-t_{si}\right)}}\right) \tag{3}$$

where, $M=\rho_b c_b w_b\left(\mathrm{J}/\mathrm{m}^3\cdot\mathrm{s}\cdot{}^{\circ}\mathrm{C}\right)$

Boundary Conditions

1) Boundary condition at $x=0$ (skin surface)

The outer surface of the skin layer is exposed to the environment during the exercise period. Therefore heat flux is dissipated for $x=0$ and heat loss takes place from the outer surface due to conduction, convection, radiation and evaporation methods. So the net heat flux is calculated by mixed boundary,

$$K\left.\frac{\partial T}{\partial x}\right|_{x=0}=h\left(T-T_\infty\right)+LE \tag{4}$$

2) Boundary condition at $x=l_3$ (body core)

During Exercise, due to the rapid movement of muscle mass and an increase in heart rate, the body produces a large amount of metabolic heat energy and cannot dissipate all energy instantaneously at that time. The rate of heat loss does not offset the rate of heat gain so some heat energy stores in the body. That excess (stored) heat energy helps to increase the body core temperature up to 39˚C. So, the Dirichlet's inner boundary condition during exercise period is taken as

$$T\left(l_3\right)=T_b=39^{\circ}\mathrm{C} \tag{5}$$

Using Euler-Lagrange formula, the variational integral form of Equation (3) and Equation (4) is given by

$$\begin{aligned}I\left[T\left(x,t\right)\right]=&\frac{1}{2}\int_\Omega\left[K\left(\frac{\mathrm{d}T}{\mathrm{d}x}\right)^2+M\left(T_A-T\right)^2-2S\left(t\right)T+\rho c\frac{\mathrm{d}T^2}{\mathrm{d}t}\right]\mathrm{d}x\\&+\frac{1}{2}h\left(T_0-T_\infty\right)^2+LET_0\cdot\end{aligned} \tag{6}$$

In the model, the physical and physiological parameters depending on the layers of dermal part and are considered as given in Table 2.

Suppose, I_1, I_2 and I_3 are the integral solutions of three layers epidermis, dermis and subcutaneous tissue, respectively with $I=\sum_{i=1}^{n}I_i$. Solving the integrals I_1, I_2 and I_3 with parameters as considered in Table 2, we obtain I_1, I_2 and I_3 as functions of nodal values T_0, T_1, T_2, as given as below:

Table 2. Assumption parameters in model.

Physical and Physiological parameters	Epidermis $l_0 \le x \le l_1$	Dermis $l_1 \le x \le l_2$	Subcutaneous $l_2 \le x \le l_3$
K	K_1	K_2	K_3
M	$M_1 = 0$	M_2	M_3
T_A	$T_A^{(1)} = 0$	$T_A^{(2)} = T_b$	$T_A^{(3)} = T_b$
$S(t)$	$S_1 = 0$	$S_2 = S_0 + \frac{E - S_0}{1 + e^{-\beta(t-t_0)}}$	$S_3 = 2\left[S_0 + \frac{E - S_0}{1 + e^{-\beta(t-t_0)}}\right]$
$T^{(i)}$	$T^{(1)} = T_0 + \left(\frac{T_1 - T_0}{l_1}\right)x$	$T^{(2)} = \frac{l_2T_1 - l_1T_2}{l_2 - l_1} + \left(\frac{T_2 - T_1}{l_2 - l_1}\right)x$	$T^{(3)} = \frac{l_3T_2 - l_2T_3}{l_3 - l_2} + \left(\frac{T_3 - T_2}{l_3 - l_2}\right)x$

$$I_1 = A_1 + B_1T_0 + D_1T_0^2 + E_1T_1^2 + F_1T_0T_1 + \alpha_1\frac{\mathrm{d}}{\mathrm{d}t}\left(T_0^2 + T_1^2 + T_0T_1\right)$$

$$I_2 = A_2 + B_2T_1 + C_2T_2 + D_2T_1^2 + E_2T_2^2 + F_2T_1T_2 + \alpha_2\frac{\mathrm{d}}{\mathrm{d}t}\left(T_1^2 + T_2^2 + T_1T_2\right)$$

$$I_3 = A_3 + B_3T_2 + C_3T_3 + D_3T_2^2 + E_3T_3^2 + F_3T_2T_3 + \alpha_3\frac{\mathrm{d}}{\mathrm{d}t}\left(T_2^2 + T_3^2 + T_2T_3\right).$$

where A_i, B_i, D_i, E_i, F_i and C_j with $1 \le i \le 3$ and $2 \le j \le 3$ are all constants whose values depend upon physical and physiological parameters of dermal part as given in Table 4. As a next step to finite element method, we differentiate I_1, I_2 and I_3 with respect to T_0, T_1 and T_2 and set $\frac{\mathrm{d}I}{\mathrm{d}T_i} = 0$, for $i = 0,1,2$. On simplification, we obtain system of equations in matrix form

$$PT + Q\dot{T} = R \tag{7}$$

where,

$$P = \begin{pmatrix} 2D_1 & F_1 & 0 \\ F_1 & 2(D_2 + E_1) & F_2 \\ 0 & F_2 & 2(D_3 + E_2) \end{pmatrix},\quad Q = \begin{pmatrix} 2\alpha_1 & \alpha_1 & 0 \\ \alpha_1 & 2(\alpha_1 + \alpha_2) & \alpha_2 \\ 0 & \alpha_2 & 2(\alpha_2 + \alpha_3) \end{pmatrix}$$

$$T = \begin{pmatrix} T_0 \\ T_1 \\ T_2 \end{pmatrix},\quad \dot{T} = \begin{pmatrix} \frac{\mathrm{d}T_0}{\mathrm{d}t} \\ \frac{\mathrm{d}T_1}{\mathrm{d}t} \\ \frac{\mathrm{d}T_2}{\mathrm{d}t} \end{pmatrix},\quad R = \begin{pmatrix} -B_1 \\ -B_2 \\ -C_2 - B_3 - F_3T_3 \end{pmatrix}$$

6. Numerical Results

The threshold values of metabolic rate during physical activities: carpentering, swimming and marathon running are 4198.08 w/m^3, 6598.79 w/m^3 and 7918 w/m^3 respectively. The values of physical and physiological parameters used for numerical simulation are taken as shown in Table 3 and Table 4.

In normal condition when the atmospheric temperature is below body core

Table 3. The thickness of human skin layers in normal position [9].

Skin layers	Epidermis layer	Dermis layer	Subcutaneous layer
Thickness (metres)	0.001	0.0035	0.005

Table 4. Parameter values used in model [9] [21].

Parameter	Value	Unit
L	2,420,220	J/kg
K_1	0.209	w/m·˚C
K_2	0.314	w/m·˚C
K_3	0.418	w/m·˚C
h	6.27	w/m^2·˚C
M_2	1254	w/m^3·˚C
M_3	1254	w/m^3·˚C
ρ_1	1050	kg/m^3
ρ_2	996	kg/m^3
ρ_3	1050	kg/m^3
c_1	3469.4	J/kg·˚C
c_2	1588.4	J/kg·˚C
c_3	1588.4	J/kg·˚C

temperature, the tissue temperature increases from the skin surface towards the body core temperature. So we consider the tissue temperature $T(x,0)$ in linear order given by the equations

$$T(x,0) = T_0 + \mu x \tag{8}$$

At normal atmospheric temperature, initial skin temperature is considered 21˚C. The use of μ in Equation (8) is constant, whose numerical value is determined by taking the known value $T_3 = T_b = 39^{\circ}\text{C}$ at $x = l_3$. We use the iterative method and the Crank-Nicolson method to solve the Equation (10). The Crank -Nicolson method gives

$$\left(Q + \frac{\Delta t}{2}P\right)T^{(i+1)} = \left(Q - \frac{\Delta t}{2}P\right)T^{(i)} + \Delta tR \tag{9}$$

Here, Δt is the time interval and $T^{(0)}$ is the initial nodal temperature in 3×1 matrix form.

For the steady case of the model, we obtain the following matrix form of the system of algebraic equations

$$PT = R \tag{10}$$

Steady State Results

The results of the analysis for dermal layers temperature distribution during marathon, swimming and carpentering in steady state are presented through Figures 4 to 6 and Table 5.

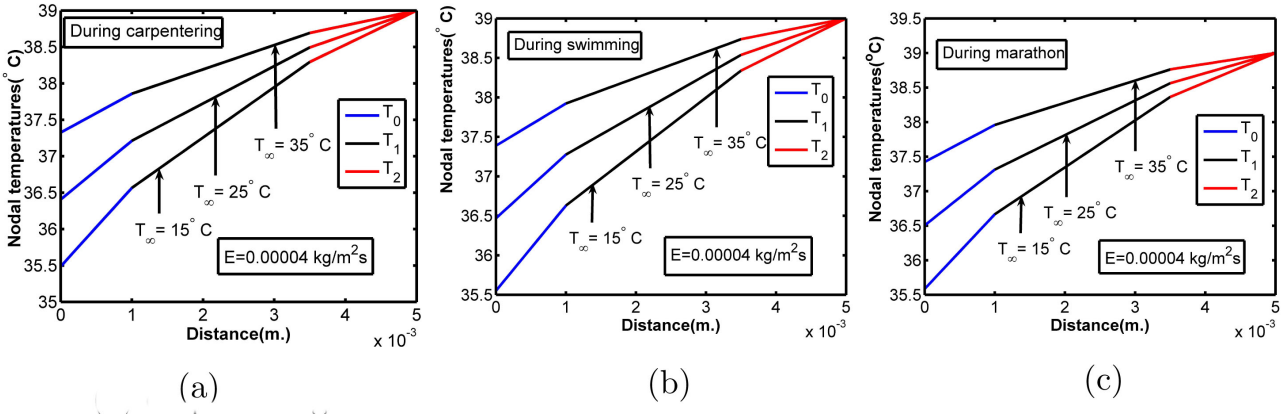

Figure 4. Estimation of epidermis, dermis and subcutaneous tissues temperature when $E = 0.00004\ \mathrm{kg/m^2 \cdot s}$ at ambient temperature 15˚C, 25˚C and 35˚C during (a) carpentering, (b) swimming and (c) marathon.

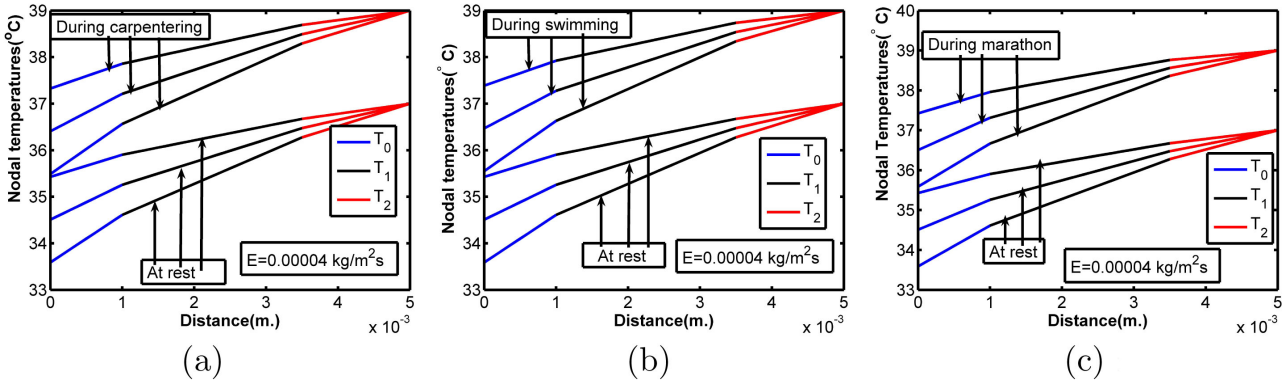

Figure 5. Estimation of epidermis, dermis and subcutaneous tissues temperature when $E = 0.00004\ \mathrm{kg/m^2 \cdot s}$ at ambient temperature 15˚C, 25˚C and 35˚C (a) during carpentering and rest, (b) during swimming and rest (c) during marathon and rest.

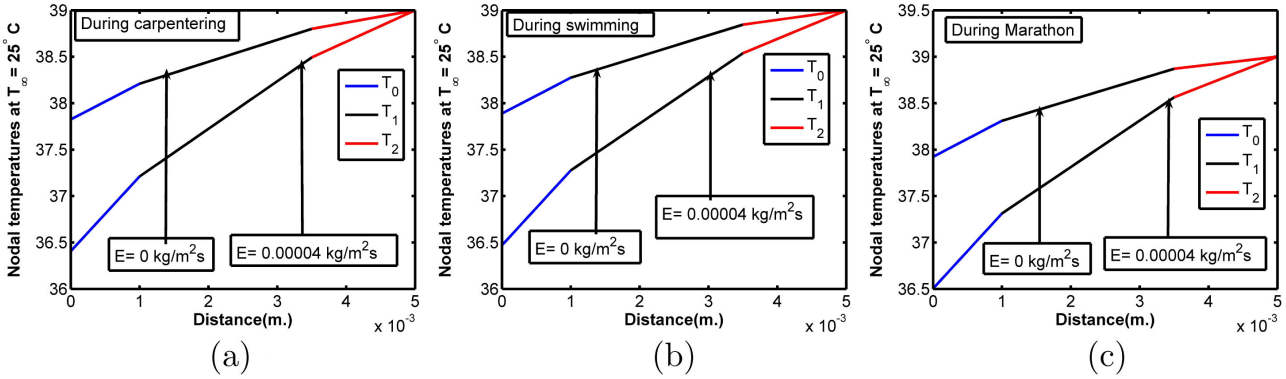

Figure 6. Estimation of epidermis, dermis and subcutaneous tissues temperature when $E = 0\ \mathrm{kg/m^2 \cdot s}$ and $E = 0.00004\ \mathrm{kg/m^2 \cdot s}$ at ambient temperature 25˚C during (a) carpentering (b) swimming and (c) marathon.

From the graph in **Figure 4** it is observed that there are significant variations in temperature distribution in the layers of skin due to change in atmospheric temperature in carpentering, swimming and marathon. But no significant changes in temperature distribution are observed during these activities at a given atmospheric temperature.

Table 5. Steady state temperature of three layered skin during carpentering, swimming, marathon and rest position at $E = 0.00004\ \mathrm{kg/m^2 \cdot s}$.

Position	Ambient temp. (˚C)	Epidermis layered temp. (˚C)	Dermis layered temp. (˚C)	subcutaneous layered temp. (˚C)
At rest	15	33.58	34.61	36.27
During carpentering	15	35.48	36.56	38.29
During swimming	15	35.54	36.63	38.33
During marathon	15	35.58	36.66	38.36
At rest	25	34.50	35.26	36.47
During carpentering	25	36.40	37.21	38.49
During swimming	25	36.46	37.28	38.53
During marathon	25	36.50	37.31	38.56
At rest	35	35.42	35.90	36.67
During carpentering	35	37.32	37.85	38.69
During swimming	35	37.38	37.92	38.73
During marathon	35	37.42	37.95	38.76

From the graph in **Figure 5(a)**, it is observed that the epidermis layer has more temperature by 1.90˚C, the dermis layer has more temperature by 1.95˚C and subcutaneous tissue has more temperature by 2.02˚C at $E = 0.00004\ \mathrm{kg/m^2 \cdot s}$ and at each ambient temperature $T_\infty = 15^\circ\mathrm{C}$, 25˚C and 35˚C during carpentering than rest position.

From the graph in **Figure 5(b)**, the result shows that the epidermis layer has more temperature by 1.96˚C, the dermis layer has more temperature by 2.02˚C and subcutaneous tissue has more temperature by 2.06˚C at $E = 0.00004\ \mathrm{kg/m^2 \cdot s}$ and at each ambient temperature $T_\infty = 15^\circ\mathrm{C}$, 25˚C and 35˚C during swimming than rest position.

From the graph in **Figure 5(c)**, it is observed that the epidermis layer has more temperature by 2.00˚C, the dermis layer has more temperature by 2.05˚C and subcutaneous tissue has more temperature by 2.09˚C at $E = 0.00004\ \mathrm{kg/m^2 \cdot s}$ and at each ambient temperature $T_\infty = 15^\circ\mathrm{C}$, 25˚C and 35˚C during marathon than rest position.

From the graph in **Figures 6(a)-(c)**, it is observed that each skin layer has more temperature at $E = 0\ \mathrm{kg/m^2 \cdot s}$ than at $E = 0.00004\ \mathrm{kg/m^2 \cdot s}$ at fixed environment temperature 25˚C in carpentering, swimming and marathon. This shows that temperature of dermal layer control by producing the essential sweat from the body when the environment temperature is high during the activities.

In the present **Table 5**, the table shows the steady state temperature of three skin layered during different activities at various ambient temperatures. The temperature of each dermal layer during the marathon is more than swimming and carpentering at each ambient temperature 15˚C, 25˚C, and 35˚C. The temperature of each dermal layer during swimming is more than carpentering due

to different metabolic rates at the same ambient temperature.

Unsteady State Results

The graphs of unsteady steady case for atmospheric temperatures, $T_\infty = 15^\circ\text{C}$, 25˚C and 35˚C are presented in Figures 7 to 9 and it's numerical results are shown in Table 6 and Table 7.

Figure 7 represents the tissue temperatures during the different activities at

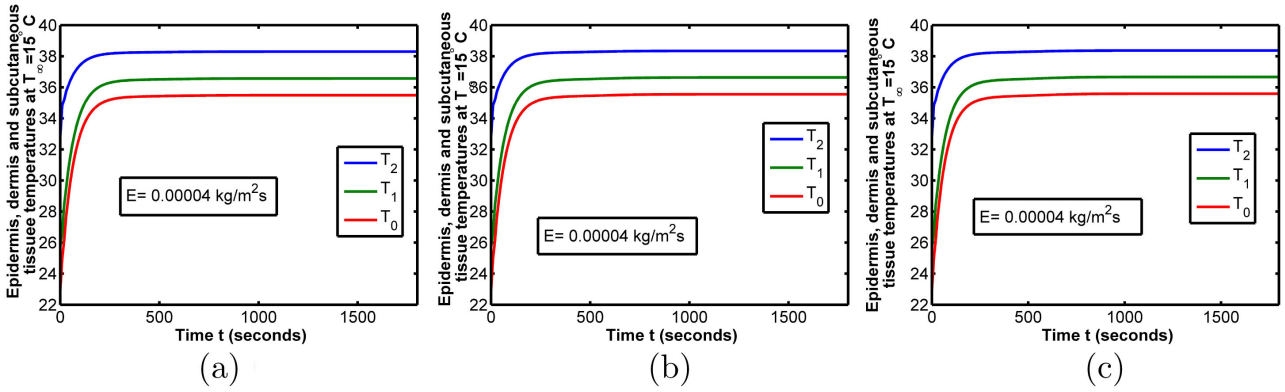

Figure 7. Estimation of the epidermis, dermis and subcutaneous tissue temperatures at $T_\infty = 15^\circ\text{C}$ and $E = 0.00004\ \text{kg}/\text{m}^2\cdot\text{s}$ during (a) carpentering, (b) swimming and (c) marathon.

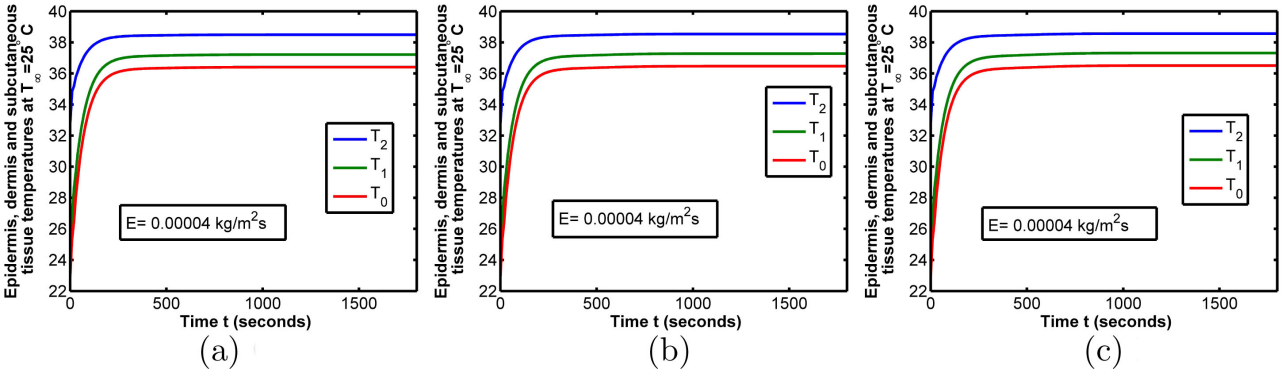

Figure 8. Observation of the epidermis, dermis and subcutaneous tissue temperatures at $E = 0.00004\ \text{kg}/\text{m}^2\cdot\text{s}$ and $T_\infty = 25^\circ\text{C}$ during (a) carpentering, (b) swimming and (c) marathon.

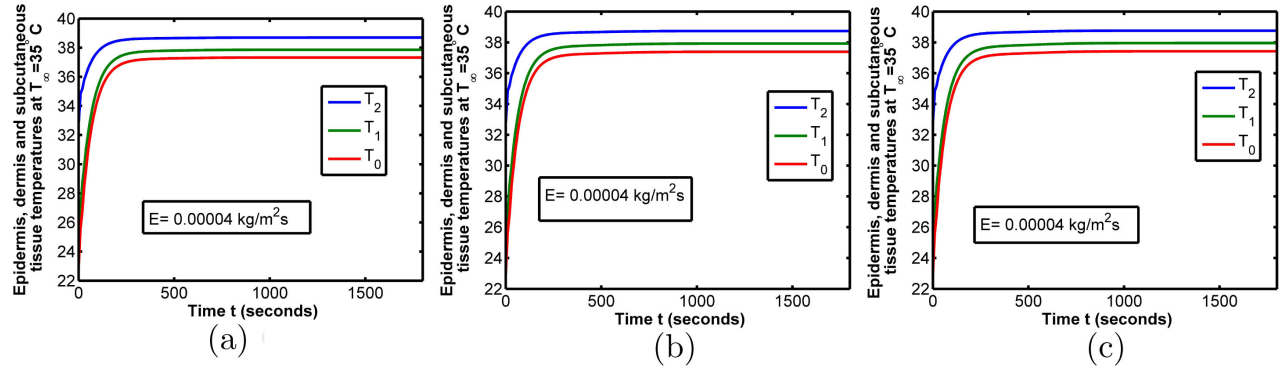

Figure 9. Estimation of epidermis, dermis and the subcutaneous tissue temperatures at $E = 0.00004\ \text{kg}/\text{m}^2\cdot\text{s}$ $T_\infty = 35^\circ\text{C}$ during (a) carpentering, (b) swimming and (c) marathon.

$T_\infty = 15^\circ\text{C}$. The results show the temperatures in the epidermis layer increased to 35.48˚C, 35.54˚C and 35.58˚C, temperatures in the dermis layer increased to 36.56˚C, 36.63˚C and 36.66˚C and temperatures in the subcutaneous tissue increased to 38.29˚C, 38.33˚C and 38.36˚C at $E = 0.00004\ \text{kg}/\text{m}^2 \cdot \text{s}$ during carpentering, swimming and marathon respectively.

On observing Figure 8, at $T_\infty = 25^\circ\text{C}$ and $E = 0.00004\ \text{kg}/\text{m}^2 \cdot \text{s}$, the subcutaneous tissue temperature is greater by 3.20˚C than epidermis layer and is greater by 1.97˚C than dermis layer temperatures during carpentering. The subcutaneous tissue temperature is greater by 3.18˚C than the epidermis and is greater by 1.96˚C than dermis layer temperatures during swimming. During the marathon, the subcutaneous tissue temperature is greater by 3.17˚C than the epidermis and is greater by 1.94˚C than dermis layer temperatures. These results exhibit that subcutaneous tissue temperature is higher than dermis and epidermis layers because subcutaneous tissue is nearer from the body core with constant body core temperature.

Figure 9 reveals the temperatures variation between the dermis and subcutaneous tissue is higher than the temperatures variations between the epidermis and dermis layers at $T_\infty = 35^\circ\text{C}$ and $E = 0.00004\ \text{kg}/\text{m}^2 \cdot \text{s}$ during carpentering, swimming and marathon.

In present Table 6, the maximum temperatures of epidermis, dermis and subcutaneous tissue respectively are raised to 37.42˚C, 37.95˚C and 38.76˚C during the marathon, 37.38˚C, 37.92˚C and 38.73˚C during swimming and 37.32˚C, 37.85˚C and 38.69˚C during carpentering at ambient temperature 35˚C and $E = 0.00004\ \text{kg}/\text{m}^2 \cdot \text{s}$ .These results execute that the temperature of each skin layer increases due to the rise in the metabolic rate during the exercises. Table 7 represents the temperatures of epidermis, dermis, and subcutaneous tissue during different physical activities at different ambient temperatures and $E = 0.00008\ \text{kg}/\text{m}^2 \cdot \text{s}$. The table shows the maximum temperatures of epidermis, dermis, and subcutaneous tissue respectively increase to 36.00˚C, 36.96˚C and 38.45˚C during marathon, increase to 35.96˚C, 36.92˚C, and 38.42˚C, during swimming and increase to 35.90˚C, 36.85˚C, and 38.38˚C during carpentering at ambient temperature 35˚.

On comparing Table 6 and Table 7, the results exhibit that the temperature of the skin layers fall due to loss of more heat energy in the form of sweat at high sweat rate.

Table 6. Estimation of the unsteady state skin layers temperature at $E = 0.00004\ \text{kg}/\text{m}^2 \cdot \text{s}$ during carpentering, swimming and marathon.

Ambient temperature	Temperature during carpentering			Temperature during swimming			Temperature during marathon		
(T_∞)	T_0	T_1	T_2	T_0	T_1	T_2	T_0	T_1	T_2
15˚C	35.48	36.56	38.29	35.54	36.63	38.33	35.58	36.66	38.36
25˚C	36.40	37.21	38.49	36.46	37.28	38.53	36.50	37.31	38.56
35˚C	37.32	37.85	38.69	37.38	37.92	38.73	37.42	37.95	38.76

Table 7. Estimation of the unsteady state skin layers temperature at $E = 0.00008\ \mathrm{kg/m^2 \cdot s}$ during carpentering, swimming and marathon.

Ambient temperature	Temperature during carpentering			Temperature during swimming			Temperature during marathon		
(T_∞)	T_0	T_1	T_2	T_0	T_1	T_2	T_0	T_1	T_2
15˚C	34.06	35.56	37.98	34.13	35.63	38.03	34.16	35.66	38.05
25˚C	34.98	36.21	38.18	35.05	36.27	38.23	35.08	36.31	38.25
35˚C	35.90	36.85	38.38	35.96	36.92	38.42	36.00	36.96	38.45

7. Discussion and Conclusion

The metabolic rate increases due to increases of the oxygen consumption by the body during physical activities. It helps to increase the temperature of the body. When the environment temperature increases, the metabolic rate in the body decreases. In the human body, the normal core temperature is 37˚C so, on or above 37˚C, the body produces negligible metabolic heat [17]. In this model, the ambient temperatures 15˚C, 25˚C and 35˚C are taken.

More active physical activity produces more sweat due to the fast movement of muscle mass. The analysis also shows, carpentering produces less metabolic energy than swimming and swimming produces less metabolic energy than the marathon. In this model sweat release rates on the exercises are taken as 0.00004 kg/m^2s and 0.00008 kg/m^2s.

Figures 7-9 exhibit that the temperatures of epidermis, dermis and subcutaneous tissue increase rapidly at the beginning and reach to the steady temperatures after a certain period. These figures also reveal that the subcutaneous tissue temperatures reach earlier to steady temperatures than epidermis and dermis temperatures. This is due to increase of the metabolic rate on increasing the lean muscle mass and lose adipose fat tissue in subcutaneous tissue during activities. These results also demonstrate that the steady-state temperature of each dermal layer is achieved more during the marathon than swimming and carpentering due to more metabolic rate during the marathon. The unsteady and steady both results execute that the environment temperature gives significant changes in temperature in human dermal part.

The above result suggests that the temperature of each node increases by decreasing the sweat evaporation rate and vice versa at the same ambient temperature. This shows that the sweat evaporation rate is the catalyst in the thermoregulation process. All of the previous researchers developed models have not determined the temperature distribution in human dermal part by the computational method during the activity period. So this model is developed for the temperature distribution in dermal parts of human body during activities. The thermal effect of physical activities is quite significant. It also uses to develop models regarding physical work for labourers, military, other sports persons, etc. based on their physical and physiological characters.

Conflicts of Interest

The authors declare no conflicts of interest regarding the publication of this paper.

References

[1] Alexiou, S. (2014) The Effect of Water Temperature on the Human Body and the Swimming Effort. *Biology of Exercise*, **10**, 9-26.

[2] Kenefick, R.W., Cheuvront, S.N. and Sawka, M.N. (2007) Thermo-Regulatory Function during the Marathon. *Sports Medicine*, **37**, 312-315. https://doi.org/10.2165/00007256-200737040-00010

[3] Fernandes, A., *et al.* (2014) Measuring Skin Temperature before, during and after Exercise, a Comparison of Thermocouple and Infrared Thermography. *Physiological Measurement*, **35**, 189-203. https://doi.org/10.1088/0967-3334/35/2/189

[4] Mayers, G.E. (1981) Alcohol's Effect of Body Temperature, Hyporthermia, Hyperthermia and Poikilothermia. *Brain Research Bulletin*, **7**, 209-220. https://doi.org/10.1016/0361-9230(81)90085-X

[5] Acharya, S., Gurung, D.B. and Saxena, V.P. (2013) Effect of Metabolic Reaction on Thermo-Regulation in Human Male and Female Body. *Applied Mathematics*, **4**, 39-48. https://doi.org/10.4236/am.2013.45A005

[6] Kimberly Holland, K. (2016) Thermoregulation, Healthline. University of Illinois, College of Medicine, Champaign.

[7] Tansey, E.A. and Johnson, C.D. (2015) Recent Advances in Thermoregulation. *Advances in Physiology Education*, **39**, 139-148. https://doi.org/10.1152/advan.00126.2014

[8] Gurung, D.B. and Shrestha, D.C. (2016) Mathematical Study of Temperature Distribution in Human Dermal Part during Physical Exercises. *Journal of the Institute of Engineering*, **12**, 63-76. https://doi.org/10.3126/jie.v12i1.16727

[9] Gurung, D.B. (2007) Mathematical Study of Abnormal Thermo-Regulation in Human Dermal Part. Ph.D. Thesis, Kathmandu University, Dhulikhel.

[10] Sawka, M.N., *et al.* (1993) Nutritional Needs in Hot Environments. The National Academics of Sciences, Engineering and Medicine, National Academy Press, Washington DC, Ch. 1, 3-44.

[11] Diaz, M.D. and Becker, D.E. (2010) Physiological and Clinical Considerations during Sedation and General Anesthesia, American Dental Society of Anesthesiology. *Anesthesia Progress*, **57**, 25-33. https://doi.org/10.2344/0003-3006-57.1.25

[12] Durnin, J.V.G.A. (1992) Energy Metabolism in the Elderly. In: *Nutrition of the Elderly*, Nutrition Workshop Series, Vol. 29, Raven, New York, 51-63.

[13] Agrawal, D.C. (1999) Work and Heat Energy Expenditure during Swimming. *Physical Education*, **34**, 220-226. https://doi.org/10.1088/0031-9120/34/4/309

[14] Pennes, H.H. (1948) Analysis of Tissue and Arterial Blood Temperature in Resting Human Forearm. *Journal of Applied Physiology*, **1**, 93-122. https://doi.org/10.1152/jappl.1948.1.2.93

[15] Saxena, V.P. and Gupta, M.P. (1994) Variational Finite Element Method Heat Flow Problems in Human Limbs. *International Journal of Mathematics and Mathematical Sciences*, **17**, 771-778. https://doi.org/10.1155/S0161171294001079

[16] Chao, K.N., Eisley, J.G. and Yang, W.J. (1973) Heat and Water Migration in Regional Skins and Subcutaneous Tissue. *Proc. Bio. Mech. Symp.* (*ASME*), 69-72.

[17] Acharya, S., Gurung, D.B. and Saxena, V.P. (2015) Two Dimensional Finite Element Method for Metabolic Effect in Thermoregulation on Human Males and Females Skin Layers. *Journal of Coastal Life Medicine*, **3**, 623-629. https://doi.org/10.12980/JCLM.3.2015J5-38

[18] Khanday, M.A. and Saxena, V.P. (2009) Finite Element Approach for the Study of Thermoregulation in Human Head Exposed to Cold Environment. *AIP Conference Proceedings*, **1146**, 375-385. https://doi.org/10.1063/1.3183555

[19] Saxena, V.P. and Arya, D. (1988) Unsteady State Heat Flow in Epidermis and Dermis of a Human Body. *Indian Academy of Sciences* (*Math. Sci.*), **98**, 71-80. https://doi.org/10.1007/BF02880973

[20] Kumari, B. and Adlaka, N. (2013) One Dimensional Finite Difference Model to Study Temperature Distribution in Peripheral Regions of a Human Body during and after Exercise. *Journal of Medical Imaging and Health Informatics*, **3**, 179-186. https://doi.org/10.1166/jmihi.2013.1153

[21] Gurung, D.B., Saxena, V.P. and Adhikari, P.R. (2009) FEM Approach to One Dimensional Unsteady State Temperature Distribution in Human Dermal Parts with Quadratic Shape Function. *Journal of Applied Mathematics and Informatics*, **27**, 301-331.

[22] Agrawal, M., Pardarsani, K.R. and Adlaka, N. (2014) State Temperature Distribution in Dermal Regions of an Irregular Tapered Shaped Human Limb with Variable Eccentricity. *Journal of Thermal Biology*, **44**, 27-34. https://doi.org/10.1016/j.jtherbio.2014.06.004

[23] Khanday, M.A. (2013) Theoretical Approach to Study the Thermal Stress on the Human Brain Tissue in Hypothermic Conditions. *International Journal of Advanced Computer and Mathematical Sciences*, **4**, 181-187.

[24] Gurung, D.B., Adhikari, P.R., *et al.* (2014) Thermal Effect of the Eyelid in Human Eye Temperature Model. *Journal of Applied Mathematics and Informatics*, **32**, 649-663. https://doi.org/10.14317/jami.2014.649

[25] Perl, W. (1962) Heat and Matter Distribution in Body Tissues and the Determination of Tissue Blood Flow by Local Clearance Method. Journal of Theoretical Biology, **2**, 201-235. https://doi.org/10.1016/0022-5193(62)90025-5

Nomenclature

H	Metabolic heat produced during exercise
W	Heat amount used to perform external work
R	Heat radiation
C	Conductive and convective heat
E	Evaporative heat loss
H	Heat storage
c	Tissue specific heat capacity
K	Tissue thermal conductivity
$S(t)$	Metabolic rate during exercise
L	Latent heat capacity
h	Combined heat transfer coefficient due to convection and radiation
K_1	Thermal conductivity of the epidermis layer
K_2	Thermal conductivity of the dermis layer
K_3	Thermal conductivity of the subcutaneous tissue
c_1	Specific heat capacity of epidermis layer
c_2	Specific heat capacity of dermis layer
c_3	Specific heat capacity of subcutaneous tissue
l_1	Thickness of epidermis layer
l_2	Thickness of epidermis and dermis layers
l_3	Total thickness of skin and subcutaneous tissue
M_1	Blood mass flow in epidermis layer
M_2	Blood mass flow in dermis layer
M_3	Blood mass flow in subcutaneous tissue
S_1	Metabolic rate in epidermis layer
S_2	Metabolic rate in dermis layer
S_3	Metabolic rate in subcutaneous tissue
w_b	Blood perfusion rate
c_b	Blood specific heat capacity
ρ	Tissue density
ρ_b	Blood density
ρ_1	Density of epidermis layer
ρ_2	Density of dermis layer
ρ_3	Density of subcutaneous tissue
Ω	Domain of layered skin
β	Exercise controlled parameter
T	Tissue temperature
T_A	Arterial blood temperature
T_∞	Ambient temperature
T_b	Body core temperature
S_0	Basal metabolic rate
E	Exercise threshold metabolism
t	Exercise time period
t_{si}	Sigmoid's mid point of the curve over the time for extensive exercise

Scientific Research Publishing

Applied Mathematics, 2020, 11, 771-778
https://www.scirp.org/journal/am
ISSN Online: 2152-7393
ISSN Print: 2152-7385

Mean Difference and Mean Deviation of Tukey Lambda Distribution

Giovanni Girone[1], Antonella Massari[2], Fabio Manca[3], Angela Maria D'Uggento[4*]

[1]Faculty of Economics, University of Bari, Largo Abbazia S. Scolastica, Bari, Italy
[2]Department of Economics, Management and Business Law, University of Bari, Largo Abbazia S. Scolastica, Bari, Italy
[3]Department of Education, Psychology, Communication, University of Bari, Bari, Italy
[4]Department of Economics and Finance, University of Bari, Largo Abbazia S. Scolastica, Bari, Italy
Email: giovanni.girone@uniba.it, antonella.massari@uniba.it, fabio.manca@uniba.it, *angelamaria.duggento@uniba.it

How to cite this paper: Girone, G., Massari, A., Manca, F. and D'Uggento, A.M. (2020) Mean Difference and Mean Deviation of Tukey Lambda Distribution. *Applied Mathematics*, **11**, 771-778.
https://doi.org/10.4236/am.2020.118051

Received: July 1, 2020
Accepted: August 21, 2020
Published: August 24, 2020

Abstract

The purpose of this paper is to broaden the knowledge of mean difference and, in particular, of an important distribution model known as Tukey lambda, which is generally used to choose a model to fit data. We have obtained compact formulas, which are not yet reported in literature, of mean deviation and mean difference related to the said distribution model. These results made it possible to analyze the relationships among variability indexes, namely standard deviation, mean deviation and mean difference, regarding Tukey lambda model.

Keywords

Mean Difference, Mean Deviation, Tukey Lambda Distribution, Variability Indexes' Relationships

1. Introduction

The purpose of this work is to increase the methodological contributions on the mean difference and on the relationships of the mean difference with other variability indexes [1] [2]. The studies on the mean difference, introduced by Corrado Gini in 1912 as a measure of the variability of the characters according to the aspect of inequality, have aroused the interest of many scholars over years and also recently [3] [4]. The importance of mean difference is also due to the fact that the sample mean difference is a correct estimate of that of the population distribution model and, therefore, functional for inferential purposes [5]. The theoretical contributions on the mean difference concern the main continuous distribution models (normal, rectangular, exponential, ...) [6], however, for other

distribution models, such as Tukey's, no contributions are known in literature.

2. Tukey Lambda Distribution

Tukey lambda distribution is usually used to choose a distribution model to fit data and its direct use is less usual. In general, its characteristic is that neither its density function $f(x)$ nor its cumulative function $F(x)$ is known, but only the inverse of this latter $F^{-1}(x)$, that is the quantile function $Q(p)$ [7] [8].

A complete Tukey distribution shape includes three parameters: one of position, one of scale and one of shape [9] [10].

In order to calculate the mean difference and the mean deviation, it is better to refer to a reduced distribution in which the position parameter is set to zero and the scale to one. Formulas of mean difference and mean deviation of complete distribution are equal to the ones of reduced distribution multiplied by the scale parameter value. Tukey lambda distribution is defined by the quantile function

$$x = Q(p) = \frac{p^{\lambda} - (1-p)^{\lambda}}{\lambda}, \quad 0 < p < 1. \tag{1}$$

Said function is not always analytically invertible and, therefore, allows to obtain cumulative function and density function only for some values of λ [11] which are $\lambda = -1, 0, 1/4, 1/3, 1/2, 1, 3/2, 2, 3, 4$. Cumulative functions of Tukey lambda distribution for such values are listed below:

$$\lambda = -1,\ F(x) = \frac{-2 + x + \sqrt{4 + x^2}}{2x},\ -\infty < x < \infty \tag{2}$$

$$\lambda = 0,\ F(x) = \frac{1}{1 + \mathrm{e}^{-x}},\ -\infty < x < \infty \tag{3}$$

$$\lambda = \frac{1}{4},\ F(x) = \frac{1}{2} + \frac{x}{512}\sqrt{-3584x^2 - 17x^6 + \left(1024 + 12x^4\right)\sqrt{512 + 2x^4}},\ -4 < \lambda < 4 \tag{4}$$

$$\lambda = \frac{1}{3},\ F(x) = \frac{1}{2} - \frac{5x^3}{216} + \frac{x^5}{72\left(5832 + x^6 + 108\sqrt{2916 + x^6}\right)^{1/3}} + \frac{x}{72}\left(5832 + x^6 + 108\sqrt{2916 + x^6}\right)^{1/3},\ -3 < x < 3 \tag{5}$$

$$\lambda = \frac{1}{2},\ F(x) = \frac{1}{8}\left(4 - x\sqrt{8 - x^2}\right),\ -2 < x < 2 \tag{6}$$

$$\lambda = 1,\ F(x) = \frac{1 + x}{2},\ -1 < x < 1 \tag{7}$$

$$\lambda = \frac{3}{2},\quad F(x) = \frac{1}{2}\left[1 - \sqrt{-2 + \frac{1 + 18x^2}{\left(1 - 45x^2 - \frac{81x^4}{2} + \frac{3}{2}x\sqrt{\left(-4 + 9x^2\right)^3}\right)^{1/3}} + \left(1 - 45x^2 - \frac{81x^4}{2} + \frac{3}{2}x\sqrt{\left(-4 + 9x^2\right)^3}\right)^{1/3}}\right],\ -\frac{2}{3} < x < \frac{2}{3} \tag{8}$$

$$\lambda = 2, F(x) = \frac{1+2x}{2}, -\frac{1}{2} < x < \frac{1}{2} \tag{9}$$

$$\lambda = 3, F(x) = \frac{1}{2}\left(1 - \frac{1}{\left(6x+\sqrt{1+36x^2}\right)^{1/3}} + \left(6x+\sqrt{1+36x^2}\right)^{1/3}\right), -\frac{1}{3} < x < \frac{1}{3} \tag{10}$$

$$\lambda = 4, F(x) = \frac{1}{2}\left(1 - \frac{1}{3^{1/3}\left(36x+\sqrt{3}\sqrt{1+432x^2}\right)^{1/3}} + \frac{\left(36x+\sqrt{3}\sqrt{1+432x^2}\right)^{1/3}}{3^{2/3}}\right), -\frac{1}{4} < x < \frac{1}{4} \tag{11}$$

It is necessary to use numerical inversion of $Q(p)$ to get a cumulative function for other λ values.

Regarding Tukey distribution, some characteristic values as function of λ are known: average, mode, median, standard deviation, asymmetry index, disnormality excess index, entropy, characteristic function. Expressions of mean difference and mean deviation are unknown.

3. Variability Indexes of Tukey Lambda Distribution

The variance of Tukey lambda distribution as a function of λ parameter [12] is

$$\sigma^2 = \frac{2}{\lambda^2}\left[\frac{1}{1+2\lambda} - \frac{\Gamma(\lambda+1)^2}{\Gamma(2\lambda+2)}\right], \lambda > -\frac{1}{2}. \tag{12}$$

By using the cumulative functions derived by the inversion of quantile functions of Tukey lambda distribution, mean difference and mean deviation values are obtained and shown in **Table 1**.

Mean difference values for integers from 1 to 10 are arranged exactly on a parabolic hyperbola

$$\Delta(\lambda) = \frac{4}{2+3\lambda+\lambda^2}, \lambda > 1. \tag{13}$$

Some values of Δ calculated numerically for other values of λ parameter are also all arranged over the said function, which can be then considered a general expression of the mean difference of Tukey lambda distribution. Said function takes not-negative finite values for $\lambda > -1$, as it can be shown in **Figure 1**.

Therefore, the mean difference in Tukey lambda distribution has a domain $\lambda > -1$ which is wider than the one of standard deviation $\lambda > -1/2$.

Let us now consider the mean deviation. First of all, we can see that the average of our distribution exists only for $\lambda > -1$ and, therefore, said domain also applies to mean deviation. Mean deviation values for integers from 1 to 10 are arranged exactly over the function

$$\delta(\lambda) = \frac{2^{1-\lambda}\left(2^{\lambda}-1\right)}{\lambda(\lambda+1)}, \lambda > -1. \tag{14}$$

Values of δ calculated numerically for other values of λ parameter are also all arranged exactly over the said function, which can be then considered the expression

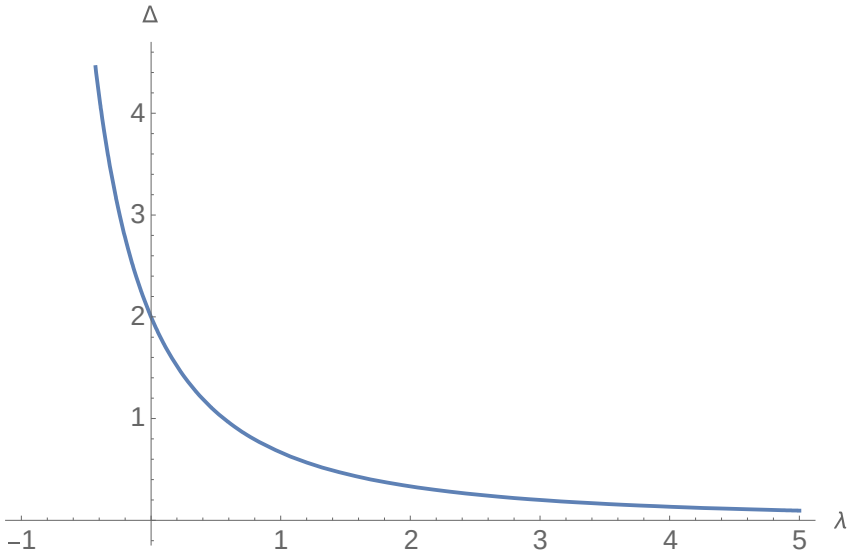

Figure 1. Mean difference of Tukey lambda distribution as a function of λ parameter.

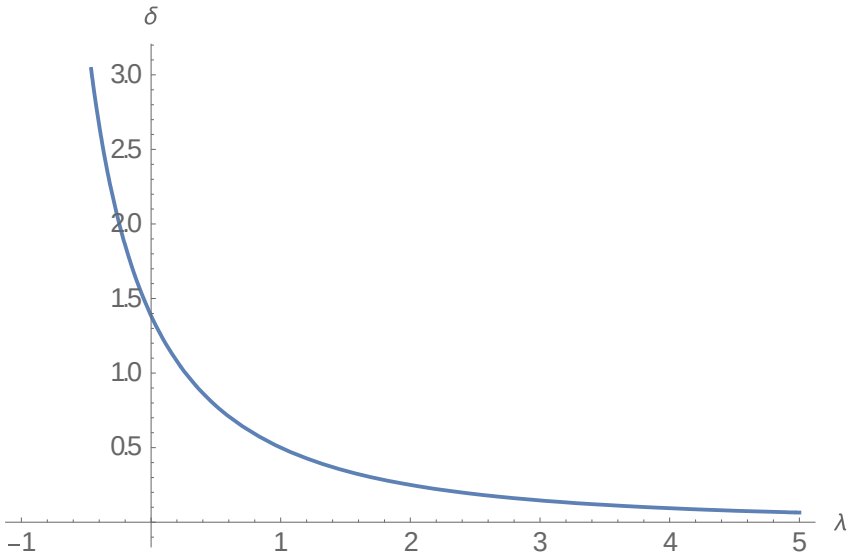

Figure 2. Mean deviation of Tukey lambda distribution as a function of λ parameter.

Table 1. Values of mean difference and mean deviation for some values of λ parameter in Tukey lambda distribution.

λ	Δ	Δ
−1	∞	∞
−4/5	50/3	9.263764082403105
−3/4	64/5	7.27245685874591
−2/3	9	5.240144005205601
−3/5	50/7	4.297623404313451
−1/2	16/3	3.3137084989847696
−1/3	18/5	2.339289449053423

Continued

−1/4	64/21	2.0182092266958453
0	2	2log2
1/4	64/65	1.018262942376231
1/3	9/7	0.9283476330715509
1/2	16/15	$\frac{4}{3}\left(2-\sqrt{2}\right)$
3/5	25/26	0.7088459262782351
2/3	9/10	0.6660710550945809
3/4	64/77	0.6177469599979266
1	2/3	1/2
3/2	16/35	0.34477152501692165
2	1/3	1/4
5/2	16/63	0.1881653270194103
3	1/5	7/48
4	2/15	3/32
5	2/21	31/480
6	1/14	3/64
7	1/18	127/3584
8	2/45	85/3072
9	2/55	511/23040
10	1/33	93/5120

of mean deviation of the Tukey lambda distribution. Said function takes not-negative finite values for $\lambda > -1$ as it can be shown in **Figure 2**.

The mean deviation of Tukey lambda distribution has, therefore, a domain wider than the one of standard deviation.

4. Relations between Variability Indexes of Tukey Lambda Distribution

By inverting the expression of mean difference in Tukey lambda distribution as a function of λ parameter (13), the following two roots come out

$$\lambda_1 = \frac{-3\Delta + \sqrt{\Delta}\sqrt{16+\Delta}}{2\Delta} \tag{15}$$

and

$$\lambda_2 = \frac{-3\Delta - \sqrt{\Delta}\sqrt{16+\Delta}}{2\Delta}. \tag{16}$$

The second solution, which is always negative, is not usable to obtain the relationship between Δ and σ [13].

By substituting the first solution λ_1 (15) in the standard deviation expression, it comes out an analytical relationship of the same one related to the mean difference of Tukey lambda distribution:

$$\sigma = \frac{2\sqrt{\frac{2}{\sqrt{16/\Delta+1}-2} - \frac{2\Gamma\left[\frac{1}{2}\left(\sqrt{16/\Delta+1}-1\right)\right]^2}{\Gamma\left[\sqrt{16/\Delta+1}-1\right]}}}{\sqrt{16/\Delta+1}-3}, \Delta > 0. \quad (17)$$

Said relationship is represented in Figure 3.

As it can be seen, standard deviation increases quickly when mean difference increases.

Let us, now, consider the relationship between mean difference and mean deviation.

By substituting root λ_1 in the formula of mean deviation (14), it comes out the following analytical relationship

$$\delta(\Delta) = \frac{2\left(2^{\frac{3}{2}-\frac{\sqrt{\frac{16}{\Delta}+1}}{2}} - 1\right)}{\sqrt{\frac{16}{\Delta}+1}-\frac{4}{\Delta}-1}, \Delta > 0. \quad (18)$$

As shown in Figure 4, it is evident that the relationship between the two indexes is almost linear.

Finally, let us consider the relationship between mean deviation and standard deviation of Tukey lambda distribution.

Since it is not possible to obtain λ parameter as a function of mean deviation, it is necessary to use a numerical procedure to calculate the two variability indexes values for a consistent set of λ parameter values and to represent pairs of values on a Cartesian axis.

By choosing values of λ: −0.49, −0.48, ..., 5.00, it comes out a numerical relationship as shown in Figure 5.

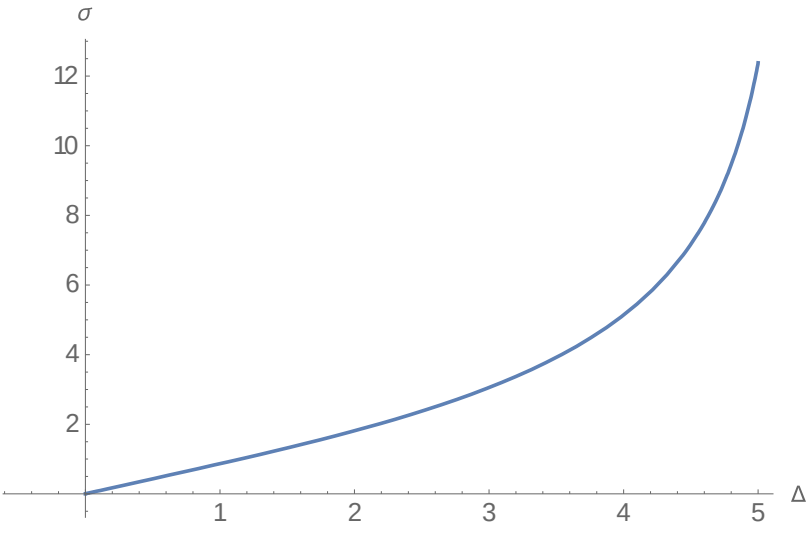

Figure 3. Analytical relationship between mean difference and standard deviation of Tukey lambda distribution.

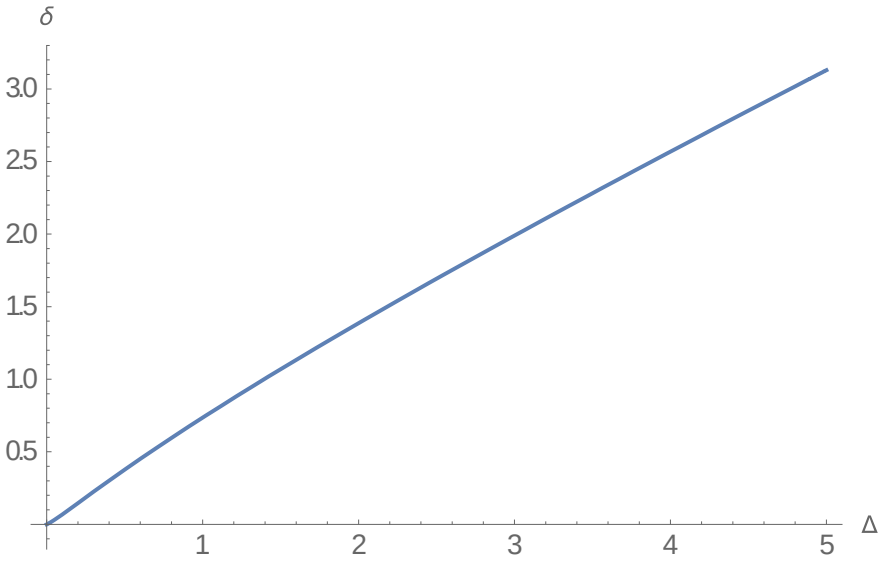

Figure 4. Analytical relationship between mean difference and mean deviation of Tukey lambda distribution.

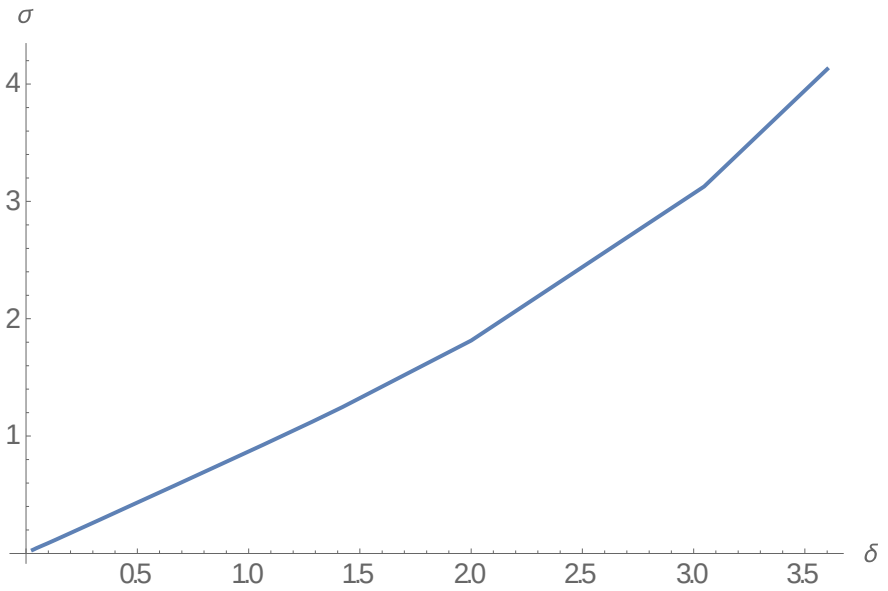

Figure 5. Numerical relationship between mean deviation and standard deviation of Tukey lambda distribution.

As it can be seen, the relationship between mean deviation and standard deviation of Tukey Lambda distribution increases with slow acceleration.

5. Conclusive Remarks

In this work, the formulas of mean difference and mean deviation of Tukey Lambda distribution have been obtained. It is an original contribution aimed at increasing the knowledge about this distribution model. These results allowed us to investigate the relationships among the three main variability indexes, standard deviation, mean deviation and mean difference, regarding Tukey lambda model.

Conflicts of Interest

The authors declare no conflicts of interest regarding the publication of this paper.

References

[1] Girone, G., Massari, A. and Manca, F. (2016) The Relation between the Mean Difference and the Standard Deviation in Continuous Distribution Models. *Quality and Quantity*, **51**, 481-507. https://doi.org/10.1007/s11135-016-0398-y

[2] D'Uggento, A.M., Girone, G. and Marin, C. (2016) The Relation between the Mean Difference and the Mean Deviation in 11 Continuous Distribution Models. *Quality and Quantity*, **51**, 595-615. https://doi.org/10.1007/s11135-016-0427-x

[3] Davydov, Y. and Greselin, F. (2019) Inferential Results for a New Measure of Inequality. *The Econometrics Journal*, **22**, 153-172. https://doi.org/10.1093/ectj/utz004

[4] Greselin, F. and Zitikis, R. (2018) From the Classical Gini Index of Income Inequality to a New Zenga-Type Relative Measure of Risk: A Modeller's Perspective. *Econometrics*, **6**, 1-20. https://doi.org/10.3390/econometrics6010004

[5] Girone, G. and Mazzitelli, D. (2007) La differenza media nei principali modelli distributivi continui. *Annali del Dipartimento di Scienze Statistiche "Carlo Cecchi"*, **VI**, 43-62.

[6] Girone, G., Massari, A., Campobasso, F., Manca, F., D'Uggento, A.M., Marin, C. and Nannavecchia, A. (2017) Rassegna sulla differenza media di distribuzioni teoriche continue. *Rivista di Economia e Commercio*, **V**, 13-28.

[7] Ramberg, J. and Schmeiser, B. (1972) An Approximate Method for Generating Symmetric Random Variables. *Communications of the ACM*, **15**, 987-990. https://doi.org/10.1145/355606.361888

[8] Ramberg, J., *et al.* (1979) A Probability Distribution and Its Uses in Fitting Data. *Technometrics*, **21**, 201-214. https://doi.org/10.1080/00401706.1979.10489750

[9] Tukey, J. (1960) The Practical Relationship between the Common Transformations of Percentages of Counts and Amounts. Technical Report 36, Statistical Techniques Research Group, Princeton University.

[10] Johnson, N.L. and Kotz, S. (1973) Extended and Multivariate Tukey Lambda Distributions. *Biometrika*, **60**, 655-661. https://doi.org/10.1093/biomet/60.3.655

[11] Sarabia, J.M. (1997) A Hierarchy of Lorenz Curves Based on the Generalized Tukey's Lambda Distribution. *Econometric Reviews*, **16**, 305-320. https://doi.org/10.1080/07474939708800389

[12] Johnson, N., Kotz, S. and Balakrishnan, N. (1994) Continuous Univariate Distributions. Vol. 1, Wiley, New York, 1994.

[13] Hastings, C., Mosteller, F., Tukey, J.W. and Winsor, C.P. (1947) Low Moments for Small Samples: A Comparative Study of Order Statistics. *Annals of Mathematical Statistics*, **18**, 413-426. https://doi.org/10.1214/aoms/1177730388

Attributions

Girone Section 1; Massari Section 3; Manca Section 4; D'Uggento Sections 2 and 5.

Scientific Research Publishing

Applied Mathematics, 2020, 11, 779-787
https://www.scirp.org/journal/am
ISSN Online: 2152-7393
ISSN Print: 2152-7385

The Adomian Decomposition Method for Solving Volterra-Fredholm Integral Equation Using Maple

Hunida M. Malaikah

Department of Mathematics, Faculty of Science, King Abdulaziz University, Jeddah, KSA
Email: hmalaikah@kau.edu.sa

How to cite this paper: Malaikah, H.M. (2020) The Adomian Decomposition Method for Solving Volterra-Fredholm Integral Equation Using Maple. *Applied Mathematics*, **11**, 779-787.
https://doi.org/10.4236/am.2020.118052

Received: July 19, 2020
Accepted: August 24, 2020
Published: August 27, 2020

Abstract

In this paper, Adomian decomposition method (ADM) is used to solve the Volterra-Fredholm integral equation. A number of examples have been presented to explain the numerical results, which is the comparison between the exact solution and the numerical solution, and it is found through the tables and the amount of error between the exact solution and the numerical solution, it is very small and almost non-existent and is also illustrated through the graph how the exact solution of completely applies to the numerical solution This proves the accuracy of the method, which is the Adomian decomposition method (ADM) for solving the Volterra Fredholm integral equation using Maple 18. And that this method is characterized by ease, speed and great accuracy in obtaining numerical results.

Keywords

Volterra-Fredholm Integral Equation, Adomian Decomposition Method, Maple18

1. Introduction

The current research intends to the Adomian decomposition method for solving Volterra-Fredholm integral equation using Maple18.

Integral equations are the basic sciences in our real life, and they explain physical, chemical, engineering, and medical phenomena, and more than that, they contribute greatly to reaching analytical and numerical solutions to these phenomena in various areas of our lives [1] [2]. There are several studies of Adomian decomposition metod, convergence and accuracy of Adomian's decomposition method for the solution of Lorenz equationsis studied in [3]. Solv-

ing Riccati differential equation using Adomian's decomposition method is given in [4]. An adaptation of Adomian decomposition for numeric-analytic integration of strongly nonlinear and chaotic oscillatorsis studied in [5]. The extended Adomian decomposition method for fourth order boundary value problems is given in [6]. The use of the Adomian decomposition method for solving multipoint boundary value problems is mentioned in [7]. [8] developed a new algorithm for evaluating Adomian polynomials. [9] studied an efficient algorithm for the multivariable Adomian polynomials. [10] found convenient analytic recurrence algorithms for the Adomian polynomials. A review of the Adomian decomposition method and its applications to fractional differential equations is given in [11]. [12] covers a bibliography of the theory and applications of the Adomian decomposition method. We find that solutions of nonlinear integral equations are more difficult to solve than linear integral equations and there are many analytical and numerical methods for solving linear and nonlinear integral equations mentioned in the references [13] [14] [15] [16]. We discuss the numerical solution of the integral Volterra equation of the second type using an implicit trapezoidal [17] [18]. The Adomian decomposition method of the Fredholm integral equation of the second kind using MATLAB and Maple is demonstrated in [19]. The Adomian decomposition method was applied to solve the Fredholm integral equation of the second kind [20]. Also, Modified analysis method for solving the Volterra integral equation of the second kind using Maple is discussed in [21].

In this article we have applied the Adomian decomposition method used by using the Maple algorithm by applying this algorithm to different examples, including finding the approximate solution and then comparing it to the exact solution and finding out the amount of error between the approximate solution and the exact solution.

The main objective of this work is to use the Adomian decomposition method in solving the Volterra-Fredholm integral equation of the second kind using Maple18.

The paper is arranged as follows: In Section 2, the Adomian decomposition method; in Section 3, numerical examples are also considered to show the ability of the proposed method, and the conclusion is drawn in Section 4.

2. The Adomian Decomposition Method

To clarify the basic idea of this method, we consider the following general non-linear differential equation:

$$u(x) = f(x) + \lambda_1 \int_a^x K_1(x,t)u(t)\mathrm{d}t + \lambda_2 \int_a^b K_2(x,t)u(t)\mathrm{d}t. \tag{1}$$

where L is assumed invertible and L^{-1} is an inverse operator.

The standard Adomian method defines the solution $u(x)$ by the series

$$u(x) = \sum_{n=0}^{\infty} u_n(x). \tag{2}$$

The modified decomposition method

$$u_0(x) = f(x) \tag{3}$$

$$u_1(x) = f(x) + L^{-1}\left(\lambda_1 \int_a^x K_1(x,t)u_0(t)\mathrm{d}t\right) + L^{-1}\left(\lambda_2 \int_a^b K_2(x,t)u_0(t)\mathrm{d}t\right), \quad (4)$$

$$u_{n+1}(x) = L^{-1}\left(\lambda_1 \int_a^x K_1(x,t)u_n(t)\mathrm{d}t\right) + L^{-1}\left(\lambda_2 \int_a^b K_2(x,t)u_n(t)\mathrm{d}t\right). \quad (5)$$

The use of a modified decomposition method not only reduces the calculations but avoids the use of the human polynomial arrangement of boundaries in such cases.

3. Numerical Examples

In this section, we solve some examples, and we can compare the numerical results with the exact solution.

Example 1. Consider the Volterra Fredholm integral equation

$$u(x) = x - \frac{1}{3}x^3 + \int_0^x tu(t)\mathrm{d}t + \int_{-1}^1 t^2 u(t)\mathrm{d}t, \quad (6)$$

the exact Solution $u(x) = x$.

Applying the Adomian decomposition method using Maple18 we find (Table 1 & Figure 1).

Example 2. Consider the Volterra Fredholm integral equation

$$u(x) = \sin(x) - \cos(x) - \int_0^x u(t)\mathrm{d}t + \int_0^{\frac{\pi}{2}} u(t)\mathrm{d}t \quad (7)$$

the exact Solution $u(x) = \sin(x)$.

Applying the Adomian Decomposition Method using Maple18 we find (Table 2 & Figure 2).

Example 3. Consider the Volterra Fredholm integral equation

$$u(x) = 3x + 4x^2 - x^3 - x^4 - 2 + \int_0^x tu(t)\mathrm{d}t + \int_{-1}^1 tu(t)\mathrm{d}t. \quad (8)$$

the exact Solution $u(x) = 3x + 4x^2$.

Table 1. Approximation solution and exact solution of Volterra Fredholm integral equations for example 1.

x	$u = x$	Exact1 $= x$	Error $= \lvert \text{Exact1} - u \rvert$
0.10000	0.1000000	0.1000000	0.0000000
0.20000	0.2000000	0.2000000	0.0000000
0.30000	0.3000000	0.3000000	0.0000000
0.40000	0.4000000	0.4000000	0.0000000
0.50000	0.5000000	0.5000000	0.0000000
0.60000	0.6000000	0.6000000	0.0000000
0.70000	0.7000000	0.7000000	0.0000000
0.80000	0.8000000	0.8000000	0.0000000
0.90000	0.9000000	0.9000000	0.0000000
1.00000	1.0000000	1.0000000	0.0000000

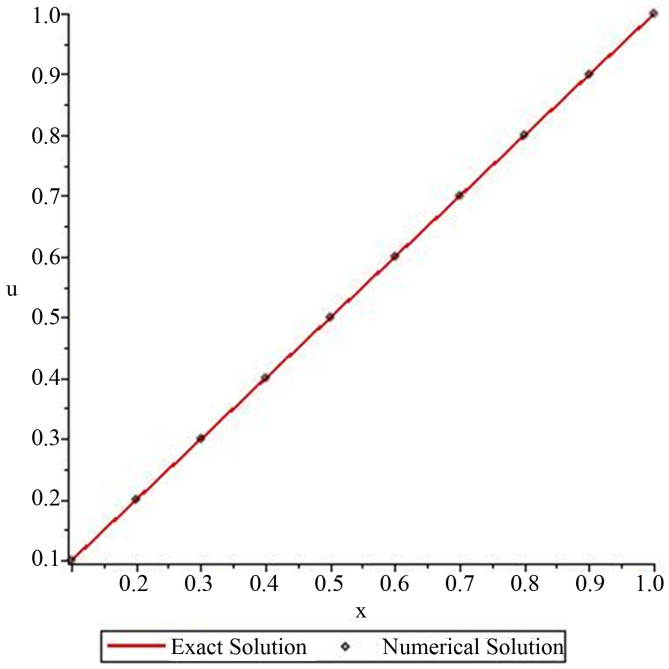

Figure 1. Plot of the solutions of Volterra Fredholm integral equation for example 1.

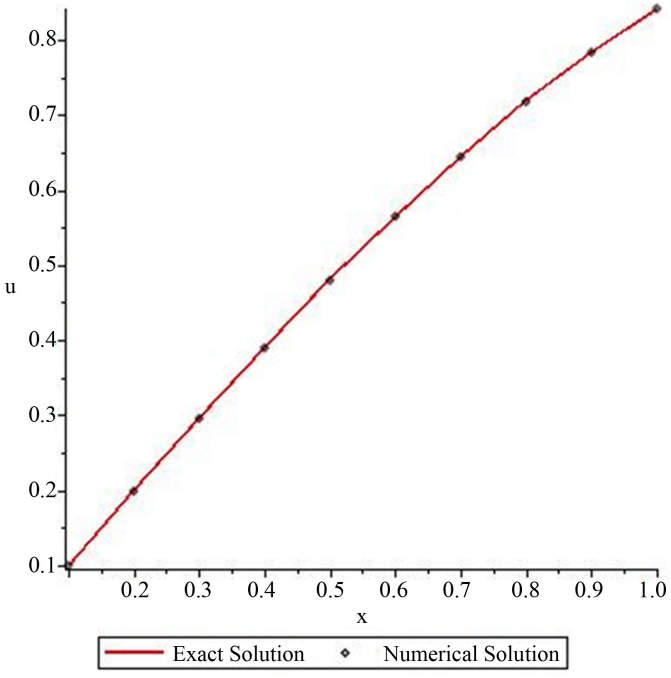

Figure 2. Plot of the solutions of Volterra Fredholm integral equation for example 2.

Table 2. Approximation solution and exact solution of Volterra Fredholm integral equations for example 2.

x	u	$\text{Exact2} = \sin(x)$	$\text{Error} = \lvert\text{Exact2} - u\rvert$
0.10000	0.0997464	0.0998334	0.0000870
0.20000	0.1986230	0.1986693	0.0000463

Continued

0.30000	0.2954967	0.2955202	0.0000235
0.40000	0.3894071	0.3894183	0.0000113
0.50000	0.4794205	0.4794255	0.0000050
0.60000	0.5646404	0.5646425	0.0000021
0.70000	0.6442169	0.6442177	0.0000008
0.80000	0.7173558	0.7173561	0.0000003
0.90000	0.7833268	0.7833269	0.0000001
1.00000	0.8414710	0.8414710	0.0000000

Table 3. Approximation solution and exact solution of Volterra Fredholm integral equations for example 3.

x	u	$\text{Exact3} = 3x + 4x^2$	$\text{Error} = \lvert\text{Exact3} - u\rvert$
0.10000	0.3400000	0.3399998	0.0000002
0.20000	0.7600000	0.7599998	0.0000002
0.30000	1.2600000	1.2599996	0.0000004
0.40000	1.8400000	1.8399994	0.0000006
0.50000	2.5000000	2.4999988	0.0000012
0.60000	3.2400000	3.2399976	0.0000024
0.70000	4.0600000	4.0599948	0.0000052
0.80000	4.9600000	4.9599883	0.0000117
0.90000	5.9400000	5.9399731	0.0000269
1.00000	7.0000000	6.9999375	0.0000625

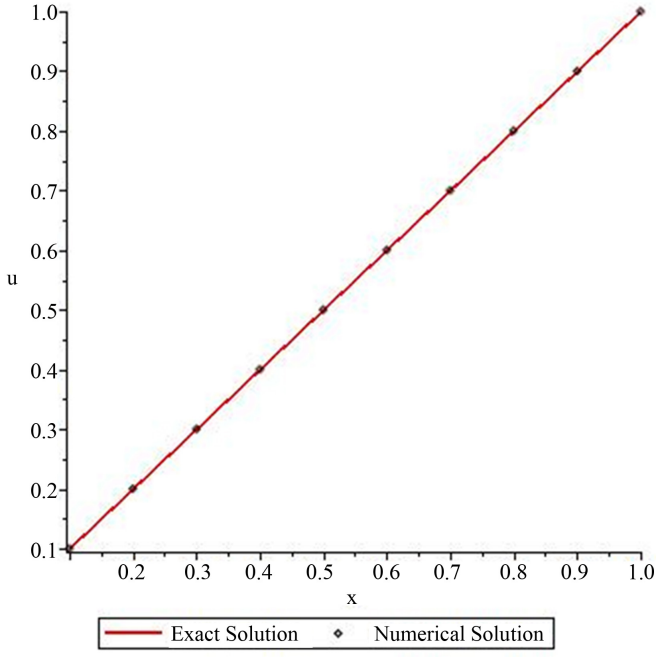

Figure 3. Plot of the solutions of Volterra Fredholm integral equation for example 3.

Applying the Adomian Decomposition Method using Maple18 we find (Table 3 & Figure 3).

Example 4. Consider the Volterra Fredholm integral equation

$$u(x) = -2 - 2x + 2e^{x} + \int_0^x (x-t)u(t)\,dt + \int_0^1 xu(t)\,dt \tag{9}$$

the exact Solution $u(x) = xe^{x}$.

Applying the Adomian Decomposition Method using Maple we find (Table 4 & Figure 4).

Example 5. Consider the Volterra Fredholm integral equation

$$u(x) = x^3 - \frac{9}{20}x^5 - \frac{1}{4}x + \frac{1}{5} + \int_0^x (x+t)u(t)\,dt + \int_0^1 (x-t)u(t)\,dt \tag{10}$$

the exact Solution $u(x) = x^3$.

Table 4. Approximation solution and exact solution of Volterra Fredholm integral equations for example 4.

x	u	$\text{Exact4} = xe^{x}$	$\text{Error} = \lvert\text{Exact4} - u\rvert$
0.10000	0.1105171	0.1093187	0.0011984
0.20000	0.2442806	0.2418630	0.0024176
0.30000	0.4049576	0.4012789	0.0036788
0.40000	0.5967299	0.5917260	0.0050039
0.50000	0.8243606	0.8179448	0.0064158
0.60000	1.0932713	1.0853320	0.0079393
0.70000	1.4096269	1.4000262	0.0096006
0.80000	1.7804327	1.7690040	0.0114287
0.90000	2.2136428	2.2001875	0.0134553
1.00000	2.7182818	2.7025662	0.0157157

Table 5. Approximation solution and exact solution of Volterra Fredholm integral equations for example 5.

x	u	$\text{Exact5} = x^3$	$\text{Error} = \lvert\text{Exact5} - u\rvert$
0.10000	0.0010000	0.0007782	0.0002218
0.20000	0.0080000	0.0083499	0.0003499
0.30000	0.0270000	0.0280883	0.0010883
0.40000	0.0640000	0.0659947	0.0019947
0.50000	0.1250000	0.1280596	0.0030596
0.60000	0.2160000	0.2202426	0.0042426
0.70000	0.3430000	0.3484413	0.0054413
0.80000	0.5120000	0.5184507	0.0064507
0.90000	0.7290000	0.7359143	0.0069143
1.00000	1.0000000	1.0062804	0.0062804

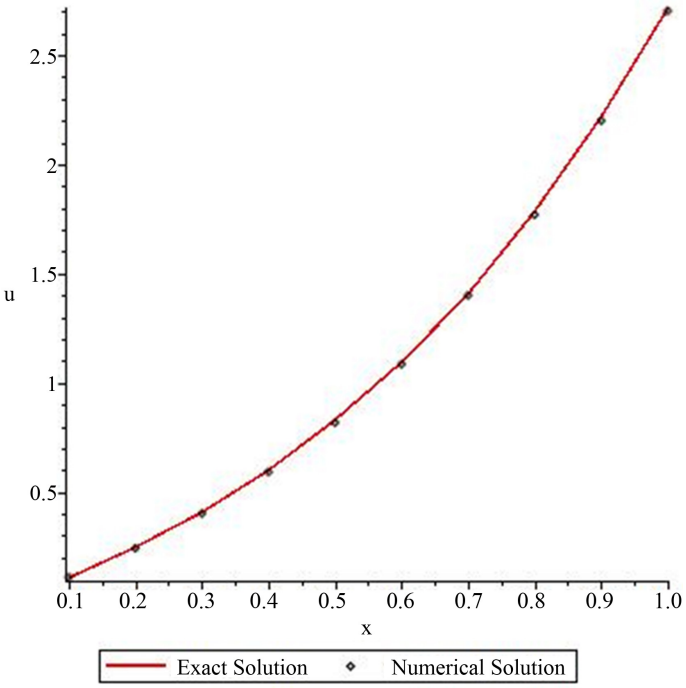

Figure 4. Plot of the solutions of Volterra Fredholm integral equation for example 4.

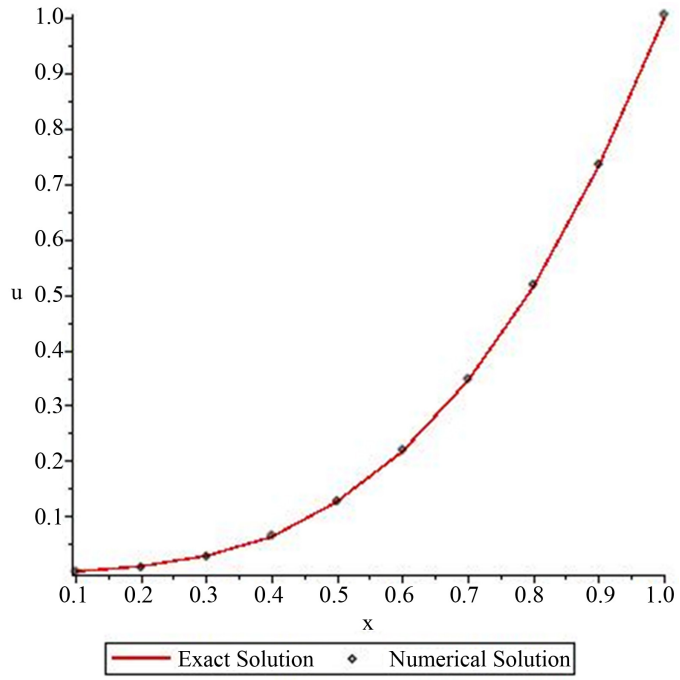

Figure 5. Plot of the solutions of Volterra Fredholm integral equation for example 5.

Applying the Adomian Decomposition Method using Maple18 we find (Table 5 & Figure 5).

4. Conclusion

In this paper, the Adomian decomposition method was applied to solve the

integral Volterra Fredholm equation using program Maple18. The results are obtained in the tables and drawn in the figures. Tables 1-5 show the correct solution and the numerical solution. Tables 1-5 represent the exact and numerical results of the examples in this article. Figures 1-5 readily show the comparison of exact solution and ap-proximate solution. Comparing the numerical results, we find that the numerical solution is largely applied to the exact solution, which proves the efficiency of the method used and the ability to obtain the numerical solution corresponding to the exact solution easily and conveniently with a program Maple 18. Moreover, the high accuracy of the results is obtained.

Acknowledgements

This project was funded by the Deanship of Scientific Research (DSR), King Abdulaziz University. The author, therefore, acknowledges with thanks for DSR technical and fnancial support.

Conflicts of Interest

The author declares no conflicts of interest regarding the publication of this paper.

References

[1] Abdul-Majid, W. (1999) A Reliable Modification of Adomain Decomposition Method. *Applied Mathematics and Computation*, **102**, 77-86. https://doi.org/10.1016/S0096-3003(98)10024-3

[2] Wazwaz, A.-M. and El-Sayed, S.M. (2001) A New Modification of the Adomain Decomposition Method for Linear and Nonlinear Operators. *Applied Mathematics and Computation*, **122**, 393-405. https://doi.org/10.1016/S0096-3003(00)00060-6

[3] Vadasz, P. and Olek, S. (2000) Convergence and Accuracy of Adomian's Decomposition Method for the Solution of Lorenz Equations. *International Journal of Heat and Mass Transfer*, **43**, 1715-1734. https://doi.org/10.1016/S0017-9310(99)00260-4

[4] El-Tawil, M.A., Bahnasawi, A.A. and Abdel-Naby, A. (2004) Solving Riccati Differential Equation Using Adomian's Decomposition Method. *Applied Mathematics and Computation*, **157**, 503-514. https://doi.org/10.1016/j.amc.2003.08.049

[5] Ghosh, S., Roy, A. and Roy, D. (2007) An Adaptation of Adomian Decomposition for Numeric-Analytic Integration of Strongly Nonlinear and Chaotic Oscillators. *Computer Methods in Applied Mechanics and Engineering*, **196**, 1133-1153. https://doi.org/10.1016/j.cma.2006.08.010

[6] Ebadi, G. and Rashedi, S. (2010) The Extended Adomian Decomposition Method for Fourth Order Boundary Value Problems. *Acta Universitatis Apulensis*, **22**, 65-78.

[7] Tatari, M. and Dehghan, M. (2006) The Use of the Adomian Decomposition Method for Solving Multipoint Boundary Value Problems. *Physica Scripta*, **73**, 672-676. https://doi.org/10.1088/0031-8949/73/6/023

[8] Azreg-Ainou, M. (2009) A Developed New Algorithm for Evaluating Adomian Polynomials. *CMES Computer Modeling in Engineering and Sciences*, **42**, 1-18.

[9] Duan, J.S. (2010) An Efficient Algorithm for the Multivariable Adomian Polynomials. *Applied Mathematics and Computation*, **217**, 2456-2467.

https://doi.org/10.1016/j.amc.2010.07.046

[10] Duan, J.S. (2011) Convenient Analytic Recurrence Algorithms for the Adomian Polynomials. *Applied Mathematics and Computation*, **217**, 6337-6348. https://doi.org/10.1016/j.amc.2011.01.007

[11] Duan, J.S., Rach, R., Baleanu, D. and Wazwaz, A.M. (2012) A Review of the Adomian Decomposition Method and Its Applications to Fractional Differential Equations. *Communications in Fractional Calculus*, **3**, 73-99.

[12] Rach, R. (2012) A Bibliography of the Theory and Applications of the Adomian Decomposition Method, 1961-2011. *Kybernetes*, **41**, 1087-1148. https://doi.org/10.1108/k.2012.06741gaa.007

[13] Abdul-Majid, W. (2011) Linear and Nonlinear Integral Equations. Higher Education Press, Beijing.

[14] Peter, L. (1985) Analytical and Numerical Methods for Volterra Equations. Studies in Applied Mathematics 7, SIAM, Philadelphia.

[15] Doddrell, D.M., Forbes, L.K. and Crozier, S. (1997) Calculating Current Densities and Fields Produced by Shielded Magnetic Resonance Imaging Probes. *SIAM Journal on Applied Mathematics*, **57**, 401-425. https://doi.org/10.1137/S0036139995283110

[16] Dalal, A.M., Amani, Z.B. and Badreeh, M.G. (2014) Numerical Solution of Volterra Integral Equation of Second Kind Using Implicit Trapezoidal. *Journal of Advances in Mathematics*, **8**, 1540-1553.

[17] Dalal, A.M. (2014) Adomian Decomposition Method of Fredholm Integral Equation of the Second Kind Using Maple. *Journal of Advances in Mathematics*, **9**, 1868-1875.

[18] Dalal, A.M. (2014) Application of Adomian Decomposition Method for Solving of Fredholm Integral Equation of the Second Kind. *European Journal of Science and Engineering*, **9**, 1-9.

[19] Dalal, A.M. (2016) Adomian Decomposition Method for Solving of Fredholm Integral Equation of the Second Kind Using Matlab. *International Journal of GEOMATE*, **11**, 2830-2833.

[20] Dalal, A.M. and Honida, M.M. (2018) Numerical Solution of System of Three Nonlinear Volterra Integral Equation Using Implicit Trapezoidal. *Journal of Mathematics Research*, **10**, 44. https://doi.org/10.5539/jmr.v10n1p44

[21] Dalal, A.M. (2019) The Modified Decomposition Method for Solving Volterra Integral Equation of the Second Kind Using Maple. *International Journal of GEOMATE*, **17**, 23-28. https://doi.org/10.21660/2019.62.4590

Scientific Research Publishing

Applied Mathematics, 2020, 11, 788-824
https://www.scirp.org/journal/am
ISSN Online: 2152-7393
ISSN Print: 2152-7385

Effect of Depth-Dependent Nociceptor Density on the Heat-Induced Withdrawal Reflex

Hongyun Wang[1], Wesley A. Burgei[2], Hong Zhou[3*]

[1]Department of Applied Mathematics, University of California, Santa Cruz, CA, USA
[2]U.S. Department of Defense, Joint Intermediate Force Capabilities Office, Quantico, VA, USA
[3]Department of Applied Mathematics, Naval Postgraduate School, Monterey, CA, USA
Email: *hzhou@nps.edu

How to cite this paper: Wang, H.Y., Burgei, W.A. and Zhou, H. (2020) Effect of Depth-Dependent Nociceptor Density on the Heat-Induced Withdrawal Reflex. *Applied Mathematics*, **11**, 788-824.
https://doi.org/10.4236/am.2020.118053

Received: June 17, 2020
Accepted: August 28, 2020
Published: August 31, 2020

Abstract

Previously we introduced a concise dose-response model for the heat-induced withdrawal reflex caused by millimeter wave radiation. The model predicts the occurrence of withdrawal reflex from the given spatial temperature profile. It was formulated on the assumption that the density of nociceptors in skin is uniform, independent of the depth. The model has only two parameters: the activation temperature of heat-sensitive nociceptors and the critical threshold on the activated volume for triggering withdrawal reflex. In this study, we consider the case of depth-dependent nociceptor density in skin. We use a general parametric form with a scaling parameter in the depth direction to represent the nociceptor density. We analyze system behaviors for four density types of this form. Based on the theoretical results, we develop a methodology for 1) identifying from test data the density form of nociceptors distribution, 2) finding from test data the scaling parameter in the density form, and 3) determining from test data the activation temperature of nociceptors.

Keywords

High-Energy Millimeter Wave Radiation, Heat-Induced Pain, Depth-Dependent Nociceptor Density In Skin

1. Introduction

The rapid development of applications such as wireless communications, security scanning, tissue diagnosis, and non-lethal weapons for crowd control or perimeter security has considerably increased human exposure to high-frequency millimeter waves (MMW) ranging from 30 to 300 gigahertz (GHz). For the purpose of biological risk assessment, it is vital to understand the effects of this irradia-

tion on humans.

Many experiments have shown that exposure to MMW at sufficiently high intensities primarily produces fast heating near the surface of the skin [1]-[7]. The transmitted MMW power is absorbed in the skin to a depth of less than 0.5 mm at 100 GHz [8] and is attenuated exponentially as a function of skin depth. The skin generally consists of three different layers, namely epidermis, dermis, and hypodermis [9]. These layers have different thickness depending on the location of the skin. In particular, the epidermis is the outermost layer of skin containing both living and dead cells with thickness 0.075 - 0.15 mm. The dermis lies beneath the epidermis and is much thicker (1 - 4 mm). There are blood vessels and nerves in the dermis. The third layer is the hypodermis, which is composed of mainly subcutaneous fat. The hypodermis is about 1.1 - 5.6 mm in thickness. Studies performed at 60 GHz demonstrated that while the maximum value of the power density and specific absorption rate occurs at the epidermis, up to 60% of the incident power reaches the dermis, and only 10% gets to the hypodermis [10] [11]. Absorption of the MMW energy causes the local temperature of the skin to rise and can activate nociceptors [12] and consequently lead to a sensation of pain [13] [14].

Nociceptors are sensory nerve cells that respond to painful stimuli by sending out signals to the spinal cord via a chain of nerve fibers. When the collective signal becomes strong enough, the withdrawal reflex is triggered and the subject moves away from the exposure [15] [16]. Previously, we formulated a dose-response model for the heat-induced withdrawal reflex from MMV radiation [17]. The concise model predicts the occurrence of withdrawal reflex from a given spatial temperature profile of the skin. A prominent feature of the model is that it contains only two parameters. One key assumption in the concise model is that the nociceptor density in skin does not vary with the depth. In this paper we extend our earlier study by relaxing this assumption. Our goal is to determine the effect of depth-dependent nociceptor density on the heat-induced withdrawal reflex.

2. Mathematical Formulation in the Case of Depth Dependent Nociceptor Density

In this section, we study the mathematical formulation when the nociceptor density is a function of depth in the skin. We start by introducing proper mathematical notations:

- y: the depth coordinate (the skin surface is $y = 0$).
- $\boldsymbol{r}$: 2-D coordinates on the skin surface; $(\boldsymbol{r}, y)$ is the 3-D coordinates.
- $T(\boldsymbol{r}, y)$: 3-D spatial temperature profile of the skin.
- T_{act} : activation temperature of nociceptors; given $T(\boldsymbol{r}, y)$, the activation status of a nociceptor at $(\boldsymbol{r}, y)$ is governed by the indicator function

$$I_{(T \geq T_{\text{act}})}(\boldsymbol{r}, y) \equiv \begin{cases} 1, & \text{if } T(\boldsymbol{r}, y) \geq T_{\text{act}} \\ 0, & \text{if } T(\boldsymbol{r}, y) < T_{\text{act}} \end{cases}$$

- $\rho(y)$: nociceptor density at depth y (number per volume).
- X_{act}: total number of activated nociceptors in the skin,

$$X_{\text{act}} = \int \rho(y) I_{(T \geq T_{\text{act}})}(\boldsymbol{r}, y) \mathrm{d}\boldsymbol{r}\mathrm{d}y$$

- ρ_0: characteristic reference nociceptor density.

When the nociceptor density is uniform, $\rho(y) = \rho_0$, the activated volume is proportional to the number of activated nociceptors. In this case, we adopted the activated volume as the single metric predictor variable (the input dose) for predicting withdrawal reflex [17].

Input dose in the case of uniform density:

$$z \equiv \int I_{(T \geq T_{\text{act}})}(\boldsymbol{r}, y) \mathrm{d}\boldsymbol{r}\mathrm{d}y \tag{1}$$

The advantages of this input dose are 1) it makes the dose quantity independent of the nociceptor density ρ_0, and 2) it shifts the effect of ρ_0 into the dose threshold z_c. In the dose response model, withdrawal reflex occurs when $z \geq z_c$ where the effects of ρ_0 and all other factors are reflected the single metric quantity z_c.

In the case of non-uniform nociceptor density, the activated volume is no longer proportional to the number of activated nociceptors, and thus is no longer a valid candidate for the input dose. We like to define the dose such that it contains (1) as a special case. For that purpose, we define the equivalent activated volume z_{equ} based on reference density ρ_0, and use z_{equ} as the input dose.

Input dose in the case of non-uniform density:

$$z_{\text{equ}} \equiv \frac{1}{\rho_0} X_{\text{act}} = \int \frac{\rho(y)}{\rho_0} I_{(T \geq T_{\text{act}})}(\boldsymbol{r}, y) \mathrm{d}\boldsymbol{r}\mathrm{d}y \tag{2}$$

The dose response relation has the same form as in the case of uniform density.

$$\text{Outcome}(z_{\text{equ}}) = \begin{cases} 1\ (\text{withdrawal reflex}), & \text{if } z_{\text{equ}} \geq z_c \\ 0\ (\text{no withdrawal reflex}), & \text{if } z_{\text{equ}} < z_c \end{cases}$$

In this study, we consider the hypothetical situation where the time of withdrawal reflex and the spatial temperature profile at reflex are measurable in experiments. With these two measurable entities, we explore the behaviors of several parameterized nociceptor density types. The objectives of the study are 1) to distinguish these candidate density types from each other based on the measurable entities, and 2) to infer the parameter values.

The calculation of z_{equ} defined in (2) requires only the relative density $\rho(y)/\rho_0$. The effect of ρ_0 is contained in the dose threshold z_c. When $\rho(y)/\rho_0$ is given, the dose response model has only two unknown parameters: T_{act} and z_c. In a test, the measured temperature profile $T(\boldsymbol{r}, y)$ at reflex provides a constraint on (T_{act}, z_c). Mathematically, we construct constraint function $z_c(T_{\text{act}})$ as follows. For any value of T_{act}, by definition, the corresponding value of z_c is the value of z_{equ} calculated based on T_{act} and $T(\boldsymbol{r}, y)$.

$$z_c\left(T_{\text{act}}\right)=\int\frac{\rho(y)}{\rho_0}I_{(T\geq T_{\text{act}})}(\boldsymbol{r},y)\,\mathrm{d}\boldsymbol{r}\mathrm{d}y \tag{3}$$

when $\rho(y)/\rho_0$ is given, function $z_c\left(T_{\text{act}}\right)$ is completely determined by the measured $T(\boldsymbol{r},y)$. Constraint functions $z_c\left(T_{\text{act}}\right)$ based on $T(\boldsymbol{r},y)$ measured at different test conditions are potentially distinct from each other. All these constraint functions have one common intersection, which gives the true values of $\left(T_{\text{act}},z_c\right)$.

When the true relative density $\rho(y)/\rho_0$ is unknown, we work with a trial relative density $r^{(\text{try})}(y)$. We use $r^{(\text{try})}(y)$ to replace $\rho(y)/\rho_0$ in (3) and construct trial constraint function $z_c\left(T_{\text{act}}\right)$ from the test data. Note that the true values of $\left(T_{\text{act}},z_c\right)$ satisfy only the true constraint function calculated using the true $\rho(y)/\rho_0$. When $r^{(\text{try})}(y)$ deviates from the true $\rho(y)/\rho_0$, the true values of $\left(T_{\text{act}},z_c\right)$ are not on the trial constraint curve calculated using $r^{(\text{try})}(y)$. Consequently, for a pair of trial constraint functions calculated using $r^{(\text{try})}(y)$ (based on measured $T(\boldsymbol{r},y)$ of two distinct test conditions), their intersection is not at the true values of $\left(T_{\text{act}},z_c\right)$, and the intersection varies with the test conditions of the pair. The test-condition-dependence of the intersection serves as an indication that the trial density $r^{(\text{try})}(y)$ is incorrect. The specific behavior of test-condition-dependence of the intersection provides a venue for us to tune $r^{(\text{try})}(y)$ toward the true $\rho(y)/\rho_0$.

We examine several types of parameterized density. We study the test-condition dependence of 1) the reflex time and 2) the intersection of a pair of trial constraint functions. The goal is to identify system behaviors that a) help us distinguish these density types from each other and b) guide us to tune the trial parameter toward its true value.

We carry out the analysis in the idealized situation where

- the electromagnetic heating is uniform over the beam cross-section (with area A) and it decays exponentially with depth y;
- the initial temperature is uniform everywhere;
- the heat conduction is included only in the depth direction.

This is the same as case B in our previous study [17]. At any given time, the temperature inside the beam cross-section is a function of depth y only and it decreases with y. The time evolution of temperature distribution $T(y,t)$ is governed by

$$\begin{cases}\rho_{\text{m}}C_p\dfrac{\partial T(y,t)}{\partial t}=K\dfrac{\partial^2T(y,t)}{\partial y^2}+P_{\text{dep}}\mu\mathrm{e}^{-\mu y}\\ \left.\dfrac{\partial T(y,t)}{\partial y}\right|_{y=0}=0,\quad T(y,0)=T_0\end{cases}$$

where

- ρ_{m} is the mass density of skin,
- C_p is the specific heat capacity of the skin,
- K is the thermal conductivity of the skin,

- μ is the absorption coefficient of the skin,
- P_{dep} is the beam power density deposited on (absorbed into) the skin, and
- T_0 is the initial temperature of the skin.

In this idealized situation, the region of activated nociceptors ($T(y) \geq T_{\text{act}}$) is a cylinder with depth y_{act} governed by $T(y_{\text{act}}) = T_{\text{act}}$. By definition, T_{act}, $y_{\text{act}}\big|_{(\text{reflex})}$ and the reflex time t_{ref} are constrained by the temperature distribution, which we assume is measurable.

$$T_{\text{act}} = T\left(y_{\text{act}}\big|_{(\text{reflex})}, t_{\text{ref}}\right) \tag{4}$$

We consider a general 1-parameter form for the relative density of nociceptors

$$\frac{\rho(y)}{\rho_0} = f(\beta y)$$

where $f(s)$ can be any positive function. The activated depth y_{act} and the dose z_{equ} both vary with the activation temperature T_{act}, and are related by Equation (2) as

$$z_{\text{equ}} = A\int_0^{y_{\text{act}}} f(\beta y)\,\mathrm{d}y = \frac{A}{\beta}F(\beta y_{\text{act}}) \tag{5}$$

$$y_{\text{act}} = \frac{1}{\beta}F^{-1}\left(\frac{\beta z_{\text{equ}}}{A}\right) \tag{6}$$

where A is the beam spot area, $F(s) \equiv \int_0^s f(z)\,\mathrm{d}z$, and $F^{-1}(u)$ is the inverse function of $F(s)$. Since $f(s)$ is positive, function $F(s)$ is monotonically increasing and the inverse function $F^{-1}(u)$ is well-defined over the range of $F(s)$. By definition, functions $F(s)$ and $F^{-1}(u)$ satisfy $F(0) = 0$ and $F^{-1}(0) = 0$. Recall that the dose threshold is defined as $z_c \equiv z_{\text{equ}}\big|_{(\text{reflex})}$. Equation (6) gives

$$y_{\text{act}}\big|_{(\text{reflex})} = \frac{1}{\beta}F^{-1}\left(\frac{\beta z_c}{A}\right) \tag{7}$$

Equation (4) in combination with (7) provides a constraint on T_{act}, z_c, β and t_{ref}, which can be used for different purposes, depending on which parameters are known. When t_{ref} and $T(y,t)$ are measured, (4) gives us a constraint on z_c, T_{act} and β. On the other hand, when z_c, T_{act} and β are given, (4) can be viewed as a governing equation for t_{ref}. This is useful, for example, for examining the behavior of t_{ref} vs. A.

In the analysis of subsequent sections, we need the expansions of $f(s)$ and $F(s)$, $F^{-1}(u)$ and their derivatives. We now derive these expansions. We first write out the Taylor expansion of $f(s)$ around $s = 0$.

$$f(s) = a_0 + a_1 s + a_2\frac{s^2}{2!} + \cdots \quad \text{where } a_k = f^{(k)}(0)$$

$$F(s) \equiv \int_0^s f(z)\,\mathrm{d}z = a_0 s + a_1\frac{s^2}{2!} + a_2\frac{s^3}{3!} + \cdots$$

The expansion of $F^{-1}(u)$ is derived from that of $F(s)$ using an iterative

method. It depends on which term in the expansion of $F(s)$ is the leading non-zero term. Let $u \equiv F(s)$. The inverse function $F^{-1}(u)$ maps u back to s. We discuss two cases.

- **Case 1**: $f(0) \neq 0$. Function $u = F(s)$ has the expansion

$$u = a_0 s + a_1 \frac{s^2}{2!} + \cdots \quad \text{where } a_k = f^{(k)}(0)$$

Based on that, we built an iteration formula:

$$s_{j+1} = \frac{1}{a_0}\left(u - a_1 \frac{1}{2!} s_j^2\right), \quad s_0 = 0$$

The iteration gives us expansions of $F^{-1}(u)$ and $\left(F^{-1}\right)'(u)$

$$F^{-1}(u) = \frac{1}{a_0} u - \frac{a_1}{2a_0^3} u^2 + \cdots \quad \text{for } f(0) \neq 0 \tag{8}$$

$$\left(F^{-1}\right)'(u) = \frac{1}{a_0} - \frac{a_1}{a_0^3} u + \cdots \quad \text{for } f(0) \neq 0 \tag{9}$$

- **Case 2**: $f(0) = 0$ but $f'(0) \neq 0$. Function $u = F(s)$ has the expansion

$$u = a_1 \frac{s^2}{2!} + a_2 \frac{s^3}{3!} + \cdots \quad \text{where } a_k = f^{(k)}(0)$$

Based on that, we construct an iteration formula for s^2:

$$s_{j+1}^2 = \frac{2}{a_1}\left(u - a_2 \frac{1}{3!}\left(s_j^2\right)^{3/2}\right), \quad s_0^2 = 0$$

which yields the expansion of s^2 in terms of u

$$s^2 = \frac{2}{a_1} u \left(1 - \frac{a_2}{6} \cdot \frac{2}{a_1}\left(\frac{2}{a_1} u\right)^{1/2} + \cdots\right)$$

Taking square roots of both sides, we obtain

$$F^{-1}(u) = \frac{\sqrt{2}}{\sqrt{a_1}} u^{1/2} - \frac{a_2}{3a_1^2} u + \cdots \quad \text{for } f(0) = 0 \text{ but } f'(0) \neq 0 \tag{10}$$

$$\left(F^{-1}\right)'(u) = \frac{1}{\sqrt{2a_1}} u^{-1/2} - \frac{a_2}{3a_1^2} + \cdots \quad \text{for } f(0) = 0 \text{ but } f'(0) \neq 0 \tag{11}$$

with the mathematical results above, we study the behavior of t_{ref} vs A.

3. Analysis of Reflex Time vs. Beam Spot Area

When T_{act}, z_c and β are given, (4) with (7) governs t_{ref} vs A. In our previous study [17], we scaled and shifted the physical temperature distribution to the normalized non-dimensional temperature $H(y_{\text{nd}}, t_{\text{nd}})$.

$$\frac{\left(T(y,t) - T_0\right) K \mu}{P_{\text{dep}}} = H\left(y_{\text{nd}}, t_{\text{nd}}\right) \tag{12}$$

where the non-dimensional depth y_{nd} and the non-dimensional time t_{nd} are defined as

$$y_{\mathrm{nd}} \equiv \mu y, \quad t_{\mathrm{nd}} \equiv t\frac{K\mu^2}{\rho_{\mathrm{m}}C_p}$$

The normalized temperature $H\left(y_{\mathrm{nd}}, t_{\mathrm{nd}}\right)$ has the expression

$$H\left(y,t\right) \equiv \int_0^t G\left(y,s\right)\mathrm{d}s$$

$$G\left(y,t\right) \equiv \frac{1}{2}\mathrm{erfc}\left(\frac{2t-y}{\sqrt{4t}}\right)\mathrm{e}^{t-y} + \frac{1}{2}\mathrm{erfc}\left(\frac{2t+y}{\sqrt{4t}}\right)\mathrm{e}^{t+y} \tag{13}$$

It is important to notice that the normalized temperature $H\left(y,t\right)$ is parameter-free. The non-dimensional version of (4) with (7) has the form

$$\frac{\left(T_{\mathrm{act}} - T_0\right)K\mu}{P_{\mathrm{dep}}} = H\left(y_{\mathrm{act,nd}}, t_{\mathrm{ref,nd}}\right) \tag{14}$$

$$y_{\mathrm{act,nd}} \equiv \frac{\mu}{\beta}F^{-1}\left(\frac{\beta}{\mu A_{\mathrm{nd}}}\right), \quad A_{\mathrm{nd}} \equiv \frac{A}{\mu z_c}, \quad t_{\mathrm{ref,nd}} \equiv t_{\mathrm{ref}}\frac{K\mu^2}{\rho_{\mathrm{m}}C_p}$$

In the above, $A_{\mathrm{nd}} \equiv \dfrac{A}{\mu z_c}$ is the non-dimensional beam spot area. In the limit of $A \to \infty$, we have $y_{\mathrm{act,nd}} \to 0$ and the equation for $t_{\mathrm{ref,nd}}$ becomes

$$\frac{\left(T_{\mathrm{act}} - T_0\right)K\mu}{P_{\mathrm{dep}}} = h\left(t_{\mathrm{ref,nd}}\big|_{A\to\infty}\right)$$

where $h\left(t_{\mathrm{nd}}\right) \equiv H\left(0, t_{\mathrm{nd}}\right)$. Let $t_0 \equiv h^{-1}\left(\dfrac{\left(T_{\mathrm{act}} - T_0\right)K\mu}{P_{\mathrm{dep}}}\right)$. We have $t_{\mathrm{ref,nd}}\big|_{A\to\infty} = t_0$.

We examine the asymptotic behavior of this convergence. We seek an expansion of the form

$$t_{\mathrm{ref,nd}}\left(A_{\mathrm{nd}}\right) = t_0\left[1 + c_A\left(\frac{1}{A_{\mathrm{nd}}}\right)^{\alpha} + \cdots\right] \tag{15}$$

Expanding $H\left(y_{\mathrm{nd}}, t_{\mathrm{nd}}\right)$ around $\left(0, t_0\right)$ and substituting (15), we get

$$0 = \frac{\partial H\left(0,t_0\right)}{\partial t}t_0 c_A\left(\frac{1}{A_{\mathrm{nd}}}\right)^{\alpha} + \frac{1}{2}\frac{\partial^2 H\left(0,t_0\right)}{\partial y^2}\left(\frac{\mu}{\beta}F^{-1}\left(\frac{\beta}{\mu A_{\mathrm{nd}}}\right)\right)^2 \tag{16}$$

Exponent α and coefficient c_A are determined using the leading term expansion of $F^{-1}\left(u\right)$. The result depends on whether the nociceptor density at the skin surface is zero.

- **Case 1**: $f\left(0\right) \neq 0$.

  The expansion of $F^{-1}\left(u\right)$ given in (8). Substituting it into (16), we have

$$\alpha = 2, \quad c_A = \frac{1}{2t_0\left(f\left(0\right)\right)^2}\cdot\frac{1-\mathrm{erfc}\left(\sqrt{t_0}\right)\mathrm{e}^{t_0}}{\mathrm{erfc}\left(\sqrt{t_0}\right)\mathrm{e}^{t_0}} \tag{17}$$

Here we have used $\dfrac{\partial H\left(0,t_0\right)}{\partial t} = \mathrm{erfc}\left(\sqrt{t_0}\right)\mathrm{e}^{t_0}$ and $\dfrac{\partial^2 H\left(0,t_0\right)}{\partial y^2} = \mathrm{erfc}\left(\sqrt{t_0}\right)\mathrm{e}^{t_0} - 1$ derived in our previous study.

- **Case 2:** $f(0)=0$ but $f'(0)\neq 0$

The expansion of $F^{-1}(u)$ given in (10). Substituting it into (16), we arrive at

$$\alpha=1,\quad c_A=\frac{\mu}{t_0 f'(0)\beta}\cdot\frac{1-\operatorname{erfc}\left(\sqrt{t_0}\right)\mathrm{e}^{t_0}}{\operatorname{erfc}\left(\sqrt{t_0}\right)\mathrm{e}^{t_0}} \tag{18}$$

Returning to the physical quantities before the non-dimensionalization, the reflex time vs beam spot area is given by

$$t_{\mathrm{ref}}(A)=\frac{t_0\rho_{\mathrm{m}}C_p}{K\mu^2}\left[1+c_A\left(\frac{\mu z_c}{A}\right)^{\alpha}+\cdots\right],\quad t_0=h^{-1}\left(\frac{(T_{\mathrm{act}}-T_0)K\mu}{P_{\mathrm{dep}}}\right) \tag{19}$$

4. Analysis of Constraint Functions on (T_{act}, z_c)

When t_{ref} and $T(y,t_{\mathrm{ref}})$ are measured, (4) with (7) serves as a constraint on T_{act}, z_c and β with beam spot area A as a parameter describing the test condition. We denote the constraint function as $T_{\mathrm{act}}(z_c;\beta,A)$ and use (4) to write it as

$$T_{\mathrm{act}}(z_c;\beta,A)=\Phi\left(\frac{1}{\beta}F^{-1}\left(\frac{\beta z_c}{A}\right);\frac{1}{A}\right) \tag{20}$$

where $\Phi(y;v)T\left(y,t_{\mathrm{ref}}(1/v)\right)$ is the temperature profile at reflex with beam spot area $A=1/v$. We represent the effect of A via variable $v=1/A$ since t_{ref} is a smooth function of $v=1/A$ as $A\to\infty$. To facilitate the discussion, we introduce two sets of mathematical notations. These two sets of notations are used to distinguish a quantity's true value from its role as a variable in a function.

- β^*: true value of coefficient β.
- β: a trial value of coefficient β.
- $(T_{\mathrm{act}}^*, z_c^*)$: true values of model parameters T_{act} and z_c.
- $T_{\mathrm{act}}(z_c;\beta,A)$: constraint function (20) calculated using trial value β; in $T_{\mathrm{act}}(z_c;\beta,A)$, z_c denotes the independent variable, and T_{act} the dependent variable.

Note that the data is generated with the true value β^*. In the calculation constraint function (20), we use the measured data and a trial value β since β^* is unknown. When $\beta=\beta^*$, the constraint function shares one common intersection for all values of A:

$$T_{\mathrm{act}}(z_c^*;\beta^*,A)=T_{\mathrm{act}}^*\quad\text{for all } A \tag{21}$$

when $\beta\neq\beta^*$, in general $(T_{\mathrm{act}}^*, z_c^*)$ is not on constraint curve $T_{\mathrm{act}}(z_c;\beta,A)$, and the intersection of a pair of constraint functions varies with the test conditions (values of A). We study the behavior of the intersection vs A. We make use of (21) and expand $T_{\mathrm{act}}(z_c;\beta,A)$ around (z_c^*,β^*). For conciseness, we introduce $\varepsilon\equiv\frac{\beta z_c}{A}$ and write (20) as:

$$T_{\mathrm{act}}(z_c;\beta,A)=\Phi\left(\xi;\frac{1}{A}\right),\quad \xi(\beta,\varepsilon)\equiv\frac{1}{\beta}F^{-1}(\varepsilon),\quad \varepsilon(\beta,z_c)\equiv\frac{\beta z_c}{A}$$

We apply the chain rule to calculate partial derivatives.

$$\frac{\partial T_{\text{act}}}{\partial z_c} = \frac{\partial}{\partial y}\Phi\left(\xi;\frac{1}{A}\right)\left(F^{-1}\right)'(\varepsilon)\frac{1}{A} \tag{22}$$

$$\begin{aligned}\frac{\partial T_{\text{act}}}{\partial \beta} &= \frac{\partial}{\partial y}\Phi\left(\xi;\frac{1}{A}\right)\left(F^{-1}\right)'(\varepsilon)\frac{1}{A}\cdot\frac{z_c}{\beta}\left[-\frac{F^{-1}(\varepsilon)}{\varepsilon\left(F^{-1}\right)'(\varepsilon)}+1\right] \\ &\equiv \frac{\partial T_{\text{act}}}{\partial z_c}\cdot\eta \quad \text{where } \eta \equiv \frac{z_c}{\beta}\left[-\frac{F^{-1}(\varepsilon)}{\varepsilon\left(F^{-1}\right)'(\varepsilon)}+1\right]\end{aligned} \tag{23}$$

Using these derivatives, we write out the expansion of $T_{\text{act}}\left(z_c;\beta,A\right)$.

$$T_{\text{act}}\left(z_c;\beta,A\right) = T_{\text{act}}^{*} + \left.\frac{\partial T_{\text{act}}}{\partial z_c}\right|_{\left(z_c^{*},\beta^{*}\right)}\cdot\left[\left(z_c - z_c^{*}\right) + \eta\big|_{\left(z_c^{*},\beta^{*}\right)}\left(\beta-\beta^{*}\right)\right] \tag{24}$$

The slope of $T_{\text{act}}\left(z_c;\beta,A\right)$ vs. z_c is $\left.\frac{\partial T_{\text{act}}}{\partial z_c}\right|_{\left(z_c^{*},\beta^{*}\right)}$, which is given in (22). In **Appendix A**, we show that the slope converges to zero as $A\to\infty$. It follows that

$$T_{\text{act}}\left(z_c;\beta,A=\infty\right) = T_{\text{act}}^{*} \quad \text{for all } \beta \tag{25}$$

(25) shows that in the limit of $A\to\infty$, the constraint curve is a horizontal line at T_{act}^{*}, independent of z_c and β. For finite A, $\frac{\partial T_{\text{act}}}{\partial z_c}\neq 0$ and T_{act} in (24) varies with z_c and β. We consider the intersection of $T_{\text{act}}\left(z_c;\beta,A\right)$ and $T_{\text{act}}\left(z_c;\beta,\infty\right)\equiv T_{\text{act}}^{*}$. The T_{act}-coordinate of the intersection is T_{act}^{*}. Let $z_c^{(I)}\left(\beta,A\right)$ denote the z_c-coordinate of the intersection. Solving for $z_c^{(I)}\left(\beta,A\right)$ from (24) and (25) leads to

$$z_c^{(I)}\left(\beta,A\right) = z_c^{*} - \eta\big|_{\left(z_c^{*},\beta^{*}\right)}\left(\beta-\beta^{*}\right) \tag{26}$$

The dependence of $z_c^{(I)}\left(\beta,A\right)$ on A is contained in $\eta\big|_{\left(z_c^{*},\beta^{*}\right)}$ given in (23). Using the expansion of $\frac{F^{-1}(\varepsilon)}{\varepsilon\left(F^{-1}\right)'(\varepsilon)}$ derived in (73) in **Appendix A**, we investigate the behavior of η at large A.

- **Case 1**: $f(0)\neq 0$.

$$\eta\big|_{\left(z_c^{*},\beta^{*}\right)} = \left.\frac{z_c}{\beta}\left(-\frac{a_1}{2a_0^{2}}\varepsilon\right)\right|_{\left(z_c^{*},\beta^{*}\right)} = \frac{-\left(z_c^{*}\right)^{2} f'(0)}{2\left(f(0)\right)^{2}}\cdot\frac{1}{A} \quad \text{for large } A$$

In case 1, as $A\to\infty$, the intersection $z_c^{(I)}\left(\beta,A\right)$ given by (26) converges to the true value z_c^{*} regardless of trial value β.

$$\lim_{A\to\infty} z_c^{(I)}\left(\beta,A\right) = z_c^{*} \quad \text{for all } \beta$$

The residual in convergence is proportional to $\left(\beta-\beta^{*}\right)/A$ and has the same sign as $f'(0)\left(\beta-\beta^{*}\right)$. More specifically, we have

$$z_c^{(I)}(\beta, A) = z_c^* + \frac{\left(z_c^*\right)^2 f'(0)}{2\left(f(0)\right)^2} \cdot \frac{\beta - \beta^*}{A} \quad \text{for large } A \tag{27}$$

- **Case 2:** $f(0) = 0$ but $f'(0) \neq 0$

$$\begin{aligned} \eta\Big|_{\left(z_c^*, \beta^*\right)} &= \frac{z_c}{\beta}\left(-1 - \frac{\sqrt{2}a_2}{3a_1^{3/2}}\varepsilon^{1/2}\right)\Bigg|_{\left(z_c^*, \beta^*\right)} \\ &= \frac{z_c^*}{\beta^*}\left(-1 - \frac{\sqrt{2\beta^* z_c^*}\, f''(0)}{3\left(f'(0)\right)^{3/2}} \cdot \frac{1}{\sqrt{A}}\right) \to \frac{-z_c^*}{\beta^*} \quad \text{for large } A \end{aligned} \tag{28}$$

In case 2, as $A \to \infty$, the intersection $z_c^{(I)}(\beta, A)$ given by (26) converges to

$$\lim_{A\to\infty} z_c^{(I)}(\beta, A) = z_c^* - \left(\frac{-z_c^*}{\beta^*}\right)\left(\beta - \beta^*\right) = z_c^* \frac{\beta}{\beta^*}$$

which is proportional to trial value β. The residual in convergence is proportional to $\left(\beta - \beta^*\right)/\sqrt{A}$ and has the same sign as $f''(0)\left(\beta - \beta^*\right)$. Asymptotically, $z_c^{(I)}$ is

$$z_c^{(I)}(\beta, A) = z_c^* \frac{\beta}{\beta^*} + \frac{\left(z_c^*\right)^{3/2}}{\left(\beta^*\right)^{1/2}} \cdot \frac{\sqrt{2} f''(0)}{3\left(f'(0)\right)^{3/2}} \cdot \frac{\beta - \beta^*}{\sqrt{A}} \quad \text{for large } A \tag{29}$$

with the analytical preparations above, we examine four types of parametric form for nociceptor density vs depth, depicted in Figure 17.

5. Type 1 Nociceptor Density: $\rho(y) = \rho_0 e^{-\beta y}$

For type 1 nociceptor density, the relative density takes the parametric form

$$\frac{\rho(y)}{\rho_0} = f(\beta y), \quad \text{where } f(s) = e^{-s} \tag{30}$$

The graph of type 1 $f(s)$ is plotted in Figure 17. It has the properties

$$f(0) = 1 \neq 0, \quad f'(0) = -1, \quad \max_{0 \le s < \infty} f(s) = 1$$

5.1. Reflex Time

The reflex time vs beam spot area is given by (19) and (17), namely,

$$t_{\text{ref}}(A) = \frac{t_0 \rho_m C_p}{K\mu^2}\left[1 + c_A\left(\frac{\mu z_c}{A}\right)^2 + \cdots\right], \quad c_A = \frac{1 - \operatorname{erfc}\left(\sqrt{t_0}\right)e^{t_0}}{2t_0 \operatorname{erfc}\left(\sqrt{t_0}\right)e^{t_0}} \tag{31}$$

As A increases, t_{ref} converges to its limit with the residual proportional to $1/A^2$:

$$t_{\text{ref}}(A) - t_{\text{ref}}(\infty) \sim \frac{1}{A^2}$$

Figure 1 plots the relation between t_{ref} and A in two ways. Left panel: t_{ref} vs A. Right panel: t_{ref} vs. $1/A$. In particular, the right panel confirms that the residual in the convergence of t_{ref} decays faster than $1/A$ for large A, as predicted in the analysis above.

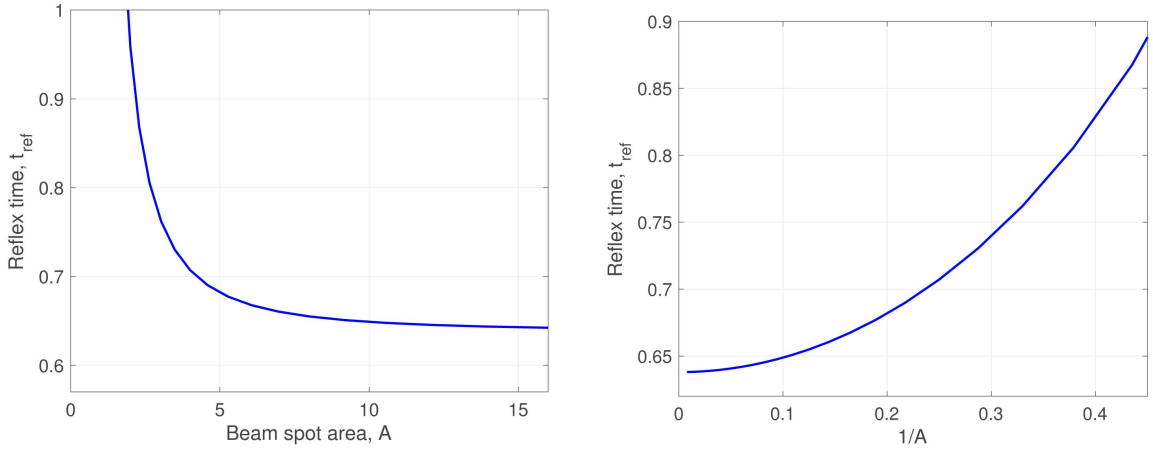

Figure 1. The relation between reflex time (t_{ref}) and beam spot area (A) for type 1 nociceptor density (30) with $\beta^* = 1$. Left panel: t_{ref} vs A. Right panel: t_{ref} vs $1/A$.

It is interesting to notice that expansion (31) is independent of β^*. Consequently, the measurements of $t_{\text{ref}}(A)$ vs. A do not contain any information for estimating β^*.

5.2. Constraint Function $T_{\text{act}}(z_c;\beta,A)$

We consider the intersection of the pair $T_{\text{act}}(z_c;\beta,A)$ and $T_{\text{act}}(z_c;\beta,\infty)\equiv T_{\text{act}}^*$. The z_c-coordinate of the intersection, $z_c^{(I)}(\beta,A)$, is generally described by (26). For type 1 density, we have $f(s)=\mathrm{e}^{-s}$, $f(0)=1\neq 0$ and $f'(0)=-1$, and the specific expression of $z_c^{(I)}(\beta,A)$ is given by (27).

$$z_c^{(I)}(\beta,A)=z_c^*-\frac{\left(z_c^*\right)^2}{2}\left(\beta-\beta^*\right)\cdot\frac{1}{A} \tag{32}$$

At $\beta=\beta^*$, the intersection $z_c^{(I)}(\beta^*,A)=z_c^*$ is independent of A. When $\beta\neq\beta^*$, the trend of $z_c^{(I)}(\beta,A)$ vs. A tells us whether $\beta>\beta^*$ or $\beta<\beta^*$.

- For $\beta>\beta^*$, $z_c^{(I)}(\beta,A)$ ascends toward z_c^* from below as A increases.
- For $\beta<\beta^*$, $z_c^{(I)}(\beta,A)$ descends toward z_c^* from above as A increases.

Figure 2 displays simulated $T_{\text{act}}(z_c;\beta,A)$ for several values of A, respectively for $\beta>\beta^*$ and for $\beta<\beta^*$. Here constraint function $T_{\text{act}}(z_c;\beta,A)$ is based on test data (which is generated with true value $\beta^*=1$) and is calculated using formulation (20) with trial value β. The trend of $z_c^{(I)}(\beta,A)$ vs A is illustrated in **Figure 3**. The simulation results in **Figure 2** and **Figure 3** confirm the theoretically predicted trend above.

When it is known that the nociceptor density has the parametric form of type 1 given in (30), we can tune the trial value β down or up toward the true value β^* depending on whether the calculated $z_c^{(I)}(\beta,A)$ increases or decreases with A.

5.3. Constraint Function Calculated Using the Uniform Density

We now consider the situation where the type of parametric form of $\rho(y)/\rho_0$

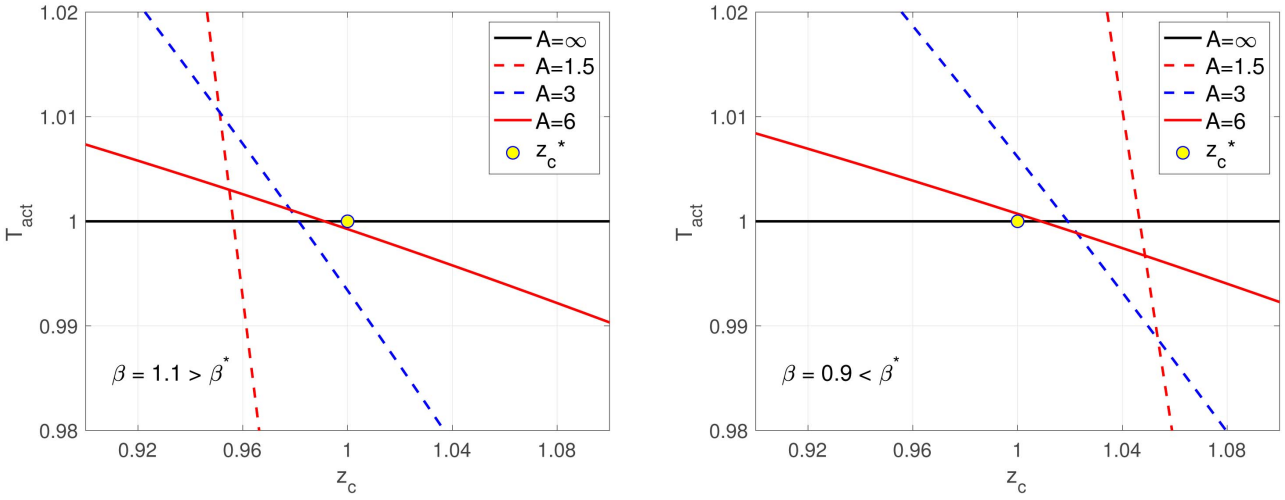

Figure 2. Constraint curves for type 1 density (30). $T_{\text{act}}(z_c;\beta,A)$ is based on test data generated with true value $\beta^*=1$, and calculated using (20) with trial value β. Left panel: $\beta>\beta^*$. Right panel: $\beta<\beta^*$.

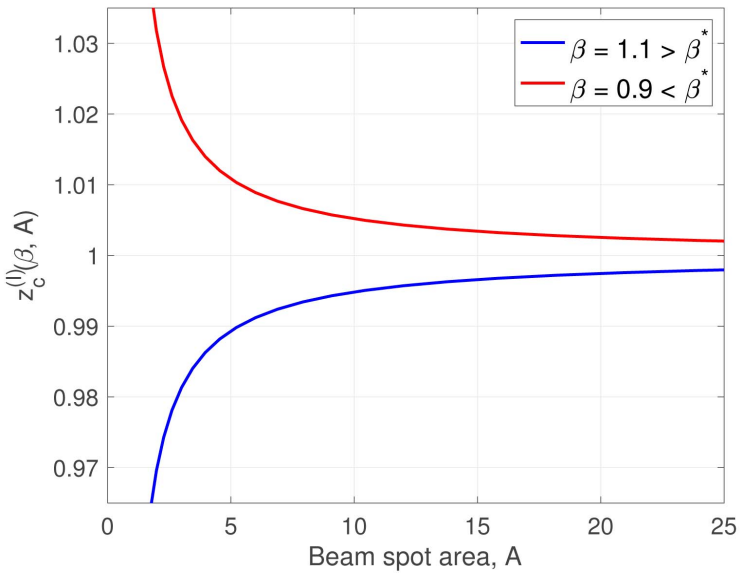

Figure 3. $z_c^{(I)}(\beta,A)$ vs. A, respectively for $\beta>\beta^*$ and for $\beta<\beta^*$. Here $z_c^{(I)}(\beta,A)$ is the intersection of $T_{\text{act}}(z_c;\beta,A)$ and $T_{\text{act}}(z_c;\beta,\infty)\equiv T_{\text{act}}^*$ from **Figure 2**.

is unknown. With no information on the type of density form, we use the uniform density as the trial density in calculating the constraint function. Let $T_{\text{act,uni}}(z_c;A)$ denote the constraint function based on the test data (which is generated using type 1 density (30) with true value β^*) and calculated using framework (20) with the *uniform trial density* $\rho(y)/\rho_0\equiv 1$. Notice that the uniform density is a member of type 1 family (30) with $\beta=0$. Thus, the two constraint functions $T_{\text{act,uni}}(z_c;A)$ and $T_{\text{act}}(z_c;\beta,A)$ are related by $T_{\text{act,uni}}(z_c;A)=T_{\text{act}}(z_c;\beta=0,A)$. Let $z_{c,\text{uni}}^{(I)}(A)$ denote the z_c-coordinate of the intersection of the pair $T_{\text{act,uni}}(z_c;A)$ and $T_{\text{act,uni}}(z_c;A=\infty)\equiv T_{\text{act}}^*$. Setting $\beta=0$ in (32), we obtain

$$z_{c,\text{uni}}^{(I)}(A) = z_c^* + \frac{\left(z_c^*\right)^2}{2}\beta^* \cdot \frac{1}{A} \tag{33}$$

Since the uniform density is parameter-free, the calculation of constraint function $T_{\text{act,uni}}(z_c; A)$ and intersection $z_{c,\text{uni}}^{(I)}(A)$ is based solely on the test data. It does not require any input parameter or knowledge of the function form of the true density. Once the test data is available, $T_{\text{act,uni}}(z_c; A)$ and $z_{c,\text{uni}}^{(I)}(A)$ can be calculated. When the true underlying density is type 1 given in (30), result (33) predicts that $z_{c,\text{uni}}^{(I)}(A)$ converges to z_c^* as $A \to \infty$ with the difference proportional to $1/A$. **Figure 4** compares simulated $z_{c,\text{uni}}^{(I)}(A)$ and $z_c^{(I)}(\beta, A)$. The simulation results validate the theoretical prediction. In particular, $z_{c,\text{uni}}^{(I)}(A)$ varies linearly with $1/A$. We fit function $c_0 + c_1/A$ to data of $z_{c,\text{uni}}^{(I)}(A)$ vs $1/A$. The fitting coefficients give us

$$z_c^* = c_0, \quad \beta^* = \frac{2c_1}{c_0^2}$$

Before we end this section, we clarify that result (33) predicts the behavior of constraint function $T_{\text{act,uni}}(z_c; A)$ calculated using the uniform trial density when the true underlying density affecting the test data is type 1 given in (30). When the true underlying density is of a different type, the behavior will be different. One objective of examining $T_{\text{act,uni}}(z_c; A)$ and $z_{c,\text{uni}}^{(I)}(A)$ is to identity the type of nociceptor density from the observed behavior of $z_{c,\text{uni}}^{(I)}(A)$ vs A, based on the theoretically predicted behaviors for a list of density types. In the subsequent sections, we will study more density types.

6. Type 2 Nociceptor Density: $\rho(y) = \rho_0 \cdot (\beta y)\mathrm{e}^{1-\beta y}$

For type 2 nociceptor density, the relative density has the parametric form

$$\frac{\rho(y)}{\rho_0} = f(\beta y), \quad \text{where } f(s) = s\mathrm{e}^{1-s} \tag{34}$$

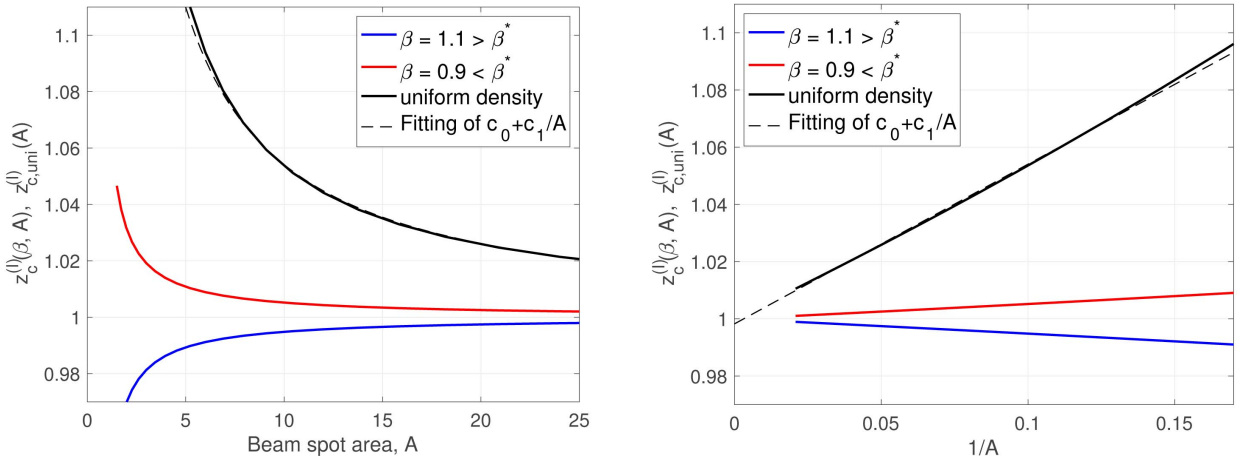

Figure 4. Simulated results of $z_{c,\text{uni}}^{(I)}(A)$ for type 1 density given in (30). Here $z_{c,\text{uni}}^{(I)}(A)$ is based on the data from the true density (with $\beta^* = 1$) but is calculated using the uniform trial density. Left panel: $z_{c,\text{uni}}^{(I)}(A)$ vs A. Right panel: $z_{c,\text{uni}}^{(I)}(A)$ vs. $1/A$.

The graph of type 2 $f(s)$ is shown in Figure 17. It is straightforward to see that

$$f(0)=0,\quad f'(0)=\mathrm{e}\neq 0,\quad f''(0)=-2\mathrm{e},\quad \max_{0\le s<\infty} f(s)=1$$

6.1. Reflex Time

The reflex time vs beam spot area is described by (19) and (18).

$$t_{\mathrm{ref}}(A)=\frac{t_0\rho_{\mathrm{m}}C_p}{K\mu^2}\left[1+c_A\cdot\frac{\mu z_c}{A}+\cdots\right],\quad c_A=\frac{\mu\left(1-\mathrm{erfc}\left(\sqrt{t_0}\right)\mathrm{e}^{t_0}\right)}{t_0\mathrm{e}\beta^*\mathrm{erfc}\left(\sqrt{t_0}\right)\mathrm{e}^{t_0}} \tag{35}$$

As A increases, t_{ref} converges to its limit with the difference proportional to $1/A$.

$$t_{\mathrm{ref}}(A)-t_{\mathrm{ref}}(\infty)\sim\frac{1}{A}$$

Figure 5 plots the relation between t_{ref} and A in two ways. Left panel: t_{ref} vs A. Right panel: t_{ref} vs $1/A$. In particular, the right panel confirms that t_{ref} is linear with respect to $1/A$ for large A, as predicted in the analysis above. This is in contrast with the convergence of $1/A^2$ for type 1 nociceptor density (30). To distinguish between these two density forms, we introduce an auxiliary quantity Q

$$Q\equiv\frac{t_{\mathrm{ref}}(A)-t_{\mathrm{ref}}(2A)}{t_{\mathrm{ref}}(2A)-t_{\mathrm{ref}}(4A)} \tag{36}$$

The theoretical prediction above tells us

$$Q=\begin{cases}4 & \text{if } \rho(y)=\rho_0\mathrm{e}^{-\beta y}\ (\text{type 1})\\ 2 & \text{if } \rho(y)=\rho_0\cdot(\beta y)\mathrm{e}^{1-\beta y}\ (\text{type 2})\end{cases} \tag{37}$$

In (35), coefficient c_A does contain β^*. However, in (35) β^* is tangled with

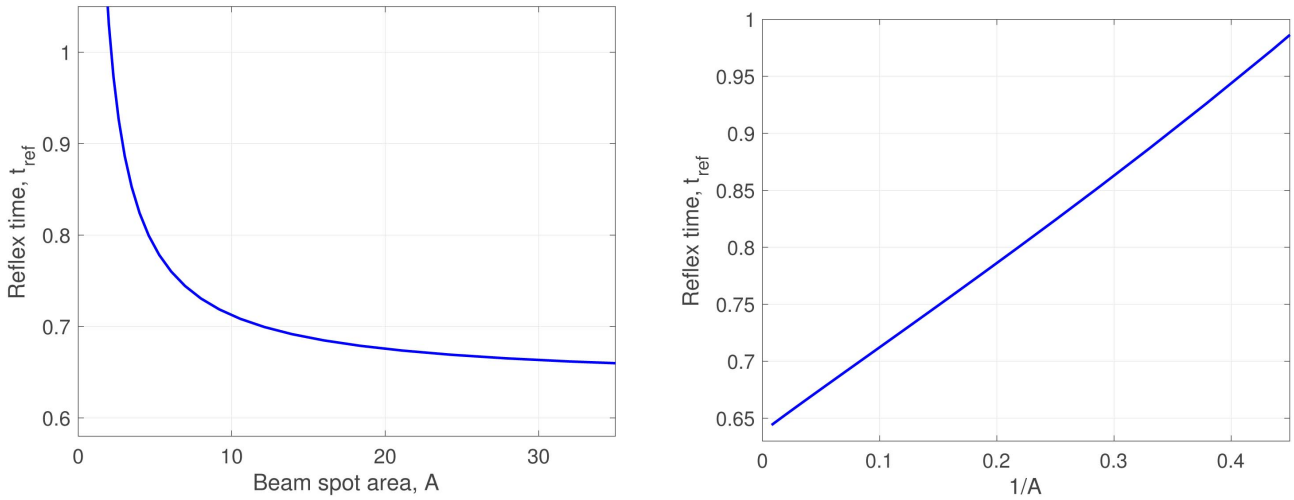

Figure 5. The relation between reflex time (t_{ref}) and beam spot area (A) for type 2 nociceptor density (34) with $\beta^*=1$. Left panel: t_{ref} vs A. Right panel: t_{ref} vs $1/A$.

other parameters. It is not possible to extract the value of β^* unless all other parameters are known.

6.2. Constraint Function $T_{\text{act}}(z_c;\beta,A)$

We consider the intersection of the pair $T_{\text{act}}(z_c;\beta,A)$ and $T_{\text{act}}(z_c;\beta,\infty)\equiv T_{\text{act}}^*$. The z_c-coordinate of the intersection, $z_c^{(I)}(\beta,A)$, is generally described by (26). For type 2 density, we have $f(s)=se^{1-s}$, $f(0)=0$, $f'(0)=e\neq 0$ and $f''(0)=-2e$, and the specific expression of $z_c^{(I)}(\beta,A)$ is given by (29).

$$z_c^{(I)}(\beta,A)=z_c^*\frac{\beta}{\beta^*}-\frac{\left(2z_c^*\right)^{3/2}}{3\sqrt{e\beta^*}}\left(\beta-\beta^*\right)\cdot\frac{1}{\sqrt{A}}$$

At $\beta=\beta^*$, the intersection $z_c^{(I)}(\beta^*,A)=z_c^*$ is independent of beam spot area A. When $\beta\neq\beta^*$, the trend of $z_c^{(I)}(\beta,A)$ vs A tells us whether $\beta>\beta^*$ or $\beta<\beta^*$.

- For $\beta>\beta^*$, $z_c^{(I)}(\beta,A)$ ascends toward $z_c^*\frac{\beta}{\beta^*}$ as A increases.
- For $\beta<\beta^*$, $z_c^{(I)}(\beta,A)$ descends toward $z_c^*\frac{\beta}{\beta^*}$ as A increases.

The increase/decrease trend of $z_c^{(I)}(\beta,A)$ vs. A is qualitatively the same as that for type 1 density given in (30). There are two differences. For type 2 density (34), we have 1) $\lim_{A\to\infty} z_c^{(I)}(\beta,A)=z_c^*\frac{\beta}{\beta^*}$, which varies with trial value β, and 2) the residual in convergence is proportional to $1/\sqrt{A}$, instead of $1/A$.

Figure 6 shows simulated $T_{\text{act}}(z_c;\beta,A)$ for several values of A, respectively for $\beta>\beta^*$ and for $\beta<\beta^*$. Here constraint function $T_{\text{act}}(z_c;\beta,A)$ is based on test data (which is generated with true value $\beta^*=1$) and is calculated using formulation (20) with trial value β. The trend of $z_c^{(I)}(\beta,A)$ vs A is shown in Figure 7. The simulation results in Figure 6 and Figure 7 confirm the theoretically predicted trend above.

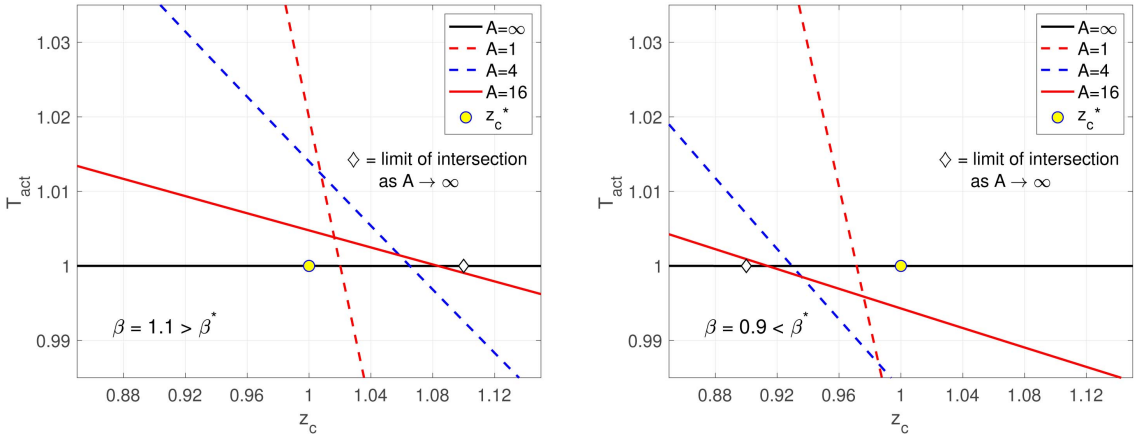

Figure 6. Constraint curves for type 2 density (34). $T_{\text{act}}(z_c;\beta,A)$ is based on test data generated with true value $\beta^*=1$, and calculated using (20) with trial value β. Left panel: $\beta>\beta^*$. Right panel: $\beta<\beta^*$.

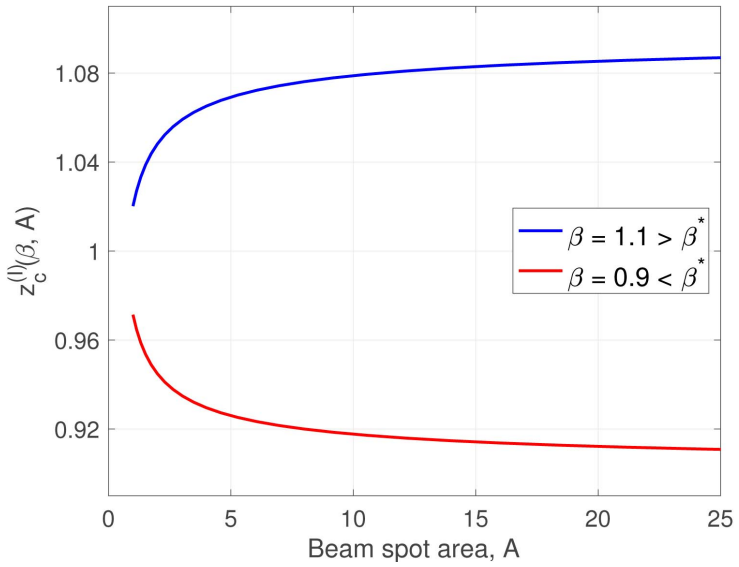

Figure 7. $z_c^{(I)}(\beta, A)$ vs. A, respectively for $\beta > \beta^* = 1$ and for $\beta < \beta^*$. Here $z_c^{(I)}(\beta, A)$ is the intersection of $T_{\text{act}}(z_c; \beta, A)$ and $T_{\text{act}}(z_c; \beta, \infty) \equiv T_{\text{act}}^*$ from **Figure 6**.

When it is known that the nociceptor density has the parametric form of type 2 given in (34), we can tune the trial value β down or up toward the true value β^* depending on whether the calculated $z_c^{(I)}(\beta, A)$ increases or decreases with A.

6.3. Constraint Function Calculated Using the Uniform Density

When the type of parametric form of $\rho(y)/\rho_0$ is unknown, we like to design a method to identify the true underlying density type among a set of candidate density types based on test data measured in experiments. In the analysis of reflex time above, we used quantity Q defined in (36), with behaviors described in (37), to distinguish between type 1 and type 2 densities. Now we look into using constraint functions as a tool for that purpose. With no information on the density type, we use the uniform density as the trial density in calculating the constraint function.

Let $T_{\text{act,uni}}(z_c; A)$ denote the constraint function based on the test data (which is generated using type 2 density (34) with true value β^*) and calculated using framework (20) with the *uniform trial density* $\rho(y)/\rho_0 \equiv 1$. We select the uniform density to make the calculation of constraint function parameter-free, based solely on the test data.

Note that the uniform density is not a member of type 2 family (34). Consequently, constraint function $T_{\text{act,uni}}(z_c; A)$ is not a special case of $T_{\text{act}}(z_c; \beta, A)$. To study the behavior of $T_{\text{act,uni}}(z_c; A)$, we try to connect it to $T_{\text{act}}(z_c; \beta^*, A)$, the true constraint function. Both $T_{\text{act,uni}}(z_c; A)$ and $T_{\text{act}}(z_c; \beta, A)$ are constructed from the same test data generated with the true underlying density (34). Each of them is calculated in framework (20) using a different type of trial density, and has different features:

- $T_{\text{act}}\left(z_c;\beta^*,A\right)$ is the constraint function calculated using the correct density type (34) with the true parameter value β^*. Operationally, the calculation of $T_{\text{act}}\left(z_c;\beta^*,A\right)$ is not realistic unless we know β^*. The theoretical advantage of $T_{\text{act}}\left(z_c;\beta^*,A\right)$ is that it shares a common intersection $\left(z_c^*,T_{\text{act}}^*\right)$ for all values of *A*.
- $T_{\text{act,uni}}\left(z_{c,\text{uni}};A\right)$ is the constraint function calculated using the uniform trial density. Operationally, we can always calculate $T_{\text{act,uni}}\left(z_{c,\text{uni}};A\right)$ from test data. However, the point $\left(z_c^*,T_{\text{act}}^*\right)$ in general is not on the curve $T_{\text{act,uni}}\left(z_{c,\text{uni}};A\right)$.

The two constraint functions above are unified in $\Phi\left(y;1/A\right)$ via y_{act}, as described in (4).

$$T_{\text{act}}=\Phi\left(y_{\text{act}};\frac{1}{A}\right) \tag{38}$$

The mapping between y_{act} and z_c, however, depends on the trial density. As a result, variable z_c is related to y_{act} differently in the two constraint functions. For clarity of the discussion, we use $z_{c,\text{uni}}$ to denote the variable in $T_{\text{act,uni}}\left(z_{c,\text{uni}};A\right)$, and use z_c for the variable in $T_{\text{act}}\left(z_c;\beta^*,A\right)$. The difference lies in the trial density used in the formulation. For the true density, z_c is related to y_{act} in (5). For the uniform density, $z_{c,\text{uni}}=A\cdot y_{\text{act}}$. Expressing y_{act} in terms of z_c or $z_{c,\text{uni}}$, we obtain

$$y_{\text{act}}=\begin{cases}\dfrac{1}{\beta^*}F^{-1}\left(\dfrac{\beta^* z_c}{A}\right) & \text{for } \rho(y)/\rho_0=\left(\beta^* y\right)\mathrm{e}^{1-\beta^* y}\\ \dfrac{z_{c,\text{uni}}}{A} & \text{for } \rho(y)/\rho_0=1\end{cases} \tag{39}$$

Combining (39) and (38), we write out $T_{\text{act,uni}}\left(z_{c,\text{uni}};A\right)$ and $T_{\text{act}}\left(z_c;\beta^*,A\right)$

$$T_{\text{act}}\left(z_c;\beta^*,A\right)=\Phi\left(\frac{1}{\beta^*}F^{-1}\left(\frac{\beta^* z_c}{A}\right);\frac{1}{A}\right)$$

$$T_{\text{act,uni}}\left(z_{c,\text{uni}};A\right)=\Phi\left(\frac{z_{c,\text{uni}}}{A};\frac{1}{A}\right) \tag{40}$$

Since $T_{\text{act}}\left(z_c;\beta^*,A\right)$ is calculated using the true density, it satisfies

$$T_{\text{act}}^*=\Phi\left(\frac{1}{\beta^*}F^{-1}\left(\frac{\beta^* z_c^*}{A}\right);\frac{1}{A}\right)\quad \text{for all } A$$

Taking the limit as $A\to\infty$ yields

$$T_{\text{act}}^*=\lim_{A\to\infty}\Phi\left(\frac{1}{\beta^*}F^{-1}\left(\frac{\beta^* z_c^*}{A}\right);\frac{1}{A}\right)=\Phi\left(0;0\right)$$

In (40), letting $A\to\infty$ and using $\Phi\left(0;0\right)=T_{\text{act}}^*$, we obtain

$$T_{\text{act,uni}}\left(z_{c,\text{uni}};\infty\right)=T_{\text{act}}^*$$

Let $z_{c,\text{uni}}^{(I)}\left(A\right)$ denote the intersection of the pair $T_{\text{act,uni}}\left(z_{c,\text{uni}};A\right)$ and $T_{\text{act,uni}}\left(z_{c,\text{uni}};\infty\right)\equiv T_{\text{act}}^*$. Both $z_{c,\text{uni}}^{(I)}\left(A\right)$ and $z_c^{(I)}\left(\beta^*,A\right)\equiv z_c^*$ are calculated by first mapping T_{act}^* to y_{act}^* and then mapping to $z_c^{(I)}$. Given the measured

temperature profile at reflex, Equation (38) maps T^*_{act} to a unique y^*_{act}, independent of the trial density. It follows that in (39), line 1 with $z_c^{(I)}\left(\beta^*, A\right) \equiv z_c^*$ and line 2 with $z^{(I)}_{c,\text{uni}}(A)$ are both equal to y^*_{act}.

$$\frac{1}{\beta^*} F^{-1}\left(\frac{\beta^*}{A} z_c^*\right) = y^*_{\text{act}} = \frac{z^{(I)}_{c,\text{uni}}(A)}{A}$$

Therefore, $z^{(I)}_{c,\text{uni}}(A)$ and z_c^* are related by

$$z^{(I)}_{c,\text{uni}}(A) = \frac{A}{\beta^*} F^{-1}\left(\frac{\beta^*}{A} z_c^*\right) \tag{41}$$

For type 2 density (34), the expansion of $F^{-1}(u)$ is given in (10) with $a_1 = f'(0) = \text{e}$ and $a_2 = f''(0) = -2\text{e}$. Substituting the expansion of $F^{-1}(u)$ into (41) yields

$$z^{(I)}_{c,\text{uni}}(A) = \frac{\sqrt{2A}}{\sqrt{\text{e}\beta^*}} \sqrt{z_c^*} + \frac{2}{3\text{e}} z_c^* \tag{42}$$

Figure 8 compares simulated $z^{(I)}_{c,\text{uni}}(A)$ and $z_c^{(I)}(\beta, A)$. The simulation results confirm the theoretical prediction. In particular, $z^{(I)}_{c,\text{uni}}(A)$ varies linearly with $\sqrt{A}$. We fit function $c_0 + c_1\sqrt{A}$ to the data of $z^{(I)}_{c,\text{uni}}(A)$ vs $\sqrt{A}$. The fitting coefficients give us

$$z_c^* = \frac{3\text{e}}{2} c_0, \quad \beta^* = \frac{3c_0}{c_1^2}$$

$z^{(I)}_{c,\text{uni}}(A)$ is the intersection of two constraint functions calculated from test data using the uniform trial density. Given the test data, the process of calculating $z^{(I)}_{c,\text{uni}}(A)$ is parameter-free. However, $z^{(I)}_{c,\text{uni}}(A)$ depends on the test data, which is affected by the underlying true density. When the true density has the type 2 form given in (34), result (42) predicts that $z^{(I)}_{c,\text{uni}}(A)$ increases linearly with $\sqrt{A}$, unbounded as $A \to \infty$. Result (42) for type 2 density is in sharp contrast

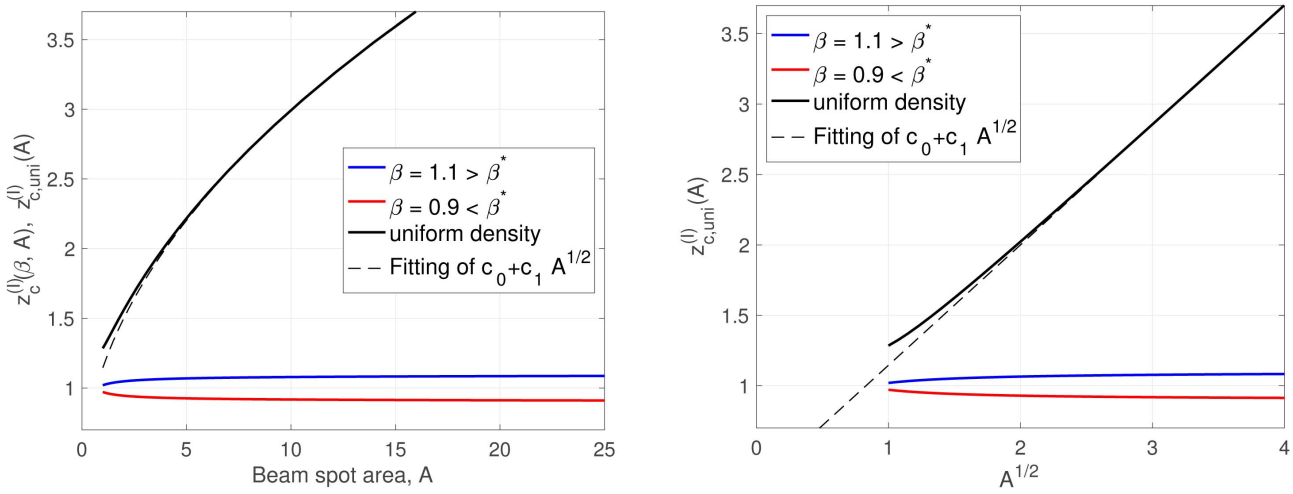

Figure 8. Simulated results of $z^{(I)}_{c,\text{uni}}(A)$ for type 2 density given in (34). Here $z^{(I)}_{c,\text{uni}}(A)$ is based on the data from the true density (with $\beta^* = 1$) but is calculated using the uniform trial density. Left panel: $z^{(I)}_{c,\text{uni}}(A)$ vs A. Right panel: $z^{(I)}_{c,\text{uni}}(A)$ vs. $\sqrt{A}$.

with the situation for type 1 density, described in (33) of Section 5, where $z_{c,\text{uni}}^{(I)}(A)$ converges to the true value z_c^* as $A \to \infty$. This difference in the behavior of $z_{c,\text{uni}}^{(I)}(A)$ vs. A provides another mechanism of distinguishing between type 1 and type 2 densities, in addition to the method of examining quantity Q, described in (37).

7. Type 3 Nociceptor Density: $\rho(y) = \rho_0 \cdot \theta(y - y_0)$

We write type 3 density in the same parametric form as that of types 1 and 2.

$$\frac{\rho(y)}{\rho_0} = f(\beta y), \quad f(s) = \theta(s-1), \quad \beta \equiv \frac{1}{y_0} \tag{43}$$

where $\theta(s)$ is the Heaviside step function.

$$\theta(s) = \begin{cases} 0, & s < 0 \\ 1, & s \geq 0 \end{cases} \tag{44}$$

The graph of type 3 $f(s)$ is shown in Figure 17. Type 3 density (43) is different from types 1 and 2 in that the nociceptor density jumps from 0 to ρ_0 at depth y_0. Because of the discontinuity, the Taylor expansions of $F(s)$ and $F^{-1}(u)$ derived in Section 3 are no longer valid. We write out $F(s)$ and $F^{-1}(u)$ directly

$$F(s) = \int_0^s \theta(s-1)\,\mathrm{d}s = \begin{cases} 0, & s < 1 \\ s-1, & s \geq 1 \end{cases}$$

$$F^{-1}(u) = u + 1 \quad \text{for } u > 0$$

The mapping between y_{act} and z_c is described by (7) and has the specific expression

$$y_{\text{act}}\big|_{(\text{reflex})} = \frac{1}{\beta} F^{-1}\left(\frac{\beta z_c}{A}\right) = \frac{z_c}{A} + y_0, \quad \beta \equiv \frac{1}{y_0} \tag{45}$$

7.1. Reflex Time

With the expression of y_{act} in (45), Equation (14) for $t_{\text{ref,nd}}$ becomes

$$\frac{(T_{\text{act}} - T_0) K \mu}{P_{\text{dep}}} = H\left(y_{\text{act,nd}}, t_{\text{ref,nd}}\right)$$

$$y_{\text{act,nd}} \equiv \mu y_{\text{act}} = \frac{1}{A_{\text{nd}}} + \mu y_0, \quad A_{\text{nd}} \equiv \frac{\mu z_c}{A}$$

In the limit of $A \to \infty$, we have $y_{\text{act,nd}} \to \mu y_0$ and the equation for $t_{\text{ref,nd}}$ converges to

$$\frac{(T_{\text{act}} - T_0) K \mu}{P_{\text{dep}}} = H\left(\mu y_0, t_{\text{ref,nd}}\big|_{A\to\infty}\right)$$

Consider $h(t \mid q) \equiv H(q,t)$ as a function of t with q as a parameter. Let $h^{-1}(u \mid q)$ be the inverse of $h(t \mid q)$ and $\tau_0(q) \equiv h^{-1}\left(\left.\frac{(T_{\text{act}} - T_0) K \mu}{P_{\text{dep}}}\right| q\right)$. As

$A \to \infty$, we have

$$t_{\text{ref,nd}}\big|_{A\to\infty} = \tau_0(\mu y_0)$$

By definition, $\tau_0(q)$ satisfies $H(q,\tau_0(q)) = \dfrac{(T_{\text{act}} - T_0)K\mu}{P_{\text{dep}}}$. We expand function $H(y_{\text{nd}}, t_{\text{nd}})$ around $(\mu y_0, \tau_0(\mu y_0))$ and write the equation for $t_{\text{ref,nd}}$ as

$$0 = \frac{\partial H(\mu y_0, \tau_0(\mu y_0))}{\partial t}\left(t_{\text{ref,nd}} - \tau_0(\mu y_0)\right) + \frac{\partial H(\mu y_0, \tau_0(\mu y_0))}{\partial y}\left(\frac{1}{A_{\text{nd}}}\right) \quad (46)$$

Substituting $t_{\text{ref,nd}}(A_{\text{nd}}) = \tau_0(\mu y_0)\left[1 + c_A\left(\dfrac{1}{A_{\text{nd}}}\right)^{\alpha} + \cdots\right]$ into (46) to calculate α and c_A, and then mapping back to the physical quantities, we obtain

$$t_{\text{ref}}(A) = \frac{\tau_0(\mu y_0)\rho_{\text{m}} C_p}{K\mu^2}\left[1 + c_A\left(\frac{\mu z_c}{A}\right) + \cdots\right],$$

$$c_A = \frac{\dfrac{-\partial H(\mu y_0, \tau_0(\mu y_0))}{\partial y}}{\tau_0(\mu y_0)\dfrac{\partial H(\mu y_0, \tau_0(\mu y_0))}{\partial t}}$$

As A increases, $t_{\text{ref}}(A)$ converges to its limit with the residual proportional to $1/A$.

$$t_{\text{ref}}(A) - t_{\text{ref}}(\infty) \sim \frac{1}{A}$$

This behavior is similar to that of type 2 density. For both type 2 and type 3, the nociceptor density is zero at the skin surface. Figure 9 plots the relation between t_{ref} and A in two ways. Left panel: t_{ref} vs A. Right panel: t_{ref} vs $1/A$. In particular, the right panel confirms that t_{ref} is linear with respect to $1/A$ for large A, as predicted in the analysis above.

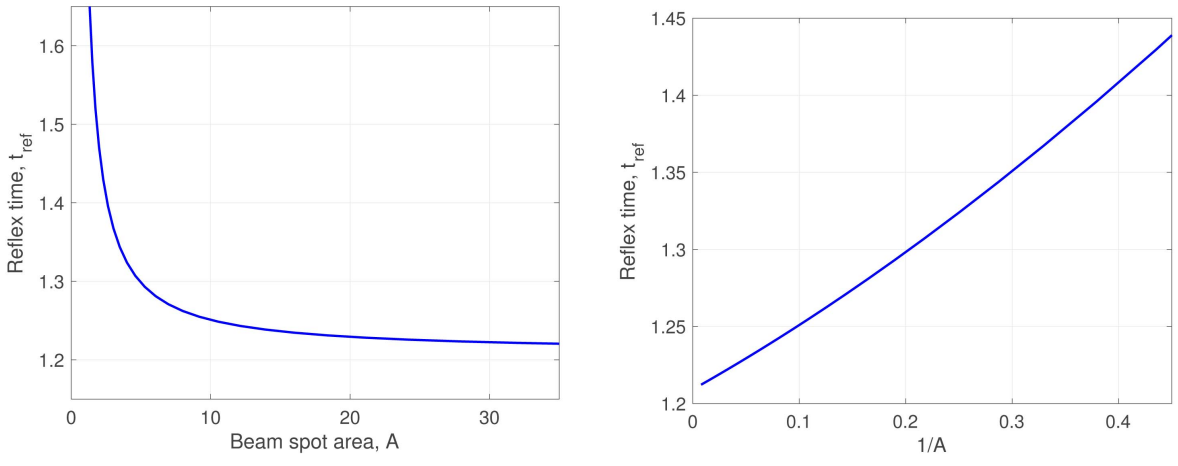

Figure 9. The reflex time (t_{ref}) as a function of beam spot area (A) for type 3 nociceptor density (43) with $y_0^* = \dfrac{1}{2}$. Left panel: t_{ref} vs A. Right panel: t_{ref} vs. $1/A$.

7.2. Constraint Function $T_{\text{act}}(z_c; y_0, A)$

For type 3 density, it is more sensible to use y_0 as the parameter since it has the clear physical meaning of the depth at which the nociceptor density jumps from 0 to ρ_0. In the unified parametric form in (43), the generic parameter is $\beta \equiv 1/y_0$. Mathematically, working with $\beta \equiv 1/y_0$ allows us to use general results of the unified parametric form obtained in previous sections. In the analysis below, we will go back and forth between y_0 and β.

We adopt the general convention of using y_0^* to denote the true value and y_0 to represent the variable. The general form of constraint function with trial value β is given in (20). Using $\beta = 1/y_0$ and $F^{-1}(u) = u + 1$, we write it as

$$T_{\text{act}}(z_c; y_0, A) = \Phi\left(\frac{z_c}{A} + y_0; \frac{1}{A}\right) \tag{47}$$

In the limit of $A \to \infty$, $T_{\text{act}}(z_c; y_0, A)$ converges to a horizontal line

$$T_{\text{act}}(z_c; y_0, A = \infty) = \Phi(y_0; 0)$$

At y_0^*, the constraint function shares the common intersection $(z_c^*, T_{\text{act}}^*)$ for all A.

$$T_{\text{act}}(z_c^*; y_0^*, A) = \Phi\left(\frac{z_c^*}{A} + y_0^*; \frac{1}{A}\right) = T_{\text{act}}^* \quad \text{for all } A$$

In particular, we have $\Phi(y_0^*; 0) = T_{\text{act}}^*$. We expand $\Phi\left(\frac{z_c}{A} + y_0; \frac{1}{A}\right)$ around $\left(\frac{z_c^*}{A} + y_0^*; \frac{1}{A}\right)$ and expand $\Phi(y_0; 0)$ around $(y_0^*, 0)$ to write them respectively as

$$\Phi\left(\frac{z_c}{A} + y_0; \frac{1}{A}\right) = T_{\text{act}}^* + \frac{\partial}{\partial y}\Phi\left(\frac{z_c^*}{A} + y_0^*; \frac{1}{A}\right)\left(\frac{z_c - z_c^*}{A} + y_0 - y_0^*\right) \tag{48}$$

$$\Phi(y_0; 0) = T_{\text{act}}^* + \frac{\partial}{\partial y}\Phi(y_0^*; 0)(y_0 - y_0^*) \tag{49}$$

Let $z_c^{(I)}(y_0, A)$ denote the z_c-coordinate of the intersection of $T_{\text{act}}(z_c; y_0, A)$ and $T_{\text{act}}(z_c; y_0, \infty)$. $z_c^{(I)}(y_0, A)$ is governed by equating the RHSs of (48) and (49).

$$\frac{\partial}{\partial y}\Phi\left(\frac{z_c^*}{A} + y_0^*; \frac{1}{A}\right)\left(\frac{z_c - z_c^*}{A} + y_0 - y_0^*\right) = \frac{\partial}{\partial y}\Phi(y_0^*; 0)(y_0 - y_0^*)$$

Solving for $z_c^{(I)}(y_0, A)$ yields

$$z_c^{(I)}(y_0, A) = z_c^* + A\left(\frac{\frac{\partial}{\partial y}\Phi(y_0^*; 0)}{\frac{\partial}{\partial y}\Phi\left(\frac{z_c^*}{A} + y_0^*; \frac{1}{A}\right)} - 1\right)(y_0 - y_0^*) \tag{50}$$

We expand $\frac{\partial}{\partial y}\Phi\left(\frac{z_c^*}{A} + y_0^*; \frac{1}{A}\right)$ with respect to $\frac{1}{A}$ into the form

$$\frac{\partial}{\partial y}\Phi\left(\frac{z_c^*}{A}+y_0^*;\frac{1}{A}\right)=\frac{\partial}{\partial y}\Phi\left(y_0^*;0\right)\left(1+\frac{b_1}{A}+\frac{b_2}{A^2}+\cdots\right) \tag{51}$$

Substituting the expansion into (50), we obtain

$$z_c^{(I)}\left(y_0,A\right)=z_c^*+\left(-b_1+\left(b_1^2-b_2\right)\frac{1}{A}\right)\left(y_0-y_0^*\right) \tag{52}$$

In **Appendix B**, we show that the coefficients satisfy

$$b_1>0 \quad \text{and} \quad \left(b_1^2-b_2\right)>0 \tag{53}$$

At $y_0=y_0^*$, the intersection $z_c^{(I)}\left(y_0^*,A\right)=z_c^*$ is independent of beam spot area A. When $y_0\neq y_0^*$, the trend of $z_c^{(I)}\left(y_0,A\right)$ vs A implies whether $y_0<y_0^*$ or $y_0>y_0^*$.

- For $y_0<y_0^*$, $z_c^{(I)}\left(y_0,A\right)$ ascends toward $z_c^*-b_1\left(y_0-y_0^*\right)>z_c^*$ as A increases.
- For $y_0>y_0^*$, $z_c^{(I)}\left(y_0,A\right)$ descends toward $z_c^*-b_1\left(y_0-y_0^*\right)<z_c^*$ as A increases.

In terms of $\beta\equiv 1/y_0$, the increase/decrease trend of $z_c^{(I)}$ vs A for type 3 density (43) resembles that for type 2 density (34). Both types of densities share the common feature that the nociceptor density is zero at skin surface: $\rho(0)=0$.

Figure 10 depicts simulated $T_{\text{act}}\left(z_c;y_0,A\right)$ for several values of A, respectively for $y_0<y_0^*$ and for $y_0>y_0^*$. Here constraint function $T_{\text{act}}\left(z_c;y_0,A\right)$ is based on test data (which is generated with true value $y_0^*=0.5$) and is calculated using formulation (47) with trial value y_0. The trend of $z_c^{(I)}\left(y_0,A\right)$ vs A is shown in Figure 11. The simulation results in Figure 10 and Figure 11 confirm the theoretically predicted trend above.

When it is known that the nociceptor density has the parametric form of type 3 given in (43), we can tune the trial value y_0 up or down toward the true value

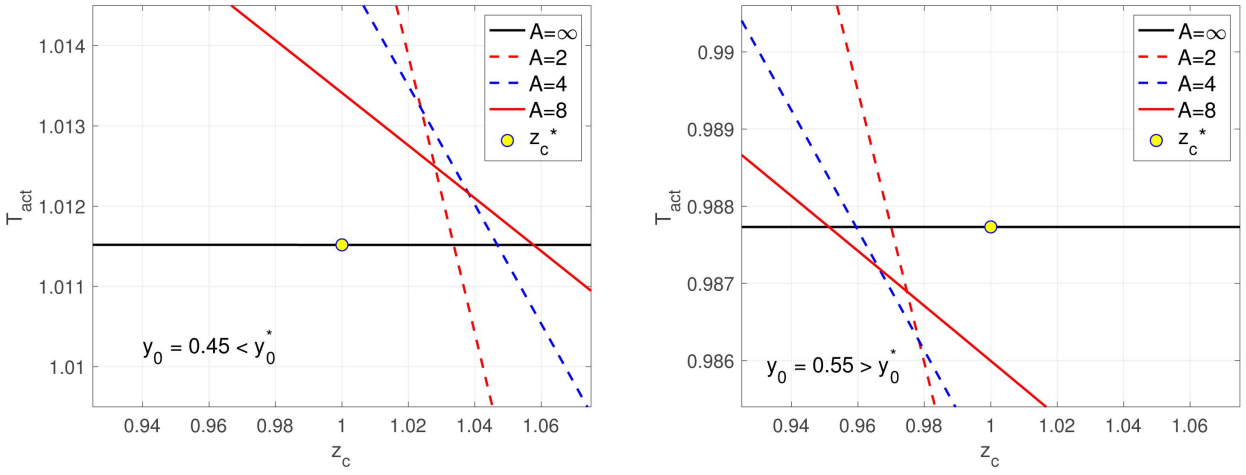

Figure 10. Constraint curves for type 3 density (43). $T_{\text{act}}\left(z_c;y_0,A\right)$ is based on test data generated with true value $y_0^*=0.5$, and calculated using (47) with trial value y_0. Left panel: $y_0<y_0^*$. Right panel: $y_0>y_0^*$. Notice that for type 3 density, $T_{\text{act}}\left(z_c;y_0,\infty\right)$ is a horizontal line, whose height varies with y_0.

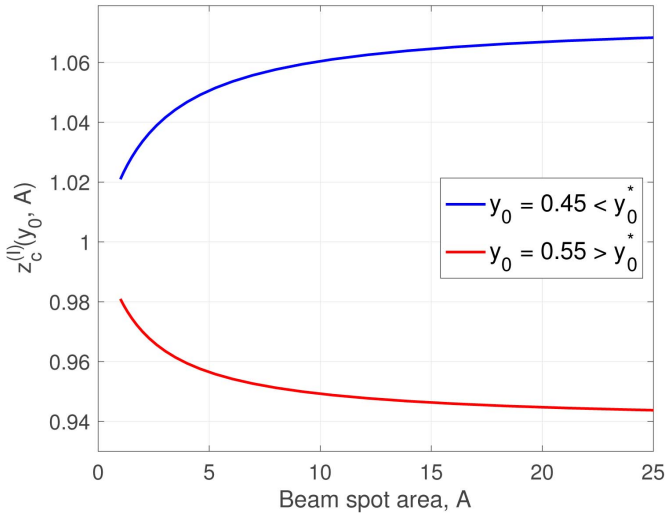

Figure 11. $z_c^{(I)}(y_0, A)$ vs A, respectively for $y_0 < y_0^* = 0.5$ and for $y_0 > y_0^*$. Here $z_c^{(I)}(y_0, A)$ is the intersection of $T_{\text{act}}(z_c; y_0, A)$ and $T_{\text{act}}(z_c; y_0, \infty)$ from **Figure 10**.

y_0^* depending on whether the calculated $z_c^{(I)}(y_0, A)$ increases or decreases with A.

7.3. Constraint Function Calculated Using the Uniform Density

When the type of parametric form of $\rho(y)/\rho_0$ is unknown, we apply the uniform trial density in calculating the constraint function and use it as a tool for probing the density type. This approach has the advantage of being operationally practical. Once the test data is available, the calculation of constraint function does not require any input parameters.

Let $T_{\text{act,uni}}(z_c; A)$ denote the constraint function based on the test data (which is generated using type 3 density (43) with true value y_0^*) and calculated using framework (47) with the *uniform trial density* $\rho(y)/\rho_0 \equiv 1$. For type 3 parametric family (43), the uniform density is a special case at $y_0 = 0$. However, expansions (48) and (49) are only for the case of y_0 near y_0^*, away from the skin surface. At $y_0 = 0$, the expansions will be different because of the insulated boundary condition $\frac{\partial}{\partial y}\Phi(0,t) = 0$. At $y_0 = 0$, we have

$$T_{\text{act,uni}}(z_c; A) = \Phi\left(\frac{z_c}{A}; \frac{1}{A}\right)$$

$$T_{\text{act,uni}}(z_c; \infty) = \Phi(0;0)$$

We expand $\Phi\left(\frac{z_c}{A}; \frac{1}{A}\right)$ around $(0;0)$. It follows that

$$\Phi\left(\frac{z_c}{A}; \frac{1}{A}\right) = \Phi(0;0) + \frac{\partial}{\partial v}\Phi(0;0)\frac{1}{A} + \frac{1}{2}\frac{\partial^2}{\partial y^2}\Phi(0;0)\frac{z_c^2}{A^2} + \frac{1}{2}\frac{\partial^2}{\partial v^2}\Phi(0;0)\frac{1}{A^2} + \frac{\partial^2}{\partial y \partial v}\Phi(0;0)\frac{z_c}{A^2} + \cdots$$

Let $z_{c,\mathrm{uni}}^{(I)}(A)$ denote the intersection of $T_{\mathrm{act,uni}}(z_c;A)$ and $T_{\mathrm{act,uni}}(z_c;\infty)$. It satisfies

$$\Phi_{yy}\left(z_{c,\mathrm{uni}}^{(I)}\right)(A)^2+2\Phi_{yv}z_{c,\mathrm{uni}}^{(I)}(A)+2\Phi_v A+\Phi_{vv}+\cdots=0$$

All derivatives are evaluated at $(0;0)$. Solving for $z_{c,\mathrm{uni}}^{(I)}(A)$, we obtain

$$z_{c,\mathrm{uni}}^{(I)}(A)=\sqrt{\frac{\Phi_v}{-\Phi_{yy}}}\cdot\sqrt{A}+\frac{2\Phi_{yv}}{-\Phi_{yy}}+\cdots \tag{54}$$

Result (54) predicts that when the true underlying density is type 3 given in (43), $z_{c,\mathrm{uni}}^{(I)}(A)$ increases linearly with $\sqrt{A}$, unbounded as $A\to\infty$. This behavior is similar to that for type 2 density. Both type 3 and type 2 share the common feature of $\rho(0)=0$. **Figure 12** compares simulated $z_{c,\mathrm{uni}}^{(I)}(A)$ and $z_c^{(I)}(y_0,A)$. The simulation results confirm the theoretical prediction.

8. Type 4 Nociceptor Density: $\rho(y)=\rho_0\left(1-\theta(y-y_0)/2\right)$

We represent type 4 density in the same parametric form as that of types 1 - 3.

$$\frac{\rho(y)}{\rho_0}=f(\beta y),\quad f(s)=1-\frac{1}{2}\theta(s-1),\quad \beta\equiv\frac{1}{y_0} \tag{55}$$

where $\theta(s)$ is the Heaviside step function defined in (44). The graph of type 4 $f(s)$ is shown in **Figure 17**. Type 4 relative density (55) has value 1 in $[0,y_0]$, and drops down to value 0.5 for $y>y_0$. When beam spot area A is sufficiently large, only a small depth of the skin needs to reach the activation temperature in order to trigger the withdrawal reflex. Thus, for large A, the behaviors of type 4 density are the same as those of the uniform density. For the purpose of revealing the effect of density jump at $y=y_0$, we examine the reflex time and the temperature profile at reflex in an intermediate range of A corresponding to the situation where the activated depth is around the density jump ($y=y_0$).

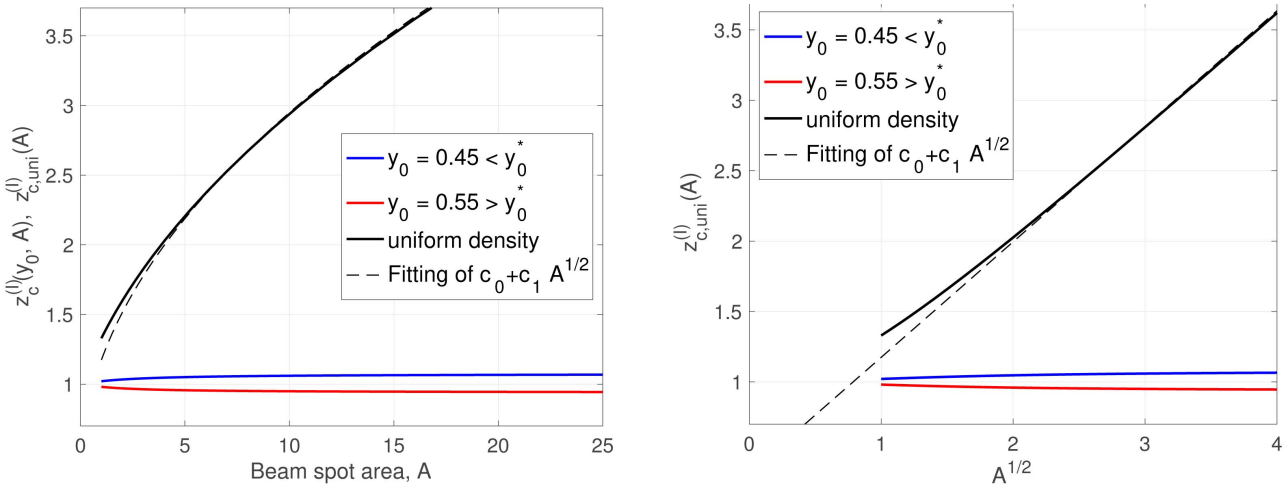

Figure 12. Simulated results of $z_{c,\mathrm{uni}}^{(I)}(A)$ for type 3 density given in (43). Here $z_{c,\mathrm{uni}}^{(I)}(A)$ is based on the data from the true density (with $y_0^*=0.5$) but is calculated using the uniform trial density. Left panel: $z_{c,\mathrm{uni}}^{(I)}(A)$ vs. A. Right panel: $z_{c,\mathrm{uni}}^{(I)}(A)$ vs $\sqrt{A}$.

8.1. Reflex Time

Because of the discontinuity in density profile (8), the Taylor expansions of $F(s)$ and $F^{-1}(u)$ derived in Section 3 are no longer valid. We write out $F(s)$ and $F^{-1}(u)$ directly.

$$F(s)=\int_0^s\left(1-\frac{1}{2}\theta(s-1)\right)\mathrm{d}s=\begin{cases}s, & s<1\\ \frac{1}{2}(s+1), & s\geq 1\end{cases}$$

$$F^{-1}(u)=\begin{cases}u, & u<1\\ 2u-1, & u\geq 1\end{cases} \tag{56}$$

The activated depth at reflex given in (7) has the expression

$$y_{\text{act}}\big|_{(\text{reflex})}(A)=y_0F^{-1}\left(\frac{z_c}{y_0A}\right)=\begin{cases}\frac{z_c}{A}, & \frac{z_c}{A}<y_0\\ 2\frac{z_c}{A}-y_0, & \frac{z_c}{A}\geq y_0\end{cases} \tag{57}$$

The non-dimensional reflex time $t_{\text{ref,nd}}$ is related to A via $y_{\text{act}}(A)$ in Equation (14).

$$\frac{(T_{\text{act}}-T_0)K\mu}{P_{\text{dep}}}=H\left(\mu y_{\text{act}}(A),t_{\text{ref,nd}}\right) \tag{58}$$

Conventionally, we view $t_{\text{ref,nd}}$ as a function of A since in experiments the beam spot area is prescribed in test design and the corresponding reflex time is observed. To facilitate the mathematically analysis, we view A as a function of $t_{\text{ref,nd}}$. We study function $A\left(t_{\text{ref,nd}}\right)$ for type 4 density and connect it to its counterpart for the uniform density. Let

- $A^{(\text{tp4})}\left(t_{\text{ref,nd}}\right)$: function A vs. $t_{\text{ref,nd}}$ for type 4 density
- $A^{(\text{uni})}\left(t_{\text{ref,nd}}\right)$: function A vs. $t_{\text{ref,nd}}$ for the uniform density
- $t_{\text{ref,nd}}^{(\text{tp4})}(1/A)$: function $t_{\text{ref,nd}}$ vs. $1/A$ for type 4 density
- $t_{\text{ref,nd}}^{(\text{uni})}(1/A)$: function $t_{\text{ref,nd}}$ vs. $1/A$ for the uniform density.

For any given value of $t_{\text{ref,nd}}$, the corresponding $y_{\text{act}}\left(t_{\text{ref,nd}}\right)$ is completely determined by Equation (58), independent of the nociceptor density. We use $y_{\text{act}}\left(t_{\text{ref,nd}}\right)$ to connect $A^{(\text{tp4})}\left(t_{\text{ref,nd}}\right)$ and $A^{(\text{uni})}\left(t_{\text{ref,nd}}\right)$. For type 4 density, $y_{\text{act}}\left(A^{(\text{tp4})}\right)$ is given in (57). Its inverse function is

$$A^{(\text{tp4})}\left(y_{\text{act}}\right)=\frac{z_c}{y_0}\cdot\frac{1}{F\left(\frac{y_{\text{act}}}{y_0}\right)}=\begin{cases}\frac{z_c}{y_{\text{act}}}, & y_{\text{act}}<y_0\\ \frac{2z_c}{y_{\text{act}}+y_0}, & y_{\text{act}}\geq y_0\end{cases} \tag{59}$$

For the uniform density, $f(s)=1$, $F(s)=s$, and $A^{(\text{uni})}\left(y_{\text{act}}\right)$ is given by

$$A^{(\text{uni})}\left(y_{\text{act}}\right)=\frac{z_c}{y_0}\cdot\frac{1}{F\left(\frac{y_{\text{act}}}{y_0}\right)}=\frac{z_c}{y_{\text{act}}} \tag{60}$$

Combining (59) and (60), we can express $1/A^{(\text{uni})}$ in terms of $1/A^{(\text{tp4})}$.

$$\frac{1}{A^{(\mathrm{uni})}}=\begin{cases}\dfrac{1}{A^{(\mathrm{tp4})}}, & \dfrac{1}{A^{(\mathrm{tp4})}}<\dfrac{y_0}{z_c}\\ \dfrac{2}{A^{(\mathrm{tp4})}}-\dfrac{y_0}{z_c}, & \dfrac{1}{A^{(\mathrm{tp4})}}\geq\dfrac{y_0}{z_c}\end{cases} \tag{61}$$

(61) described the relation between $1/A^{(\mathrm{tp4})}\left(t_{\mathrm{ref,nd}}\right)$ and $1/A^{(\mathrm{uni})}\left(t_{\mathrm{ref,nd}}\right)$. Now we treat $t_{\mathrm{ref,nd}}$ as the dependent variable and view it as a function of $1/A$. (61) leads to

$$t_{\mathrm{ref,nd}}^{(\mathrm{tp4})}\left(1/A\right)=\begin{cases}t_{\mathrm{ref,nd}}^{(\mathrm{uni})}\left(1/A\right), & \dfrac{1}{A}<\dfrac{y_0}{z_c}\\ t_{\mathrm{ref,nd}}^{(\mathrm{uni})}\left(\dfrac{2}{A}-\dfrac{y_0}{z_c}\right), & \dfrac{1}{A}\geq\dfrac{y_0}{z_c}\end{cases} \tag{62}$$

Equation (62) reveals that $t_{\mathrm{ref,nd}}^{(\mathrm{tp4})}\left(1/A\right)$ is obtained from $t_{\mathrm{ref,nd}}^{(\mathrm{uni})}\left(1/A\right)$ by a piecewise linear scaling on the independent variable $1/A$. Function $t_{\mathrm{ref,nd}}^{(\mathrm{uni})}\left(1/A\right)$ is smooth. After the piecewise linear scaling, $t_{\mathrm{ref,nd}}^{(\mathrm{tp4})}\left(1/A\right)$ has a discontinuity in derivative. Figure 13 plots the relation between $t_{\mathrm{ref}}^{(\mathrm{tp4})}$ and A in two ways. Left panel: t_{ref} vs. $1/A$. Right panel: derivative of t_{ref} vs. $1/A$. In particular, the right panel verifies that t_{ref} vs. $1/A$ has a discontinuity in derivative, as predicted in the analysis above.

8.2. Constraint Function $T_{\mathrm{act}}\left(z_c;y_0,A\right)$

For type 4 density, it is more sensible to choose y_0 as the parameter since it has the clear physical meaning of the depth at which the nociceptor density drops sharply from ρ_0 to $\rho_0/2$. In the unified parametric form in (55), the generic parameter is $\beta\equiv 1/y_0$. We adopt the general convention of using y_0^* to denote the true value and y_0 to represent the variable. The general form of constraint function with trial value β is given in (20). Using $\beta=1/y_0$ and $F^{-1}(u)$ given in (56), we write it as

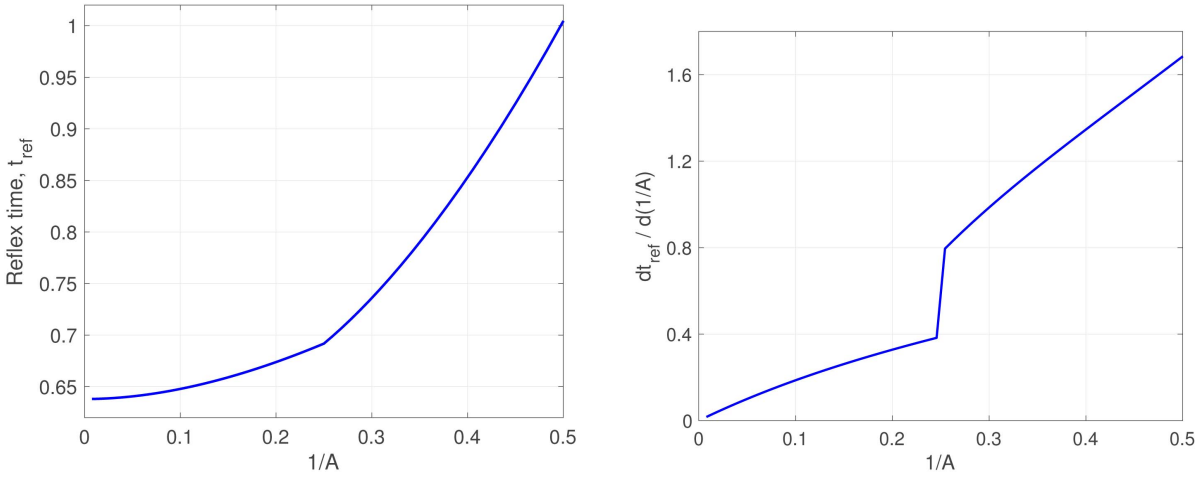

Figure 13. The relation between reflex time (t_{ref}) and beam spot area (A) for type 4 density (55) with $y_0^*=0.25$. Left panel: t_{ref} vs $1/A$. Right panel: derivative of t_{ref} vs. $1/A$.

$$T_{\text{act}}\left(z_c; y_0, A\right) = \begin{cases} \Phi\left(\frac{z_c}{A}; \frac{1}{A}\right), & \frac{z_c}{A} < y_0 \\ \Phi\left(2\frac{z_c}{A} - y_0; \frac{1}{A}\right), & \frac{z_c}{A} \geq y_0 \end{cases} \tag{63}$$

when beam spot area A is sufficiently large to make $\frac{z_c^*}{A} < y_0^*$, (57) gives $y_{\text{act}} < y_0^*$ and the measured data for type 4 density is the same as that for the uniform density. Constraint function (63) is based on the data for true value y_0^* and is calculated with trial value y_0. For any positive trial value $y_0 > 0$ and a finite interval of z_c near z_c^* in consideration, when A is sufficiently large, we have $\frac{\text{Interval of } z_c}{A} < \min\left(y_0^*, y_0\right)$ and

$$T_{\text{act}}\left(z_c; y_0, A\right) = \Phi\left(\frac{z_c}{A}; \frac{1}{A}\right) \quad \text{for large } A$$

Here $\Phi\left(\frac{z_c}{A}; \frac{1}{A}\right)$ is the constraint function based on the data for the uniform density and is calculated using the uniform trial density. $\Phi\left(\frac{z_c}{A}; \frac{1}{A}\right)$ is independent of trial value y_0, and passes through $\left(z_c^*, T_{\text{act}}^*\right)$ for all values of A.

$$\Phi\left(\frac{z_c^*}{A}; \frac{1}{A}\right) = T_{\text{act}}^* \quad \text{for all } A$$

In the limit of $1/A \to 0$, we have $\Phi\left(0;0\right) = T_{\text{act}}^*$. Let $z_c^{(I)}\left(y_0, A\right)$ denote the z_c-coordinate of the intersection of $T_{\text{act}}\left(z_c; y_0, A\right)$ and $T_{\text{act}}\left(z_c; y_0, \infty\right)$. Our analysis above shows that

- For any y_0, $T_{\text{act}}\left(z_c; y_0, A\right) = \Phi\left(\frac{z_c}{A}; \frac{1}{A}\right)$ when A is sufficiently large.
- For any y_0, $T_{\text{act}}\left(z_c; y_0, A = \infty\right) = \Phi\left(0;0\right) = T_{\text{act}}^*$.
- For any y_0, $z_c^{(I)}\left(y_0, A\right) = z_c^*$ when A is sufficiently large.

More specifically, to have $z_c^{(I)}\left(y_0, A\right) = z_c^*$, we only need $T_{\text{act}}\left(z_c; y_0, A\right) = \Phi\left(\frac{z_c}{A}; \frac{1}{A}\right)$ for z_c near z_c^*. The condition $\frac{\text{Interval of } z_c}{A} < \min\left(y_0^*, y_0\right)$ becomes $A > \frac{z_c^*}{\min\left(y_0^*, y_0\right)}$. We conclude that

$$z_c^{(I)}\left(y_0, A\right) = z_c^* \quad \text{for } A > \frac{z_c^*}{\min\left(y_0^*, y_0\right)} \tag{64}$$

Thus, for large A, $z_c^{(I)}\left(y_0, A\right)$ is independent of y_0. To probe the position of trial value y_0 relative to true value y_0^*, we need to examine the behavior of $z_c^{(I)}\left(y_0, A\right)$ for $A < \frac{z_c^*}{\max\left(y_0^*, y_0\right)}$. In this range of A, constraint function (63) takes the form

$$T_{\text{act}}\left(z_c; y_0, A\right) = \Phi\left(2\frac{z_c}{A} - y_0; \frac{1}{A}\right)$$

At true value y_0^*, $T_{\text{act}}\left(z_c; y_0^*, A\right)$ shares the common intersection $\left(z_c^*, T_{\text{act}}^*\right)$ for all A.

$$\Phi\left(2\frac{z_c^*}{A} - y_0^*; \frac{1}{A}\right) = T_{\text{act}}^*$$

We expand $\Phi\left(2\frac{z_c}{A} - y_0; \frac{1}{A}\right)$ around $\left(\frac{2z_c^*}{A} - y_0^*, \frac{1}{A}\right)$.

$$\Phi\left(2\frac{z_c}{A} - y_0; \frac{1}{A}\right) = T_{\text{act}}^* + \frac{\partial}{\partial y}\Phi\left(2\frac{z_c^*}{A} - y_0^*; \frac{1}{A}\right)\left(2\frac{z_c - z_c^*}{A} - \left(y_0 - y_0^*\right)\right)$$

Setting the LHS to T_{act}^* and solving for z_c, we obtain $z_c^{(I)}\left(y_0, A\right)$

$$z_c^{(I)}\left(y_0, A\right) = z_c^* + \frac{A}{2}\left(y_0 - y_0^*\right) \quad \text{for } A < \frac{z_c^*}{\max\left(y_0^*, y_0\right)} \tag{65}$$

For $y_0 < y_0^*$ and $\frac{z_c^*}{y_0^*} < A < \frac{z_c^*}{y_0}$, the activated depth at reflex is $y_{\text{act}}^* = \frac{z_c^*}{A} > y_0$. Substituting the expression of y_{act}^* into (57) and solving for z_c, we have

$$z_c^{(I)}\left(y_0, A\right) = z_c^* - \frac{1}{2}\left(z_c^* - Ay_0\right) \quad \text{for } \frac{z_c^*}{y_0^*} < A < \frac{z_c^*}{y_0} \tag{66}$$

For $y_0 > y_0^*$ and $\frac{z_c^*}{y_0} < A < \frac{z_c^*}{y_0^*}$, the activated depth at reflex is $y_{\text{act}}^* = 2\frac{z_c^*}{A} - y_0^*$. This y_{act}^* may or may not be beyond depth y_0. The case of $y_{\text{act}}^* > y_0$ corresponds to $A < \frac{2z_c^*}{y_0 + y_0^*}$. Substituting the expression of y_{act}^* into (57) and solving for z_c yields

$$z_c^{(I)}\left(y_0, A\right) = z_c^* + \frac{A}{2}\left(y_0 - y_0^*\right) \quad \text{for } \frac{z_c^*}{y_0} < A < \frac{2z_c^*}{y_0 + y_0^*} \tag{67}$$

Similarly, the case of $y_{\text{act}}^* < y_0$ corresponds to $A > \frac{2z_c^*}{y_0 + y_0^*}$. We get

$$z_c^{(I)}\left(y_0, A\right) = z_c^* + \left(z_c^* - Ay_0^*\right) \quad \text{for } \frac{2z_c^*}{y_0 + y_0^*} < A < \frac{z_c^*}{y_0^*} \tag{68}$$

Summarizing results for various cases, we write out a complete description of $z_c^{(I)}\left(y_0, A\right)$.

The case of $y_0 < y_0^*$,

$$z_c^{(I)}\left(y_0, A\right) = \begin{cases} z_c^* + \frac{A}{2}\left(y_0 - y_0^*\right) & \text{for } A < \frac{z_c^*}{y_0^*} \\ z_c^* - \frac{1}{2}\left(z_c^* - Ay_0\right) & \text{for } \frac{z_c^*}{y_0^*} < A < \frac{z_c^*}{y_0} \\ z_c^* & \text{for } A > \frac{z_c^*}{y_0} \end{cases}$$

The case of $y_0 > y_0^*$,

$$z_c^{(I)}(y_0, A) = \begin{cases} z_c^* + \dfrac{A}{2}(y_0 - y_0^*) & \text{for } A < \dfrac{2z_c^*}{y_0^* + y_0} \\ z_c^* + (z_c^* - Ay_0^*) & \text{for } \dfrac{2z_c^*}{y_0^* + y_0} < A < \dfrac{z_c^*}{y_0^*} \\ z_c^* & \text{for } A > \dfrac{z_c^*}{y_0^*} \end{cases} \tag{69}$$

At $y_0 = y_0^*$, we have $z_c^{(I)}(y_0^*, A) = z_c^*$ for all A. When $y_0 \neq y_0^*$, $z_c^{(I)}(y_0, A)$ has non-trivial dependence on A. The trend of $z_c^{(I)}(y_0, A)$ vs A tells us whether $y_0 < y_0^*$ or $y_0 > y_0^*$.

- When $y_0 < y_0^*$, from small A to large A, $z_c^{(I)}(y_0, A)$ starts below z_c^*, decreases further below z_c^*, and then reverts rapidly back to z_c^* and stays there.
- When $y_0 > y_0^*$, from small A to large A, $z_c^{(I)}(y_0, A)$ starts above z_c^*, increases further above z_c^*, and then reverts rapidly back to z_c^* and remains there.

Figure 14 shows simulated $T_{\text{act}}(z_c; y_0, A)$ for several values of A, respectively for $y_0 < y_0^*$ and for $y_0 > y_0^*$. Here constraint function $T_{\text{act}}(z_c; y_0, A)$ is based on test data (which is generated with true value $y_0^* = 0.25$) and is calculated using formulation (63) with trial value y_0. The trend of $z_c^{(I)}(y_0, A)$ vs A is shown in Figure 15. The simulation results in Figure 14 and Figure 15 confirm the theoretically predicted trend above.

When it is known that the nociceptor density has the parametric form of type 4 given in (55), we can tune the trial value y_0 up or down toward the true value y_0^* depending on the behavior of the calculated $z_c^{(I)}(y_0, A)$ vs. A.

8.3. Constraint Function Calculated Using the Uniform Density

When the type of parametric form of $\rho(y)/\rho_0$ is unknown, we use the uniform

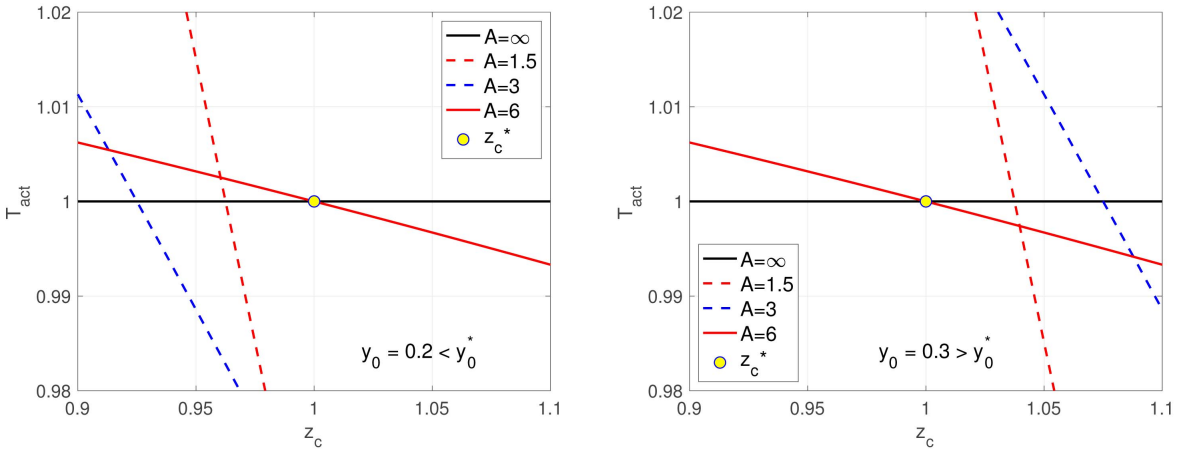

Figure 14. Constraint curves for type 4 density (55). $T_{\text{act}}(z_c; y_0, A)$ is based on test data generated with true value $y_0^* = 0.25$, and calculated using (63) with trial value y_0. Left panel: $y_0 < y_0^*$. Right panel: $y_0 > y_0^*$.

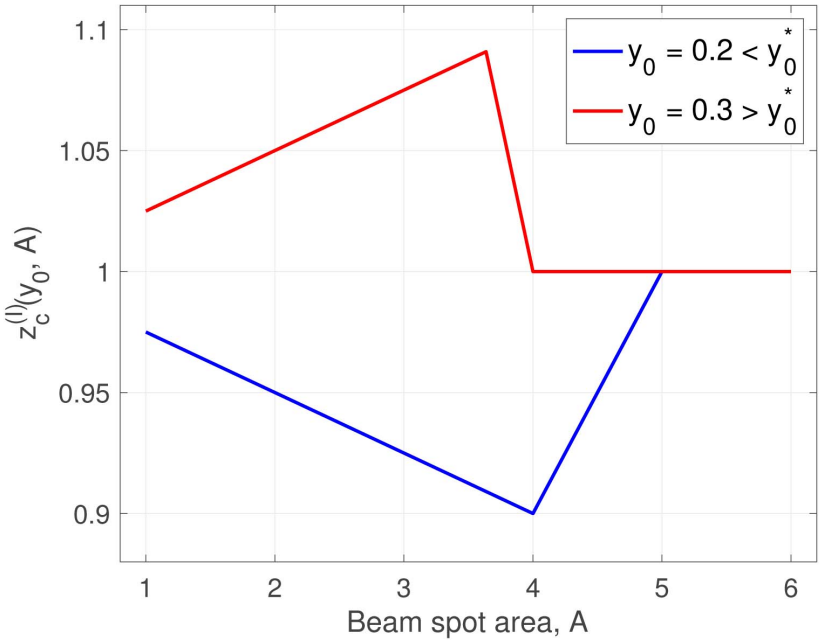

Figure 15. $z_c^{(I)}(y_0, A)$ vs A, respectively for $y_0 < y_0^* = 0.25$ and for $y_0 > y_0^*$. Here $z_c^{(I)}(y_0, A)$ is the intersection of $T_{\text{act}}(z_c; y_0, A)$ and $T_{\text{act}}(z_c; y_0, \infty)$ from **Figure 14**.

trial density in calculating the constraint function. The goal is to use the resulting constraint function as a tool to probe the underlying unknown density type.

Let $T_{\text{act,uni}}(z_c; A)$ denote the constraint function based on the test data (which is generated using type 4 density (55) with true value y_0^*) and calculated using framework (63) with the *uniform trial density* $\rho(y)/\rho_0 \equiv 1$. For type 4 parametric family (55), the uniform density is a special case with large y_0.

It follows that the behavior of $T_{\text{act,uni}}(z_c; A)$ is the same as that of $T_{\text{act}}(z_c; y_0, A)$ for large y_0, which we analyzed in the previous subsection.

Let $z_{c,\text{uni}}^{(I)}(A)$ denote the intersection of the pair $T_{\text{act,uni}}(z_c; A)$ and $T_{\text{act,uni}}(z_c; \infty) \equiv T_{\text{act}}^*$. Intersection $z_{c,\text{uni}}^{(I)}(A)$ has the same behavior as $z_c^{(I)}(y_0, A)$ for large y_0. Based on result (69) for $z_c^{(I)}(y_0, A)$ in the previous subsection, we conclude for $z_{c,\text{uni}}^{(I)}(A)$ that

$$z_{c,\text{uni}}^{(I)}(A) = \begin{cases} z_c^* + \left(z_c^* - A y_0^*\right) & \text{for } A < \dfrac{z_c^*}{y_0^*} \\ z_c^* & \text{for } A > \dfrac{z_c^*}{y_0^*} \end{cases} \tag{70}$$

Result (70) predicts that when the true underlying density is type 4 given in (55), $z_{c,\text{uni}}^{(I)}(A)$ starts at slightly below $2z_c^*$ for small A; decreases linearly toward z_c^* as A increases; arrives at z_c^* at $A = \dfrac{z_c^*}{y_0^*}$ and stays there for $A > \dfrac{z_c^*}{y_0^*}$. The qualitative behavior of $z_{c,\text{uni}}^{(I)}(A)$ converging to z_c^* for large A is similar for type 1 and type 4 densities. **Figure 16** compares simulated $z_{c,\text{uni}}^{(I)}(A)$ and $z_c^{(I)}(y_0, A)$. The simulation results confirm the theoretical prediction.

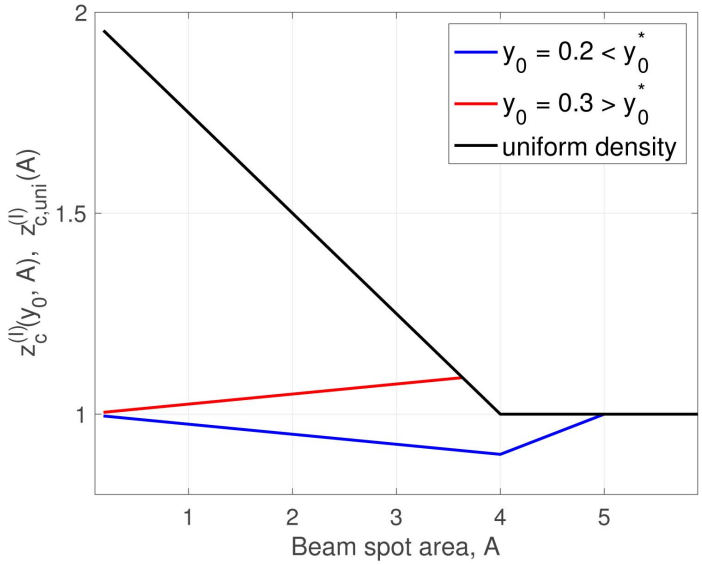

Figure 16. Simulated results of $z_{c,\mathrm{uni}}^{(I)}(A)$ for type 4 density given in (55). Here $z_{c,\mathrm{uni}}^{(I)}(A)$ is based on the data from the true density (with $y_0^* = 0.25$) but is calculated using the uniform trial density.

9. Summary

In this study, we investigate the nociceptor density of the form: $\rho(y) = \rho_0 f(\beta y)$, and its effect on heat-induced withdrawal reflex. We examine 4 types of $f(s)$ illustrated in **Figure 17**. Each $f(s)$ shown has a characteristic length 1. When scaled in the depth direction by parameter β, each $f(s)$ yields a family of density profiles.

We consider the situation where the reflex time and the temperature profile at the reflex are measurable in tests. We build the mathematical formulation for extracting 3 key parameters from test data:

- the activation temperature T_{act} for heat-sensitive nociceptors,
- the critical threshold z_c on the equivalent activated volume, and
- the parameter β in the relative density.

Our general strategy is to identify distinct behaviors for different densitytypes and distinct behaviors for different regions of parameter values. We compare these theoretical patterns with the observed patterns from test data to pinpoint the underlying unknown density type. We inspect the behavior calculated using a trial parameter value in the parametric form to determine whether the trial value is below or above the true value. Then we use that information to tune the trial value up or down accordingly toward the true value. The process is repeated with the new trial value until convergence. To best illustrate each key module individually in its own setting, we divide the task of finding the density type and the parameter value into stages and consider several problems. Mathematically, we proceed from the simplest problem to the realistic one in which both the density type and the parameter value are unknown. The solution of a simpler problem provides the building blocks for solving a more complicated problem.

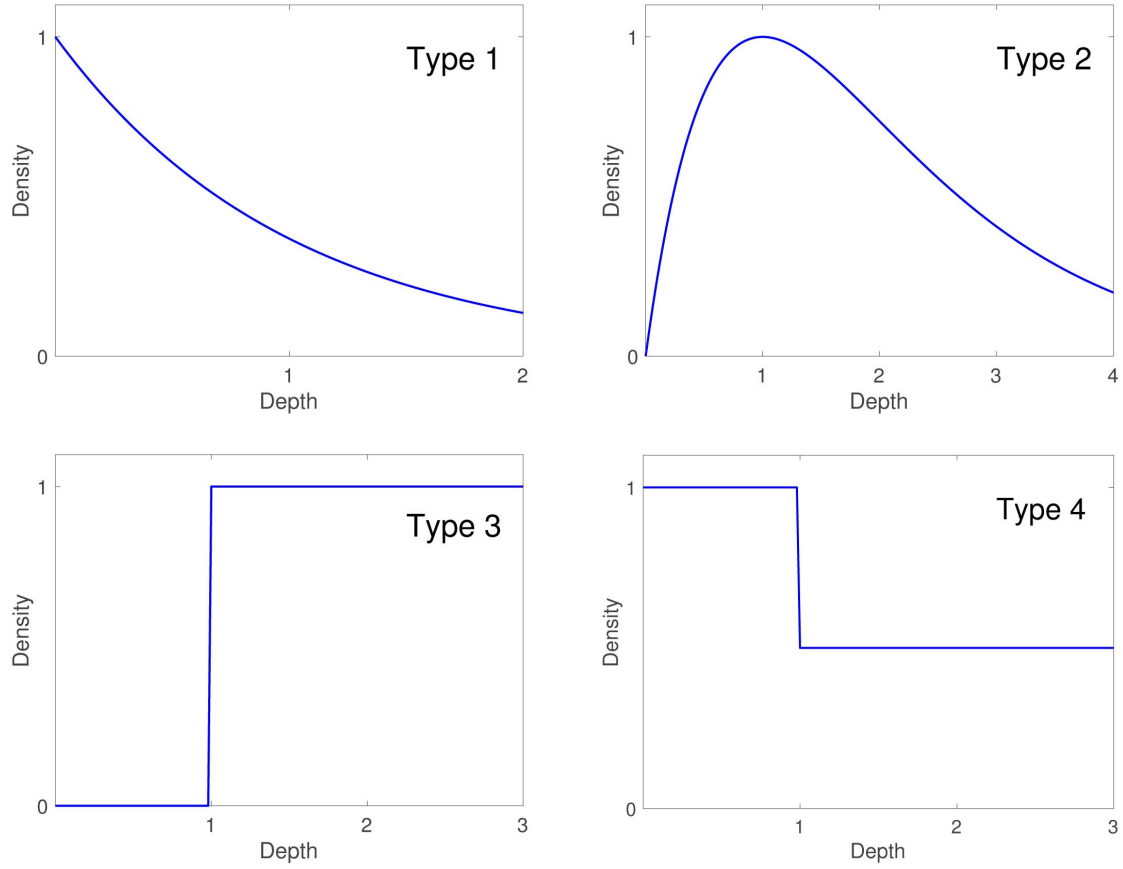

Figure 17. Four types of nociceptor density vs. depth. Each type has been transformed into the standard form of maximum density 1 and characteristic depth 1.

Problem 1:

When both the density type $f(s)$ and the true scaling parameter β^* are known for the nociceptor density, the test data allow us to construct true constraint functions on (z_c, T_{act}). Multiple constraint functions, obtained from tests at different values of beam spot area A, share a common point at the true value of (z_c, T_{act}). Parameters z_c and T_{act} are determined by finding the intersection of these distinct constraint functions.

Problem 2:

When the density type $f(s)$ is given but the true scaling parameter β^* is unknown, we construct trial constraint functions using trial values of β. Let $T_{\text{act}}(z_c; \beta, A)$ denote the trial constraint function that is based on the measured data (which is generated with true value β^*) and that is calculated using the given parametric form with trial value β. When the trial value β is different from the true value β^*, in general, the true value $(z_c^*, T_{\text{act}}^*)$ is not on trial constraint functions, and trial constraint functions at different values of beam spot area A do not share a common intersection. The behaviors of trial constraint functions $T_{\text{act}}(z_c; \beta, A)$ are demonstrated for the 4 density types, respectively in Figure 2, Figure 6, Figure 10, and Figure 14. We look at the intersection of a pair of trial constraint functions: $T_{\text{act}}(z_c; \beta, A)$ and $T_{\text{act}}(z_c; \beta, \infty)$. Let

$z_c^{(I)}(\beta, A)$ denote the intersection of the pair, which is affected by the trial value β used in calculating the trial constraint functions and by the beam spot area A used in tests. Given a trial value β, we examine the trend of $z_c^{(I)}(\beta, A)$ vs A. For each of the 4 density types, as the beam spot area A increases, $z_c^{(I)}(\beta, A)$ vs A demonstrates distinct trend of increasing or decreasing, respectively when $\beta > \beta^*$ and when $\beta < \beta^*$. The trend of $z_c^{(I)}(\beta, A)$ vs. A is illustrated for the 4 density types, respectively in Figure 3, Figure 7, Figure 11, and Figure 15. Depending on the given density type and the observed trend of $z_c^{(I)}(\beta, A)$ vs. A, we tune the trial value β accordingly to approach the true value β^*. At the true value β^*, $z_c^{(I)}(\beta^*, A) \equiv z_c^*$ is independent of A. Once we arrive at the true value β^*, the subsequent procedure of finding parameters z_c and T_{act} is the same as described in Problem 1 above: the intersection of $T_{\text{act}}(z_c; \beta^*, A)$ and $T_{\text{act}}(z_c; \beta^*, \infty)$ gives us the true value of (z_c, T_{act}).

Problem 3:

When both the density type $f(s)$ and the true scaling parameter β^* are unknown, we construct trial constraint functions using the uniform trial density $\rho(y)/\rho_0 \equiv 1$, which is parameter-free. The trial constraint function using the uniform density is denoted by $T_{\text{act,uni}}(z_c; A)$. When the true density is not the uniform density, the true value $(z_c^*, T_{\text{act}}^*)$ is not on trial constraint function $T_{\text{act,uni}}(z_c; A)$, and for different values of A trial constraint functions $T_{\text{act,uni}}(z_c; A)$ do not share a common point. Similar to what we did on trial constraint functions $T_{\text{act}}(z_c; \beta, A)$ in Problem 2 (where the density type is given), here we look at the intersection of a pair of trial constraint functions: $T_{\text{act,uni}}(z_c; A)$ and $T_{\text{act,uni}}(z_c; \infty)$. Let $z_{c,\text{uni}}^{(I)}(A)$ denote the intersection of the pair, which is affected only by the beam spot area A used in tests. Given a collection of measured data sets at several values of A, we examine the trend of $z_{c,\text{uni}}^{(I)}(A)$ vs. A. The trend behavior of $z_{c,\text{uni}}^{(I)}(A)$ vs. A is displayed for the 4 density types, respectively in Figure 4, Figure 8, Figure 12, and Figure 16. The behaviors of $z_{c,\text{uni}}^{(I)}(A)$ vs. A for types 1 and 4 are distinct from each other and are distinct from those for types 2 and 3. In addition to examining the trend of $z_{c,\text{uni}}^{(I)}(A)$ vs. A, we also check the convergence pattern of reflex time t_{ref} as beam spot area A increases, which is shown for the 4 density types, respectively in Figure 1, Figure 5, Figure 9, and Figure 13. Again, the patterns of t_{ref} vs. A for types 1 and 4 are distinct from each other and are distinct from those for types 2 and 3. Density types 2 and 3 have similar behaviors in both $z_{c,\text{uni}}^{(I)}(A)$ vs. A and t_{ref} vs. A. This is not completely surprising since both density types share the common feature of having zero nociceptor density at the skin surface. When we are presented with the task of identifying the underlying nociceptor density from among the 4 density types, it is still a challenge to distinguish between type 2 and type 3 based on the trend of $z_{c,\text{uni}}^{(I)}(A)$ vs. A or the trend of t_{ref} vs. A. We need to explore other formulations and analytical tools for differentiating types 2 and 3. One possibility is to use alternative standardized parameter-free forms other than the uniform density as the trial density in calculating the trial constraint function. Another possibility is to use the trend of system behaviors vs. varying

applied beam power, in addition to varying beam spot area. Once the density type is selected, the remaining task of determining the true values of parameters β and (z_c, T_{act}) is the same as described in Problem 2 above.

The goal of our study is to develop a methodology that utilizes test data to 1) identify the density type for the underlying nociceptor density, 2) find by trial and error the true scaling parameter in the parametric form, and 3) determine the activation temperature of nociceptors and the critical threshold on the equivalent activated volume. The results of 1) and 2) basically specify the nociceptor density profile vs depth. We assume the test data available include measurements of the reflex time and of the spatial temperature profile at reflex. Combining the procedures outlined in Problems 1, 2 and 3 above, we obtain such a methodology exactly for this purpose.

Disclaimer

The authors thank Dr. John Biddle and Dr. Stacy Teng of Institute for Defense Analyses for introducing the ADT CHEETEH-E model and for many helpful discussions. The authors acknowledge the Joint Intermediate Force Capabilities Office of U.S. Department of Defense and the Naval Postgraduate School for supporting this work. The views expressed in this document are those of the authors and do not reflect the official policy or position of the Department of Defense or the U.S. Government.

Conflicts of Interest

The authors declare no conflicts of interest regarding the publication of this paper.

References

[1] Gandhi, O.P. and Riazi, A. (1986) Absorption of Millimeter Waves by Human Beings and Its Biological Implications. *IEEE Transactions on Microwave Theory and Techniques*, **34**, 228-235. https://doi.org/10.1109/TMTT.1986.1133316

[2] Romanenko, S., Begley, R., Harvey, A.R., Hool, L. and Wallace, V.P. (2017) The Interaction between Electromagnetic Fields at Megahertz, Gigahertz and Terahertz Frequencies with Cells, Tissues and Organisms: Risks and Potential. *Journal of The Royal Society Interface*, **14**, Article ID: 20170585. https://doi.org/10.1098/rsif.2017.0585

[3] Zhadobov, M., Chahat, N., Sauleau, R., Le Quement, C. and Le Drean, Y. (2011) Millimeter-Wave Interactions with the Human Body: State of Knowledge and Recent Advances. *International Journal of Microwave and Wireless Technologies*, **3**, 237-247. https://doi.org/10.1017/S1759078711000122

[4] Foster, K.R., Ziskin, M.C. and Balzano, Q. (2016) Thermal Response of Human Skin to Microwave Energy: A Critical Review. *Health Physics*, **111**, 528-541. https://doi.org/10.1097/HP.0000000000000571

[5] Ozen, S., Helhel, S. and Bilgin, S. (2011) Temperature and Burn Injury Prediction of Human Skin Exposed to Microwaves: A Model Analysis. *Radiation and Environmental Biophysics*, **50**, 483-489. https://doi.org/10.1007/s00411-011-0364-y

[6] Nelson, D.A., Nelson, M.T., Walters, T.J. and Mason, P.A. (2000) Skin Heating Effects of Millimeter-Wave Irradiation—Thermal Modeling Results. *IEEE Transactions on Microwave Theory and Techniques*, **48**, 2111-2120. https://doi.org/10.1109/22.884202

[7] Laakso, I., Morimoto, R., Heinonen, J., Jokela, K. and Hirata, A. (2017) Human Exposure to Pulsed Fields in the Frequency Range from 6 to 100 GHz. *Physics in Medicine & Biology*, **62**, 6980-6992. https://doi.org/10.1088/1361-6560/aa81fe

[8] Durney, C.H., Massoudi, H. and Iskander, M.F. (1986) Radiofrequency Radiation Dosimetry Handbook. 4th Edition, Brooks AFB, TX: USAF School Aerospace Med.

[9] Xu, F. and Lu, T. (2011) Introduction to Skin Biothermomechanics and Thermal Pain. Springer, New York. https://doi.org/10.1007/978-3-642-13202-5

[10] Gabriel, S., Lau, R.W. and Gabriel, C. (1996) The Dielectric Properties of Biological Tissues: II Measurements in the Frequency Range 10 Hz to 20 GHz. *Physics in Medicine and Biology*, **41**, 2251-2269. https://doi.org/10.1088/0031-9155/41/11/002

[11] Hwang, H., Yim, J., Cho, J.-W., Cheon, C. and Kwon, Y. (2003) 110 GHz Broadband Measurement of Permittivity on Human Epidermis Using 1 mm Coaxial Probe. *International Microwave Symposium Digest*, **1**, 399-402.

[12] Romanenko, S., Harvey, A.R., Hool, L., Fan, S. and Wallace, V.P. (2019) Millimeter Wave Radiation Activates Leech Nociceptors via TRPV1-Like Receptor Sensitization. *Biophysical Journal*, **116**, 2331-2345. https://doi.org/10.1016/j.bpj.2019.04.021

[13] Walters, T.J., Blick, D.W., Johnson, L.R., Adair, E.R. and Foster, K.R. (2000) Heating and Pain Sensation Produced in Human Skin by Millimeter Waves: Comparison to a Simple Thermal Model. *Health Physics*, **78**, 259-267. https://doi.org/10.1097/00004032-200003000-00003

[14] Plaghki, L., Decruynaere, C., Van Dooren, P. and Le Bars, D. (2010) The Fine Tuning of Pain Thresholds: A Sophisticated Double Alarm System. *PLoS ONE*, **5**, e10269. https://doi.org/10.1371/journal.pone.0010269

[15] Parker, J.E., Nelson, E.J., Beason, C.W. and Cook, M.C. (2017) Thermal and Behavioral Effects of Exposure to 30Kw, 95-GHz Millimeter Wave Energy. Technical Report, AFRL-RH-FS-TR-2017-0016.

[16] Parker, J.E., Nelson, E.J., Beason, C.W. and Cook, M.C. (2017) Effects of Variable Spot Size on Human Exposure to 95-GHz Millimeter Wave Energy. Technical Report, AFRL-RH-FS-TQ-2017-0017.

[17] Wang, H., Burgei, W.A. and Zhou, H. (2020) A Concise Model and Analysis for Heat-Induced Withdrawal Reflex Caused by Millimeter Wave Radiation. *American Journal of Operations Research*, **10**, 31-81. https://doi.org/10.4236/ajor.2020.102004

Appendix A

Derivation of $\lim_{A\to\infty} T_{\text{act}}\left(z_c;\beta,A\right)=T_{\text{act}}^{*}$ in (25)

We show the convergence in three steps.

Step 1: We first look at the factor $\left(F^{-1}\right)'(\varepsilon)\frac{1}{A}$ in the expression of $\left.\frac{\partial T_{\text{act}}}{\partial z_c}\right|_{\left(z_c^{*},\beta^{*}\right)}$ in (22). As $A\to\infty$ we have $\varepsilon\to 0$. We expand $\left(F^{-1}\right)'(\varepsilon)$ as $\varepsilon\to 0$. In both cases 1 and 2, we have $\lim_{\varepsilon\to 0}\left(F^{-1}\right)'(\varepsilon)\cdot\varepsilon=0$. It follows that

$$\lim_{A\to\infty}\left(F^{-1}\right)'(\varepsilon)\frac{1}{A}=\lim_{\varepsilon\to 0}\left(F^{-1}\right)'(\varepsilon)\cdot\varepsilon\frac{1}{\beta z_c}=0 \tag{71}$$

Step 2: Next we look at the factor $\frac{\partial}{\partial y}\Phi(\xi;1/A)$ in the expression of $\left.\frac{\partial T_{\text{act}}}{\partial z_c}\right|_{\left(z_c^{*},\beta^{*}\right)}$ in (22). With $\lim_{A\to\infty}\xi=0$ and the insulated boundary condition $\frac{\partial T(0,t)}{\partial y}=0$, we have

$$\lim_{A\to\infty}\frac{\partial}{\partial y}\Phi\left(\xi;\frac{1}{A}\right)=\lim_{\varepsilon\to 0}\frac{\partial}{\partial y}T\left(\xi,t_{\text{ref}}\left(A\right)\right)=0 \tag{72}$$

Taking the limit as $A\to\infty$ in (22), and using results (71) and (72), we conclude

$$\lim_{A\to\infty}\frac{\partial T_{\text{act}}}{\partial z_c}=\lim_{A\to\infty}\frac{\partial}{\partial y}\Phi\left(\xi;\frac{1}{A}\right)\left(F^{-1}\right)'(\varepsilon)\frac{1}{A}=0$$

Step 3: We show that the term $\eta\left|_{\left(z_c^{*},\beta^{*}\right)}\right.$ in (24) is bounded as $A\to\infty$. In the expression of η in (23), we look at $\frac{F^{-1}(\varepsilon)}{\varepsilon\left(F^{-1}\right)'(\varepsilon)}$, the component that varies with ε. Using expansions (8) and (9) in case 1 or expansions (10) and (11) in case 2, we get

$$\frac{F^{-1}(\varepsilon)}{\varepsilon\left(F^{-1}\right)'(\varepsilon)}=\begin{cases}1+\dfrac{a_1}{2a_0^2}\varepsilon+\cdots & \text{for case 1}\\ 2+\dfrac{\sqrt{2}a_2}{3a_1^{3/2}}\varepsilon^{1/2}+\cdots & \text{for case 2}\end{cases} \tag{73}$$

In both cases, we have $\lim_{\varepsilon\to 0}\eta=\text{finite}$.

Combining the results of three steps above, we conclude that for any trial value β, as $A\to\infty$, the constraint function converges to T_{act}^{*}, as described in (25) in the main text.

Appendix B

Derivation of property (53)

Property (53) describes coefficients in the expansion of $\frac{\partial}{\partial y}\Phi\left(\frac{z_c^{*}}{A}+y_0^{*};\frac{1}{A}\right)$ with respect to $1/A$. Recall that $\Phi(y;v)\equiv T\left(y,t_{\text{ref}}\left(1/v\right)\right)$ where $v\equiv 1/A$.

Function $T(y,t)$ as given in (12) and (13), has the properties below

1) $\frac{\partial}{\partial y}T(y,t)$ is always negative.

2) At any given depth *y*, the absolute value of $\frac{\partial}{\partial y}T(y,t)$ increases with time *t*.

3) At any given time *t*, the absolute value of $\frac{\partial}{\partial y}T(y,t)$ start with 0 value at $y=0$, increases with *y* until the inflection point at $y=\kappa(t)$, and then decreases to zeros beyond the inflection point. The depth of inflection point $y=\kappa(t)$ increases with *t*.

We consider the situation of $y_0^* < \kappa(t_0)$. That is, the nociceptor density jump occurs before the inflection point of temperature profile at reflex. Combining properties 1 and 3 of $T(y,t)$ with $y_0^* < \kappa(t_0)$, we have

$$\underbrace{-\frac{\partial}{\partial y}T\left(\frac{z_c^*}{A}+y_0^*, t_{\text{ref}}(A)\right)}_{\text{positive}} > \underbrace{-\frac{\partial}{\partial y}T\left(y_0^*, t_{\text{ref}}(A)\right)}_{\text{positive}} \quad \text{for all } A \tag{74}$$

As beam spot area *A* increases $t_{\text{ref}}(A)$ decreases and is bounded from below by $t_{\text{ref}}(A) \geq t_{\text{ref}}(A=\infty) = \tau_0(\mu y_0^*)$. In turn, $\tau_0(\mu y_0^*)$ is bounded by $\tau_0(\mu y_0^*) \geq \tau_0(0) = t_0 > 0$, reflecting that the presence of a skin layer with no nociceptor delays the occurrence of withdrawal reflex. Thus, we have

$$t_{\text{ref}}(A) \geq t_{\text{ref}}(A=\infty) \geq t_0 > 0 \quad \text{independent of } A \text{ and } y_0^*$$

Applying property 2 of $T(y,t)$ to (74) with $t_{\text{ref}}(A) \geq t_{\text{ref}}(A=\infty)$, we obtain

$$-\frac{\partial}{\partial y}\Phi\left(\frac{z_c^*}{A}+y_0^*; \frac{1}{A}\right) > -\frac{\partial}{\partial y}\Phi\left(y_0^*; 0\right) > 0 \tag{75}$$

The first part of (53), $b_1 > 0$, follows from inequality (75) and definition of b_1 in (51). The second part of (53), $\left(b_1^2 - b_2\right) > 0$, is verified in simulations.

Scientific Research Publishing

Applied Mathematics, 2020, 11, 825-844
https://www.scirp.org/journal/am
ISSN Online: 2152-7393
ISSN Print: 2152-7385

Development of an Effective System for Selecting Construction Materials for Sustainable Residential Housing in Western Australia

Muhammad Rashid Minhas, Vidyasagar Potdar

School of Management, Curtin University, Perth, Australia
Email: muhammad.minhas@postgrad.curtin.edu.au, v.potdar@curtin.edu.au

How to cite this paper: Minhas, M.R. and Potdar, V. (2020) Development of an Effective System for Selecting Construction Materials for Sustainable Residential Housing in Western Australia. *Applied Mathematics*, **11**, 825-844.
https://doi.org/10.4236/am.2020.118054

Received: July 19, 2020
Accepted: August 28, 2020
Published: August 31, 2020

Abstract

Urbanization and living comfort have revolutionized the construction industry. Many techniques and strategies have been used to improve the overall efficiency of construction and to reduce waste during and after the construction activity; some are cost effective and some not. Sustainable construction strategies have addressed these issues by proposing relatively more cost effective and environment-saving solutions. One strategy is to select sustainable construction materials at the building design stage. This article involved a questionnaire survey to collect data about local technical stakeholders' (architects, designers, engineers, estimators, and managers) awareness of environmental sustainability and current practices for selecting construction materials. A sustainability index (SI) was developed using SPSS (Statistical Package for the Social Sciences) for the complex statistical analysis. These data were used to develop a decision support system (DSS) using the multi-criteria decision making (MCDM) technique, the TOPSIS. The support system was validated by applying it to sustainable roof products in a pilot case study—these materials are frequently used in local markets for residential construction in West Australia. So the main objective was to get insight to local market trends and features involved in construction materials selection. Data analysis was carried out to develop a decision support system to help technical stakeholders in construction materials selection process.

Keywords

Construction Industry, Sustainability Index (SI), Multi-Criteria Decision Making (MCDM), Decision Support System (DSS), TOPSIS

1. Introduction

In the past the global construction industry has developed rapidly in terms of advanced technology and the incorporation of safety and sustainability. Similarly, the Australian construction industry now considers sustainability as a vital factor for maintaining a balance in preservation and consumption of natural resources. To investigate the local trends and general procedures in the selection process for materials in residential building construction, a questionnaire survey was developed and circulated among the leading construction companies in Western Australia.

Survey response rate and validity: Data were collected in three survey formats: postal, online, and self-administered surveys. A total number of 52 survey questionnaires were sent to construction companies with a cover letter and a form for participant consent. From these, 11 responses were received (response rate = 21.15%; Figure 1). This response rate was considered adequate because other researchers in the construction industry also reported response rates for postal surveys between 20% and 30% [1] [2] [3].

For the online surveys, 35 company representatives were sent a uniform resource locator (URL) link to access the survey and record their responses. The response rate was 48.57% (17 responses). Face-to-face, self-administered surveys were also conducted with 7 company representatives (23 companies sent request; 30.43% response rate). This method of data collection is considered the best; complete responses are received through this method. All survey responses were evaluated before analysis to verify that all questions were answered; missing values were adjusted in the analysis with SPSS (Statistical Package for the Social Sciences, (version 24)). Some irrational responses and suggestions were received but most responses were relevant based upon the work experience of the respondents.

We used a Likert scale in our survey, which is considered reliable to investigate the overall perceptions and experiences of a group of relatively homogeneous

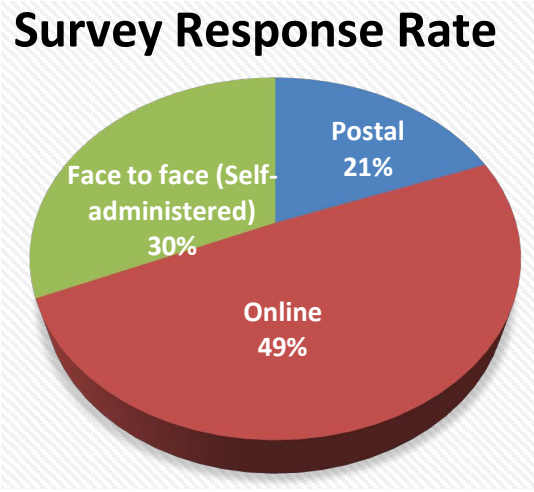

Figure 1. Survey response rate.

individuals of similar backgrounds and trades [4]. Using a multi-criteria decision making (MCDM) technique, we processed the data to develop a sustainability index (SI) for ranking the most appropriate and sustainable building construction materials. The system was validated by running a pilot analysis on local sustainable roofing materials from two major material suppliers.

Margin of error: For an inferential statistical analysis, researchers agree a sample size (n) of more than 30 is required to obtain an accurate value [5] [6] [7] [8]. Prior research validated that minimum threshold value to rank a data acceptable is 30. We got the response from more than 30 construction firms, hence our sample size ($n = 36$) is acceptable for statistical analysis with the appropriate analysis tool to get acceptable and reliable results.

2. Statistical Data Analysis

SPSS (Statistical Package for the Social Sciences, version 24) was used to analyze the data. Frequencies, percentages, averages were calculated. All values are used for open-ended questions. Data were collected on the organization profiles (*i.e.* type, size, and age of organization; area of building projects, focus, and main client type) to obtain overall snapshots of the organizations.

2.1. Level of Awareness of Environmental Issues

All company representatives and technical stakeholders were somewhat aware of environmental parameters, but only 33.34% of the 36 were extremely aware. Almost 20% were only slightly aware; most of these respondents had a trade background, with no higher education degree in construction (Table 1).

Considering environmental issues at the conceptual design stage

A large body of literature describes the importance of addressing environmental issues at the first step in the construction process, the conceptual design stage [9] [10]. To investigate the degree of agreement or disagreement regarding this practice, respondents were asked "Is it important to consider the environmental issues at the conceptual stages?" A seven-point Likert scale recorded their viewpoint (1 = *Strongly disagree*, 7 = *Strongly agree*); the extended Likert scale was used to canvass the full spectrum of opinions and current general practice in the local market (Table 2).

Table 1. Level of awareness of environmental issues in building construction.

Awareness scale	Frequency	Percent	Cumulative percent
Extremely aware	12	33.34	33.34
Moderately aware	8	22.23	55.57
Somewhat aware	9	25.0	80.57
Slightly aware	7	19.45	100.0
Total		100.0	

Source: Analysis of survey data (2018).

Table 2. Consideration of environmental issues at conceptual design stage.

Agreement scale	Frequency	Percent	Cumulative percent
Strongly disagree	0	0	0
Disagree	0	0	0
Somewhat disagree	0	0	0
Neutral	3	8.33	8.33
Somewhat agree	6	16.66	24.99
Agree	15	41.66	66.65
Strongly agree	12	33.33	100
Total		100	

Source: Analysis of survey data (2018).

Table 2 shows that most (about 75%) of the respondents (75%) agreed or strongly agreed that the best time to consider environmental or and sustainability issues is at the conceptual stage. Other researchers report similar findings as well [11]. Considering all these environmental and sustainability issues at the start of the process allows us to change our design accordingly, and the capital cost can be well managed and minimized.

2.2. Building Design Priorities

The analysis showed that the decision makers were aware of the importance of using environmentally friendly and sustainable construction materials. The respondents were asked to prioritize their objectives to gauge the level of importance they assigned to project objectives, including environmental impacts and sustainable construction materials (Table 3).

The following formula was used to calculate the values in Table 3:

$$\mathrm{RI} = \sum \frac{w}{A \times N} \tag{a}$$

where RI = relative index, w = weighting given by respondents (range 1 - 7), A = highest weight (*i.e.* 7), N = total number of respondents. The value of the relative index ranges from 0 to 1.

The respondents' highest priority was to satisfy the client's specifications (Table 3), which indicates that most of the time efforts are made to reduce the cost as well.

3. Sustainability Considerations

The implementation of sustainability depends upon the knowledge and awareness of technical stakeholders (e.g. architects, designers, engineers, estimators, and managers).

Although the respondents stated they were aware of sustainability and its importance in construction, 52.77% had only an average knowledge of the sustainable products available in the market. Moreover, the proportion of respondents

Table 3. Ranking of project objectives.

Project Objective	Weighted total	RI	Rank	Mean Value
Satisfy Client Specifications	140	0.778	1	3.889
Meet Project Deadline	134	0.744	2	3.722
Meet Building Regulation	134	0.744	3	3.722
Sustainability Criteria	130	0.722	4	3.611
Environmental Impacts	126	0.700	5	3.500
Minimize the Cost	125	0.694	6	3.472

Source: Analysis of survey data 2018.

with poor knowledge (22.22%) exceeded the proportion with good knowledge (16.66%) (Table 4). Hence, the major stakeholders need to learn about sustainable products and their efficacy and adaptability. Most respondents thought that clients or their representatives are less concerned about this factor than about other considerations, and so they pay less attention to this issue. The small percentage of respondents with excellent knowledge (8.33%) all belonged to well-established, large organizations.

3.1. Sustainability Assessment

In contrast, most respondents (88.88%) agreed that it is important to select sustainable materials for building construction (Table 5); only one respondent (2.77%) provided any reasons for not doing so (cost and lack of skilled labor).

Despite the respondents' prior claim of knowing about sustainability and its importance, the analysis showed that the percentage of their projects in which sustainability was considered important was low (Table 6).

A majority of respondents (36%) completed projects without considering sustainability as an important factor for building construction, although implementing sustainability activities can give competitive advantage over rival firms that are reluctant to implement those activities [12].

3.2. Constraints in Selecting Sustainable Materials

The building industry uses large quantities of raw materials and energy in all stages from construction to operation. This means choosing materials with high content in embodied energy involve in high energy demand at construction stage and vice versa in operational phase [13] [14].

To gauge the real-world problems or obstacles faced by the technical stakeholders in selecting sustainable materials, respondents were asked to rank such issues on a 5-point Likert scale (1, *low*; 5, *high*). The degree of agreement, calculated as Kendall's W, was 0.248 (Table 7). This value indicates that almost all of the technical stakeholders face the same obstacles, with some exceptions.

The degree of agreement is calculated Kendall's W = 0.248 which shows almost all technical stakeholders are facing the same obstacles with some exceptions.

Table 4. Knowledge of sustainable design.

Knowledge Scale	Frequency	Percent	Valid Percent	Cumulative Percent
Excellent	3	8.33	8.33	8.33
Good	6	16.66	16.66	25
Average	19	52.77	52.77	77.76
Poor	8	22.22	22.22	100
Total		100	100	

Source: Analysis of survey data 2018.

Table 5. Importance of sustainable materials in building development.

Knowledge scale	Frequency	Percent	Valid Percent	Cumulative percent
Yes	32	88.88	88.88	88.88
No	3	8.33	8.33	97.21
If no, give reason	1	2.77	2.77	100
Total		100	100	

Source: Analysis of survey data (2018).

Table 6. Projects considering sustainability important.

Projects	Frequency	Percent	Cumulative Percent
<10%	13	36.11	36.11
10% - 20%	10	27.77	63.88
21% - 30%	5	13.88	77.76
31% - 40%	2	5.55	83.31
41% - 50%	4	11.11	94.42
>50%	2	5.55	100
Total		100	

Source: Analysis of survey data (2018).

Table 7. Constraints in sustainable material selection.

Stakeholder influence	RI[a]	Rank
Lack of information	0.73	2
Uncertainty in liability of work	0.67	7
Maintenance concern	0.73	3
Building code regulations	0.65	6
Lack of tools and data	0.70	5
Perception of extra cost being incurred	0.76	1
Perception of extra time being incurred	0.72	5
Perception that sustainable materials are low in quality	0.45	11
Aesthetically less pleasing	0.55	10

Continued

Project will be delayed	0.67	9
Limited suppliers	0.68	6
Low flexibility in alternatives	0.65	5
Unwilling to adopt the change	0.66	6
Kendall's W	(0.248)	

[a]Relative index. Source: Analysis of survey data (2018).

4. Development of Criteria for Sustainable Material Selection

The gap between information and implementation can be reduced by developing systems and IT features that are easy to use. This is a combined responsibility of all sectors involved in the construction industry. It is a mutual responsibility of government and the private sector to introduce and implement regulations for a "greener" and safer environment for future generations (Raynsford, 2000).

The criteria for sustainable material selection that were investigated were divided into three categories: environmental criteria, socio-economic criteria, and technical criteria (Table 8).

The respondents were asked to rank the sub-criteria for importance and the data were analyzed (Table 9).

Aesthetics was ranked first in the socio-economic category (RI = 0.88; Table 9). This criterion was designated as high importance as per our predefined values: all factors with an RI > 0.8 were considered of high importance and those with an RI < 0.8 considered of medium to high importance.

A decision model will help technical stakeholders to select from a wide range of options, either classical or innovative. We used the above sustainability criteria for computational analysis in order to formulate the best combination of alternative construction materials. Six major criteria were used (Figure 2). These 6 criteria were further divided into 23 sub-criteria (Table 10).

5. TOPSIS-Based Approach for Prioritized Aggregation

An aggregated MCDM environment means combining the values of a set of attributes to represent a single value for the entire set of attributes. Much work has been done to introduce the prioritization in aggregation method using the TOPSIS. The derivation of our MCDM model using this prioritization approach is described below.

A sustainability index framework basically helps the decision makers to integrate the issues of sustainability while selecting the available construction materials. Selecting sustainable construction materials from the pool of alternative sustainable materials is a time consuming and difficult practice. Applying the MCDM technique is the best method for integrating objective and subjective weights of various conflicting criteria in order to choose the most appropriate sustainable material. However, the process is challenging.

Table 8. Criteria for sustainable material selection for construction professionals.

Environmental criteria	Socio-economic criteria	Technical criteria
E1: Potential for reuse	S1: Disposal cost	T1: Maintainability
E2: Environmentally favorable disposal options	S2: Health and safety	T2: Buildability
E3: Air quality impacts	S3: Maintenance cost	T3: Resistance to decay
E4: Ozone depletion potential	S4: Aesthetics	T4: Fire resistance
E5: Environmental impact during manufacturing	S5: Use of local materials	T5: Life expectancy
E6: Less toxicity	S6: Capital cost	T6: Energy saving
E7: Regulatory compliance	S7: Skilled labor availability	
E8: Reduce pollution		
E9: Wastage in production		
E10: Raw materials extraction process		

Source: Analysis of survey data (2018).

Table 9. Ranking of criteria for sustainable material selection for construction professionals.

Performance criteria								Valid percentage
	Valid percentages of scores							
Environmental criteria	1	2	3	4	5	*RI*[a]	*Ranking*	*Importance*
E1: Potential for reuse	0.0	11.1	13.9	44.4	30.6	0.79	23	M-H[b]
E2: Environmentally favorable disposal options	2.8	8.3	27.8	30.6	30.6	0.72	17	M-H
E3: Air quality impacts	2.8	8.3	33.3	33.3	22.2	0.69	18	M-H
E4: Ozone depletion potential	5.6	8.3	41.7	16.7	27.8	0.76	15	M-H
E5: Environmental impact during manufacturing	2.8	13.9	33.3	19.4	30.6	0.67	13	M-H
E6: Less toxicity	2.8	11.1	30.6	25	30.6	0.86	7	H[c]
E7: Regulatory compliance	5.6	5.6	27.8	33.3	27.8	0.84	10	H
E8: Reduce pollution	0.0	5.6	19.4	50.0	25.0	0.85	5	H
E9: Wastage in production	4.4	15.4	31.9	37.4	11.0	0.79	20	M-H
E10: Raw materials extraction process	5.6	19.8	45.1	20.9	8.8	0.77	19	M-H
Socio-economic criteria								
S1: Disposal cost	2.8	8.3	16.7	44.4	27.8	0.78	21	M-H
S2: Health and safety	0.0	8.3	27.8	33.3	30.6	0.80	9	H
S3: Maintenance cost	0.0	5.6	22.2	38.9	33.3	0.81	8	H
S4: Aesthetics	0.0	5.6	36.1	36.1	22.2	0.88	1	H
S5: Use of local materials	0.0	8.3	33.3	41.7	16.7	0.76	16	M-H
S6: Capital cost	2.8	27.8	36.1	36.1	33.3	0.81	14	H
S7: Skilled labor availability	5.5	16.5	39.6	29.7	8.8	0.64	22	M-H
Technical criteria								
T1: Maintainability	0.0	5.6	27.8	44.4	22.2	0.86	2	H
T2: Buildability	0.0	0.0	9.9	53.8	36.3	0.85	6	H

Continued

T3: Resistance to decay	0.0	8.3	27.8	30.6	33.3	0.79	4	M-H
T4: Fire resistance	0.0	8.3	27.8	30.6	33.3	0.84	11	H
T5: Life expectancy	0.0	5.6	25.0	30.6	38.9	0.78	12	M-H
T6: Energy saving	0.0	2.8	38.9	30.6	27.8	0.84	3	H

[a]Relative index. [b]medium to high. [c]high. Source: Analysis of survey data (2018).

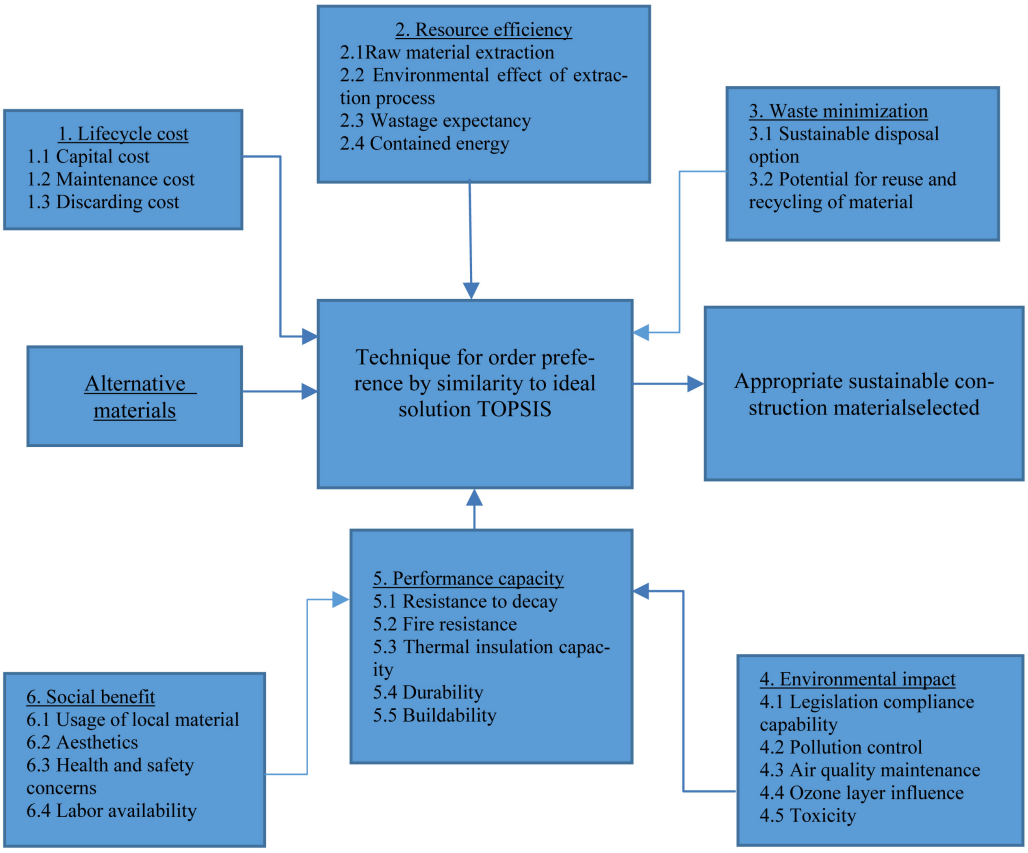

Figure 2. Conceptual framework for sustainable material selection.

The first step is to determine the most suitable aggregation method, usually from two major types: the crisp aggregation method, which is used to aggregate the real values; and the fuzzy aggregation method, which is used to aggregate the linguistic labels [15].

The second, most complicated, step is to define the boundary condition. The boundary condition compels the result of an aggregation function $f(x)$. The limit is defined as the minimal and maximal boundaries of possible output.

$$f(0,\cdots,0)=0 \quad \text{and} \quad f(1,\cdots,1)=1, \quad \text{where} \quad x\in[0,1] \tag{1}$$

The commutativity property states that ordering/ranking of arguments does not matter when there is equal importance or no relationship is considered among the different criteria.

$$f(x_1,x_2,\cdots,x_n)=f(x_2,x_1,\cdots,x_n)=f(x_n,x_2,x_1,\cdots), \quad x\in S \tag{2}$$

Table 10. Criteria and sub-criteria grouped with type.

Criteria	Sub-criteria	Description	Criteria & type
1. Life cycle cost	1.1 Capital cost	Initial purchasing cost of material	−C1
	1.2 Maintenance cost	Total repair cost during whole lifecycle of material	−C2
	1.3 Discarding cost	Demolition and disposal cost of material	−C3
2. Resource efficiency	2.1 Raw material extraction	Source of raw material	−C4
	2.2 Environmental effect of extraction process	Quantitative detrimental effects during the extraction	−C5
	2.3 Wastage expectancy	Probability of wastage during extraction	+C6
	2.4 Contained energy	Total amount of energy dedicated to providing the sustainable, renewable energy	+C7
3. Waste minimization	3.1 Sustainable disposal options	How favorable to create sustainable disposal options (e.g. carbon burial, incineration)	+C8
	3.2 Potential for reuse and recycling of material	Capacity for reuse and amount of total wastage during recycling	+C9
4. Environmental impact	4.1 Legislation compliance capability	Capability to comply with local and international legislation	+C10
	4.2 Pollution control	Overall ability to contribute to pollution control	+C11
	4.3 Air quality maintenance	Level of maintaining air quality using potential material	+C12
	4.4 Ozone layer influence	Level of impact to protect the ozone layer	+C13
	4.5 Toxicity	Level of generating the toxic materials (e.g. asbestos)	−C14
5. Performance capacity	5.1 Resistance to decay	Level of durability and sustainable age	+C15
	5.2 Fire resistance	Level of resistance against fire-related damage	+C16
	5.3 Thermal insulation capacity	Level of maintaining inner temperature of residential building	+C17
	5.4 Durability	Level of reliability and effective resistance again deterioration	+C18
	5.5 Buildability	Easiness of use and execution	+C19
6. Social benefit	6.1 Usage of local material	Local material usage, saving transportation cost and using local workforce	+C20
	6.2 Aesthetics	Level of visual attractiveness and comfort for use	+C21
	6.3 Health and safety concerns	Level of internal environmental and air pollution control	+C22
	6.4 Labor availability	Level of local skilled workforce	+C23

The continuity condition means that the aggregation function does not change markedly' if small changes were made to the attributes considered in the aggregation process.

$U_{x\in S}[0,1]^x \to [0,1]$ is a continuous aggregation function if:

$$f(x):[0,1]^x \to [0,1] \tag{3}$$

The monotonicity condition implies that aggregation functions are monotonic, that is, the aggregation function shows a "non-decreasing" relationship between the criteria and the aggregation maneuvers.

$$x_i' > x_i, \text{ then } f(x_i') > f(x_i) \text{ where } x \in S \tag{4}$$

The idem-potencies condition is an algebraic property that belongs to the binary operation and displays the relationship if:

$$f(x, x, \cdots, x) = x \text{ where } x \in S \tag{5}$$

The associativity condition is the ability of the aggregation function to retaliate against the choice of group, which should not influence the overall result of the aggregation process.

$$f\left(f\left(x_1, x_2, \cdots\right), x_n\right) = f\left(f\left(x_1, x_2\right), \cdots, x_n\right), \quad x \in S \quad [16] \tag{6}$$

Many applications require the evaluation of a set of criteria with prioritized relationships within the set in order to reach a conclusion. [17] [18] [19].

The TOPSIS is an approach that originates from the geometric concept of displaced ideal point, which means that the criterion under investigation must be situated between the positive (most favorable) and negative (least favorable) locations [20].

Determining the weights and criteria ranking: Previous studies have discussed many methods for criteria ranking and weight determination [21] [22] [23]. There are two primary methods. The "direct choice of weights" method directly assigns weights based on the opinions and consensus of a group of experts. The "weights determination from data" method derives the weights of criteria from the data available in the same domain for aggregation purposes. We used the first method to get our weighted data set.

6. Application and Validation of Sustainability Model

Considering the complexity of the data-collection process and the research output, we conducted an empirical inquiry using a real-world, practical scenario. We collected data on roofing materials that are specifically used in residential buildings in Western Australia and are available from the two major suppliers of roofing tiles.

This validation involved the application and evaluation of two suppliers with six tile options. This hypothetical case study was based on the roofing tiles from different suppliers and different options depending on the type of material selected for the test run and the type of structure implemented. Cost was one of the factors considered; however, the most important factors were the six main criteria and related sub-criteria (see Table 10). The details and physical characteristics of the materials are presented in Table 11.

This model analyzes and ranks the sustainable options by using mathematical

Table 11. Roofing tile options.

	Roof type	Building	Structural location	Roof tile size	Roof pitch
Option 1: **two alternatives, from two different suppliers**	Timber truss pitched roof	Residential	Treated timber trussed roof with anti-con underlay, batts insulation, & concrete interlocking tiles	418 mm × 260 mm	18 - 20 degrees
Option 2: **two alternatives, from two different suppliers**	Timber truss pitched roof	Residential	Treated timber trussed roof with anti-con underlay, batts insulation, & clay terracotta tiles	418 mm × 260 mm	18 - 20 degrees
Option 3: **two alternatives, from two different suppliers**	Timber truss pitched roof	Residential	Structurally insulated roofing panels with anti-con underlay & designer ceramic tiles	418 mm × 260 mm	18 - 20 degrees

implications with the MCDM technique. The data for this pilot study were collected as part of the survey questionnaire. The experts ranked the different alternatives from the suppliers based on the criteria and sub-criteria provided to them. These values were tabulated in an MS Excel™ spreadsheet and analyzed by running the TOPSIS model. The main factors that drive the selection of roofing materials are:

1) Compliance with Australian building codes and local estate building codes.

2) House type, orientation, and building construction.

3) Local council requirements.

4) Energy management, insulation selection, and the overall anatomy of the building roof.

Roof types have different pitch values depending on building type and house style. The most common pitches for roofing in Australia are 18 - 20 degrees, depending on the materials used. The prime reason for selecting roofing material for the case study is that it can be tailored at the design stage and plays an important role in maintaining the overall sustainability ranking of building.

The three options in **Table 11** were tested against six alternatives from the two major suppliers in the Australian construction industry. The alternatives have various competitive advantages over each other.

The tabulated values in the Excel spreadsheet assigned the sub-criteria with positive or negative signs: criteria with an inverse relationship to sustainability are marked as negative and criteria that enhance the sustainability are marked as positive. The six alternatives were tested against the 23 sub-criteria related to those main six. The MCDM technique with TOPSIS gives a final ranking of these criteria and sub-criteria based on expert opinion [24].

Yoon and Hwang introduced the TOPSIS method, which proposes that the best alternative has the shortest distance to the ideal solution [25] [26]. The attribute which favors an alternative material is called the best attribute and the other is called the worst attribute. The goal of this approach is to find the Euclidean space from the ideal solution [27]. TOPSIS comprises six major steps, which are described as follows using our hypothetical problem of roofing material (roof tiles) from the two major suppliers of roof tiling.

Step 1: Calculate the normalized matrix.

The normalization is calculated using Equation (7) [28]:

$$\overline{X_{ij}} = X_{ij} \Big/ \sqrt{\sum_{j=1}^{n} X_{ij}^2} \quad \text{where} \quad i = 1, 2, \cdots, n \quad \text{and} \quad j = 1, 2, \cdots, m \tag{7}$$

In a matrix, the i and j belong to the first row and first column value.

Step 2: Calculate the weighted normalized matrix.

The normalized matrix is then multiplied with the weighted value as per equation (8);

$$V_{ij} = \overline{X_{ij}} \times W_j \quad [27] \ [29] \tag{8}$$

Step 3: Calculate the ideal best and ideal worst value.

In this step, the ideal best value is the value which suits the criteria, represented by the maximum value; the ideal best negative value which opposes the agree-

ment of criteria is represented by the minimum value.

Step 4: Calculate the Euclidean distance from ideal best value.

This distance will be the closest value to ideal best value, using the Equation (9):

$$S^{+}_{i} = \left[\sum_{j=1}^{n}\left(V_{ij} - V_{J^{+}}\right)^{2}\right]^{0.5} \tag{9}$$

Step 5: Calculate the Euclidean distance from ideal worst value.

This distance will be the closest value to ideal worst value, using Equation (10):

$$S^{-}_{i} = \left[\sum_{j=1}^{n}\left(V_{ij} - V_{J^{-}}\right)^{2}\right]^{0.5} \quad [30] \tag{10}$$

Step 6: Calculate the relative closeness to the ideal solution.

The relative closeness to the ideal solution is calculated using Equation (11):

$$C_{i} = S^{-}{}_{i} / S_{i}^{+} + S_{i}^{-} \tag{11}$$

The final calculated values rank the alternatives, with 1 being the best alternative (Table 12). The MCDM can be used to solve the problem of material selection where an infinite number of alternatives exist.

Tables 13-17 show the calculations in the Excel spreadsheet. The weighted

Table 12. Ranked list of criteria.

	Ranked list of criteria
C1	Capital cost
C2	Maintenance cost
C3	Discarding cost
C4	Raw material extraction
C5	Environmental effect of extraction process
C6	Wastage expectancy
C7	Contained energy
C8	Sustainable disposal option
C9	Potential for reuse and recycling of material
C10	Legislation compliance capability
C11	Pollution control
C12	Air quality maintenance
C13	Ozone layer influence
C14	Toxicity
C15	Resistance to decay
C16	Fire resistance
C17	Thermal insulation capacity
C18	Durability
C19	Buildability
C20	Usage of local material
C21	Aesthetics
C22	Health and safety concerns
C23	Labor availability

Table 13. Data input table.

Data Input table

Supplier	Name for reference		Capital cost	Maintenance cost	Discarding cost	Raw material extraction	Environmental effect of extraction process	Wastage expectancy	Contained energy	Sustainable disposal option	Potential of reuse and recycling of material	Legislation compliance capability	Pollution control	Air quality maintenance	Ozone layer influence	Toxicity	Resistance to decay	Fire resistance	Thermal insulation capacity	Durability	Buildability	Usage of local material	Aesthetics	Health and safety concerns	Labour availability
		Criteria	C1	C2	C3	C4	C5	C6	C7	C8	C9	C10	C11	C12	C13	C14	C15	C16	C17	C18	C19	C20	C21	C22	C23
		Alternatives																							
S1	Terracotta range	A1	7	6	6	7	6	6	4	7	7	7	7	6	4	6	3	5	4	3	5	7	6	5	4
	Designer ceramic range	A2	4	2	4	6	4	4	5	5	5	6	5	5	5	2	5	7	6	5	6	4	7	7	5
	Concrete range	A3	3	1	4	6	3	2	6	4	4	6	6	4	5	3	6	6	5	7	7	5	6	6	7
S2	Terracotta range	A4	6	6	6	7	6	5	4	7	6	7	7	6	4	6	3	4	3	4	6	6	6	6	5
	Designer ceramic range	A5	5	2	4	6	4	4	6	5	5	6	5	4	5	4	4	6	5	5	5	5	5	5	6
	Concrete range	A6	4	1	4	6	2	2	7	4	4	6	6	4	4	3	5	7	4	6	4	4	6	6	5
		Criteria Sign Range	−1	−1	−1	−1	−1	−1	1	1	1	1	1	1	−1	−1	1	1	1	1	1	1	1	1	1
		W (Lambda)	1	1	1	1	1	1	1	1	1	1	1	1	1	1	1	1	1	1	1	1	1	1	1

Table 14. Normalized values table.

Normalization = N	C1	C2	C3	C4	C5	C6	C7	C8	C9	C10	C11	C12	C13	C14	C15	C16	C17	C18	C19	C20	C21	C22	C23
A1	0.5697	0.6626	0.5145	0.4500	0.5547	0.5970	0.2998	0.5217	0.5417	0.4500	0.4719	0.4983	0.3607	0.5721	0.2739	0.3442	0.3549	0.2372	0.3656	0.5417	0.4064	0.3475	0.3015
A2	0.3255	0.2209	0.3430	0.3857	0.3698	0.3980	0.3748	0.3727	0.3869	0.3857	0.3371	0.4152	0.4508	0.1907	0.4564	0.4819	0.5324	0.3953	0.4388	0.3095	0.4741	0.4865	0.3769
A3	0.2441	0.1104	0.3430	0.3857	0.2774	0.1990	0.4497	0.2981	0.3095	0.3857	0.4045	0.3322	0.4508	0.2860	0.5477	0.4131	0.4437	0.5534	0.5119	0.3869	0.4064	0.4170	0.5276
A4	0.4883	0.6626	0.5145	0.4500	0.5547	0.4975	0.2998	0.5217	0.4643	0.4500	0.4719	0.4983	0.3607	0.5721	0.2739	0.2754	0.2662	0.3162	0.4388	0.4643	0.4064	0.4170	0.3769
A5	0.4069	0.2209	0.3430	0.3857	0.3698	0.3980	0.4497	0.3727	0.3869	0.3857	0.3371	0.3322	0.4508	0.3814	0.3651	0.4131	0.4437	0.3953	0.3656	0.3869	0.3386	0.3475	0.4523
A6	0.3255	0.1104	0.3430	0.3857	0.1849	0.1990	0.5247	0.2981	0.3095	0.3857	0.4045	0.3322	0.3607	0.2860	0.4564	0.4819	0.3549	0.4743	0.2925	0.3095	0.4064	0.4170	0.3769

Table 15. Weighted normalized values table.

Weighted Normalization = V	C1	C2	C3	C4	C5	C6	C7	C8	C9	C10	C11	C12	C13	C14	C15	C16	C17	C18	C19	C20	C21	C22	C23
A1	0.0239	0.0172	0.0206	0.0247	0.0200	0.0197	0.0138	0.0240	0.0244	0.0247	0.0245	0.0209	0.0141	0.0200	0.0104	0.0172	0.0138	0.0102	0.0176	0.0244	0.0211	0.0174	0.0139
A2	0.0137	0.0057	0.0137	0.0212	0.0133	0.0131	0.0172	0.0171	0.0174	0.0212	0.0175	0.0174	0.0176	0.0067	0.0173	0.0241	0.0208	0.0170	0.0211	0.0139	0.0247	0.0243	0.0173
A3	0.0103	0.0029	0.0137	0.0212	0.0100	0.0066	0.0207	0.0137	0.0139	0.0212	0.0210	0.0140	0.0176	0.0100	0.0208	0.0207	0.0173	0.0238	0.0246	0.0174	0.0211	0.0209	0.0243
A4	0.0205	0.0172	0.0206	0.0247	0.0200	0.0164	0.0138	0.0240	0.0209	0.0247	0.0245	0.0209	0.0141	0.0200	0.0104	0.0138	0.0104	0.0136	0.0211	0.0209	0.0211	0.0209	0.0173
A5	0.0171	0.0057	0.0137	0.0212	0.0133	0.0131	0.0207	0.0171	0.0174	0.0212	0.0175	0.0140	0.0176	0.0133	0.0139	0.0207	0.0173	0.0170	0.0176	0.0174	0.0176	0.0174	0.0208
A6	0.0137	0.0029	0.0137	0.0212	0.0067	0.0066	0.0241	0.0137	0.0139	0.0212	0.0210	0.0140	0.0141	0.0100	0.0173	0.0241	0.0138	0.0204	0.0140	0.0139	0.0211	0.0209	0.0173

Table 16. Ideal best and ideal worst values table.

Criteria	C1	C2	C3	C4	C5	C6	C7	C8	C9	C10	C11	C12	C13	C14	C15	C16	C17	C18	C19	C20	C21	C22	C23
V+	0.0239	0.0172	0.0206	0.0247	0.0200	0.0197	0.0241	0.0240	0.0244	0.0247	0.0245	0.0209	0.0176	0.0200	0.0208	0.0241	0.0208	0.0238	0.0246	0.0244	0.0247	0.0243	0.0243
V−	0.0103	0.0029	0.0137	0.0212	0.0067	0.0066	0.0138	0.0137	0.0139	0.0212	0.0175	0.0140	0.0141	0.0067	0.0104	0.0138	0.0104	0.0102	0.0140	0.0139	0.0176	0.0174	0.0139

Table 17. Relative closeness and final ranking table.

Si+	Si−	Ci	Rank
0.0269	0.0372	0.5801	**1**
0.0325	0.0252	0.4372	**3**
0.0364	0.0272	0.4272	**4**
0.0260	0.0343	0.5686	**2**
0.0310	0.0215	0.4095	**5**
0.0399	0.0209	0.3440	**6**

values are used to give the best and worst alternatives for each criterion.

The values in Table 15, were calculated using the *formula* 8, the weights were determined using the data ranking and weights awarded by the experts according to their practical experience.

7. Conclusion

The results obtained agree with the TOPSIS ranking technique. Alternative 1 is ranked at first position: this is the best alternative available if we consider all of the 23 criteria weighted by the experts. The remaining alternatives are ranked accordingly considering the rest of criteria the best suitable for those materials.

Acknowledgements

M.R.M. gathered all the data and ran the analysis in the presented format. V.P. cross-checked all the information and validated the results with his experience in Information Systems.

Funding

This research received no external funding, only the resources provided by Curtin University, Perth, Western Australia.

Conflicts of Interest

The authors declare no conflicts of interest.

References

[1] Dulaimi, M.F., Ling, F.Y. and Bajracharya, A. (2003) Organizational Motivation and Inter-Organizational Interaction in Construction Innovation in Singapore. *Construction Management and Economics*, **21**, 307-318. https://doi.org/10.1080/0144619032000056144

[2] Black, C., Akintoye, A. and Fitzgerald, E. (2000) An Analysis of Success Factors and Benefits of Partnering in Construction. *International Journal of Project Management*, **18**, 423-434. https://doi.org/10.1016/S0263-7863(99)00046-0

[3] Chinyio, E.A. and Olomolaiye, P.O. (1999) A Needs Based Methodology for Classifying Construction Clients and Selecting Contractors—A Rejoinder. *Construction Management & Economics*, **17**, 413-417. https://doi.org/10.1080/014461999371330

[4] Gliem, J.A. and Gliem, R.R. (2003) Calculating, Interpreting, and Reporting Cronbach's Alpha Reliability Coefficient for Likert-Type Scales. *Midwest Research to Practice Conference in Adult, Continuing, and Community Education*, Ohio State University, 82-88.

[5] Marshall, B., Cardon, P., Poddar, A. and Fontenot, R. (2013) Does Sample Size Matter in Qualitative Research? A Review of Qualitative Interviews in IS Research. *Journal of Computer Information Systems*, **54**, 11-22. https://doi.org/10.1080/08874417.2013.11645667

[6] Francis, J.J., Johnston, M., Robertson, C., Glidewell, L., Entwistle, V., Eccles, M.P., *et al.* (2010) What Is an Adequate Sample Size? Operationalising Data Saturation for Theory-Based Interview Studies. *Psychology and Health*, **25**, 1229-1245. https://doi.org/10.1080/08870440903194015

[7] Munn, P. and Drever, E. (1990) Using Questionnaires in Small-Scale Research. A Teachers' Guide, ERIC.

[8] Mason, M. (2010) Sample Size and Saturation in PhD Studies Using Qualitative Interviews. Forum Qualitative Sozialforschung/Forum: Qualitative Social Research.

[9] Wang, L., Shen, W., Xie, H., Neelamkavil, J. and Pardasani, A. (2002) Collaborative Conceptual Design—State of the Art and Future Trends. *Computer-Aided Design*, **34**, 981-996. https://doi.org/10.1016/S0010-4485(01)00157-9

[10] Rao, P. and Holt, D. (2005) Do Green Supply Chains Lead to Competitiveness and Economic Performance? *International Journal of Operations & Production Management*, **25**, 898-916. https://doi.org/10.1108/01443570510613956

[11] Ding, G.K. (2008) Sustainable Construction—The Role of Environmental Assessment Tools. *Journal of Environmental Management*, **86**, 451-164. https://doi.org/10.1016/j.jenvman.2006.12.025

[12] Tan, Y., Shen, L. and Yao, H. (2011) Sustainable Construction Practice and Contractors' Competitiveness: A Preliminary Study. *Habitat International*, **35**, 225-230. https://doi.org/10.1016/j.habitatint.2010.09.008

[13] Bribián, I.Z., Capilla, A.V. and Usón, A.A. (2011) Life Cycle Assessment of Building Materials: Comparative Analysis of Energy and Environmental Impacts and Evaluation of the Eco-Efficiency Improvement Potential. *Building and Environment*, **46**, 1133-1140. https://doi.org/10.1016/j.buildenv.2010.12.002

[14] Dair, C.M. and Williams, K. (2006) Sustainable Land Reuse: The Influence of Different Stakeholders in Achieving Sustainable Brownfield Developments in England. *Environment and Planning A*, **38**, 1345-1366. https://doi.org/10.1068/a37370

[15] Xu, Z. and Yager, R.R. (2006) Some Geometric Aggregation Operators Based on Intuitionistic Fuzzy Sets. *International Journal of General Systems*, **35**, 417-433. https://doi.org/10.1080/03081070600574353

[16] Omar, M.N. and Fayek, A.R. (2016) A TOPSIS-Based Approach for Prioritized Aggregation in Multi-Criteria Decision-Making Problems. *Journal of Multi-Criteria Decision Analysis*, **23**, 197-209. https://doi.org/10.1002/mcda.1561

[17] Zhao, X., Lin, R. and Wei, G. (2013) Fuzzy Prioritized Operators and Their Application to Multiple Attribute Group Decision Making. *Applied Mathematical Modelling*, **37**, 4759-4770. https://doi.org/10.1016/j.apm.2012.09.048

[18] Yager, R.R., Gumrah, G. and Reformat, M.Z. (2011) Using a Web Personal Evaluation Tool-PET for Lexicographic Multi-Criteria Service Selection. *Knowledge-Based Systems*, **24**, 929-942. https://doi.org/10.1016/j.knosys.2011.02.004

[19] Chen, L. and Xu, Z. (2014) A Prioritized Aggregation Operator Based on the OWA

Operator and Prioritized Measure. *Journal of Intelligent & Fuzzy Systems*, **27**, 1297-1307. https://doi.org/10.3233/IFS-131098

[20] Chu, T.-C. (2002) Facility Location Selection Using Fuzzy TOPSIS under Group Decisions. *International Journal of Uncertainty, Fuzziness and Knowledge-Based Systems*, **10**, 687-701. https://doi.org/10.1142/S0218488502001739

[21] Lootsma, F.A. (2000) Distributed Multi-Criteria Decision Making and the Role of the Participants in the Process. *Journal of Multi-Criteria Decision Analysis*, **9**, 45-55. https://doi.org/10.1002/1099-1360(200001/05)9:1/3<45::AID-MCDA266>3.0.CO;2-L

[22] Yager, R.R. (2009) Prioritized OWA Aggregation. *Fuzzy Optimization and Decision Making*, **8**, 245-262. https://doi.org/10.1007/s10700-009-9063-4

[23] Bisdorff, R., Meyer, P. and Veneziano, T. (2014) Elicitation of Criteria Weights Maximising the Stability of Pairwise Outranking Statements. *Journal of Multi-Criteria Decision Analysis*, **21**, 113-124. https://doi.org/10.1002/mcda.1496

[24] Çalışkan, H., Kurşuncu, B., Kurbanoğlu, C. and Güven, Ş.Y. (2013) Material Selection for the Tool Holder Working under Hard Milling Conditions Using Different Multi Criteria Decision Making Methods. *Materials & Design*, **45**, 473-479. https://doi.org/10.1016/j.matdes.2012.09.042

[25] Yoon, K. (1980) Systems Selection by Multiple Attribute Decision Making. PhD Thesis, Kansas State University, Manhattan (KS).

[26] Hwang, B.G. and Tan, J.S. (2012) Green Building Project Management: Obstacles and Solutions for Sustainable Development. *Sustainable Development*, **20**, 335-349. https://doi.org/10.1002/sd.492

[27] Tzeng, G.-H., Lin, C.-W. and Opricovic, S. (2005) Multi-Criteria Analysis of Alternative-Fuel Buses for Public Transportation. *Energy Policy*, **33**, 1373-1383. https://doi.org/10.1016/j.enpol.2003.12.014

[28] Shanian, A. and Savadogo, O. (2006) TOPSIS Multiple-Criteria Decision Support Analysis for Material Selection of Metallic Bipolar Plates for Polymer Electrolyte Fuel Cell. *Journal of Power Sources*, **159**, 1095-1104. https://doi.org/10.1016/j.jpowsour.2005.12.092

[29] Sharma, P.K., Aggarwal, A. and Gupta, R. (1993) An Expert System for Aid in Material Selection Process. *Proceedings of the Engineering Management Society Conference on Managing Projects in a Borderless World*, New Delhi, 17-18 December 1993, 27-31.

[30] Chatterjee, P., Athawale, V.M. and Chakraborty, S. (2010) Selection of Industrial Robots Using Compromise Ranking and Outranking Methods. *Robotics and Computer-Integrated Manufacturing*, **26**, 483-489. https://doi.org/10.1016/j.rcim.2010.03.007

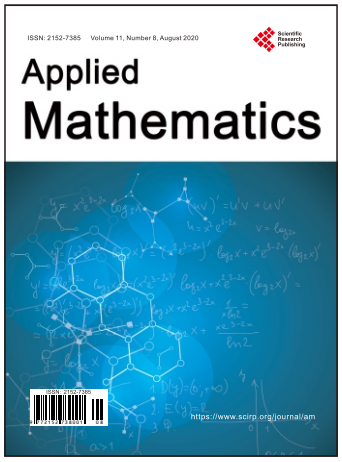

Call for Papers

Applied Mathematics (AM)

ISSN Print: 2152-7385 ISSN Online: 2152-7393
https://www.scirp.org/journal/am

Applied Mathematics **(AM)** is an international journal dedicated to the latest advancement of applied mathematics. The goal of this journal is to provide a platform for scientists and academicians all over the world to promote, share, and discuss various new issues and developments in different areas of applied mathematics.

Subject Coverage

All manuscripts must be prepared in English, and are subject to a rigorous and fair peer-review process. Accepted papers will immediately appear online followed by printed hard copy. The journal publishes original papers including but not limited to the following fields:

- Applied Probability
- Applied Statistics
- Approximation Theory
- Chaos Theory
- Combinatorics
- Complexity Theory
- Computability Theory
- Computational Methods in Mechanics and Physics
- Continuum Mechanics
- Control Theory
- Cryptography
- Discrete Geometry
- Dynamical Systems
- Elastodynamics
- Evolutionary Computation
- Financial Mathematics
- Fuzzy Logic
- Game Theory
- Graph Theory
- Information Theory
- Inverse Problems
- Linear Programming
- Mathematical Biology
- Mathematical Chemistry
- Mathematical Economics
- Mathematical Physics
- Mathematical Psychology
- Mathematical Sociology
- Matrix Computations
- Neural Networks
- Nonlinear Processes in Physics
- Numerical Analysis
- Operations Research
- Optimal Control
- Optimization
- Ordinary Differential Equations
- Partial Differential Equations
- Probability Theory
- Statistical Finance
- Stochastic Processes
- Theoretical Statistics

We are also interested in: 1) Short Reports—2-5 page papers where an author can either present an idea with theoretical background but has not yet completed the research needed for a complete paper or preliminary data; 2) Book Reviews—Comments and critiques.

Notes for Intending Authors

Submitted papers should not have been previously published nor be currently under consideration for publication elsewhere. Paper submission will be handled electronically through the website. All papers are refereed through a peer review process. For more details about the submissions, please access the website.

Website and E-mail

https://www.scirp.org/journal/am **E-mail: am@scirp.org**

What is SCIRP?

Scientific Research Publishing (SCIRP) is one of the largest Open Access journal publishers. It is currently publishing more than 200 open access, online, peer-reviewed journals covering a wide range of academic disciplines. SCIRP serves the worldwide academic communities and contributes to the progress and application of science with its publication.

What is Open Access?

All original research papers published by SCIRP are made freely and permanently accessible online immediately upon publication. To be able to provide open access journals, SCIRP defrays operation costs from authors and subscription charges only for its printed version. Open access publishing allows an immediate, worldwide, barrier-free, open access to the full text of research papers, which is in the best interests of the scientific community.

- High visibility for maximum global exposure with open access publishing model
- Rigorous peer review of research papers
- Prompt faster publication with less cost
- Guaranteed targeted, multidisciplinary audience

Scientific Research Publishing

Website: https://www.scirp.org

Subscription: sub@scirp.org

Advertisement: service@scirp.org